

CHEMICAL BATH DEPOSITED ZINC CADMIUM SULFIDE AND SPUTTER DEPOSITED  
ZINC OXIDE FOR THIN FILM SOLAR CELL DEVICE FABRICATION

By

ANDRE BARAN V

A DISSERTATION PRESENTED TO THE GRADUATE SCHOOL  
OF THE UNIVERSITY OF FLORIDA IN PARTIAL FULFILLMENT  
OF THE REQUIREMENTS FOR THE DEGREE OF  
DOCTOR OF PHILOSOPHY

UNIVERSITY OF FLORIDA

2009

© 2009 Andre Baran V

To my parents who have supported me in all areas of my life.

## ACKNOWLEDGMENTS

I wish to thank the chair of my supervisory committee, Dr. Crisalle, for his invaluable support and his sincere understanding throughout the last five years. I would also like to thank Dr. Craciun for all the characterization support that he provided and for agreeing to serve on my committee, along with Dr. Hoflund and Dr. Svoronos. This work would have not been possible without the equipment expertise of Dr. Mark Davidson, and I am very grateful for his assistance. Chuck Rowland also helped deal with equipment issues and support and I sincerely appreciate his efforts.

I would like to thank all the colleagues that I have had the privilege of working with. I thank Jiyon Song, Ryan Kaczynski, Ryan Acher, Wei Liu, and Woo Kyoung Kim, all of whom participated in our photovoltaics group at the University of Florida. I would also like to thank Sean Jones and Kim Interliggi-Crim for their invaluable support and discussions. In addition I would like to thank Evan Law for his assistance with equipment repair, and Dr. Maggie Puga-Lambers for the SIMS work. I thank Andrew Gerger the AFM work. I would especially like to thank Jacqueline Hodges for the numerous nights she spent by my side.

Lastly, I would like to thank my parents for all their hard work and support that has gotten me to this point in my life. They have supported me every step of the way, and I doubt I'll ever be able to thank them enough.

## TABLE OF CONTENTS

	<u>page</u>
ACKNOWLEDGMENTS .....	4
LIST OF TABLES .....	9
LIST OF FIGURES .....	10
LIST OF ABBREVIATIONS.....	14
ABSTRACT.....	16
CHAPTER	
1 INTRODUCTION.....	18
2 TECHNOLOGY OVERVIEW.....	28
Solar Cell Device Physics.....	28
Photodevices.....	28
The Photoelectric Effect.....	28
Solar Radiation.....	29
Band Gap Energy.....	30
Solar Cell Materials.....	30
Thin Film Solar Cell Materials.....	31
Amorphous Silicon Alloys Solar Cells.....	32
Amorphous Silicon Growth Methods.....	33
Copper Indium Diselenide.....	34
Copper Gallium Diselenide.....	35
Copper Indium Gallium Diselenide.....	36
Cadmium Sulfide.....	37
Zinc Sulfide.....	38
Zinc Cadmium Sulfide.....	38
Zinc Selenide.....	39
Indium Tin Oxide.....	40
Zinc Oxide.....	41
Chemical Bath Deposition.....	42
Fundamentals.....	42
Nucleation.....	43
Film Growth.....	45
Ion-by-ion mechanism.....	45
Hydroxide cluster mechanism.....	46
Sputter Deposition.....	47
Chamber Features.....	48
Targets.....	48
Sputter Sources.....	49

	Nonmagnetron sputter sources .....	49
	Magnetron sputter sources .....	50
	Ion beam sputter sources .....	50
3	METHODS AND TECHNIQUES .....	60
	Substrate Cleaning Procedure .....	60
	Absorber Layer Fabrication .....	61
	Buffer Layer Fabrication .....	62
	Chemical Bath Deposition Apparatus .....	62
	Transparent Conductive Oxide Fabrication .....	63
	Sputter Deposition System .....	64
	Photovoltaic Device Fabrication .....	67
	Back Contact .....	67
	Metallization and Anti-Reflective Coating .....	68
	Characterization Techniques .....	68
	Inductively Coupled Plasma .....	68
	Scanning Electron Microscopy .....	70
	Secondary electron imaging .....	71
	Backscattered electron imaging .....	71
	Energy dispersive spectroscopy .....	72
	X-Ray Diffraction .....	72
	Profilometry .....	74
	Ellipsometry .....	75
	Ultraviolet-Visible Spectroscopy .....	75
	X-Ray Photoelectron Spectroscopy .....	77
	Secondary Ion Mass Spectrometry .....	78
	Auger Electron Spectroscopy .....	79
	Four-Point Probe .....	81
	Photovoltaic Device Characterization Techniques .....	82
	Current-Voltage .....	82
	Current-Voltage Measurement .....	84
	Quantum Efficiency .....	85
4	ZINC CADMIUM SULFIDE BUFFER LAYER GROWTH .....	99
	Introduction .....	99
	Chemical Bath Deposition of Zinc Cadmium Sulfide .....	101
	Materials .....	102
	Growth Procedure .....	102
	Substrate and equipment cleaning .....	103
	Preparation of dose solutions .....	104
	Bath temperature conditioning .....	104
	Buffer layer deposition .....	105
	Termination of growth .....	105
	Zinc Cadmium Sulfide Buffer Layer Characterization Results .....	106

	Growth Rate.....	106
	Film Composition.....	107
	Optical Characteristics.....	108
	Conclusions.....	110
5	CHARACTERIZATION OF SPUTTER DEPOSITED ZINC OXIDE.....	124
	Introduction.....	124
	Experimental.....	125
	Equipment.....	125
	Materials.....	126
	Zinc Oxide Characterization Results.....	127
	Film Thickness.....	127
	Aluminum doped.....	128
	Hydrogen and aluminum doped.....	129
	Comparison of AZO and HAZO.....	130
	Electrical Characteristics.....	131
	Aluminum doped.....	131
	Hydrogen and aluminum doped.....	133
	Comparison of AZO and HAZO.....	135
	Optical Characteristics.....	136
	Figure of Merit.....	137
	Conclusions.....	138
6	THERMAL TREATMENT OF ZINC OXIDE.....	157
	Introduction.....	157
	Experimental.....	158
	Equipment.....	159
	Materials.....	160
	Annealing Results.....	161
	Electrical Characterization.....	161
	Aluminum doped.....	162
	Hydrogen and aluminum doped.....	163
	Optical Characterization.....	163
	Aluminum doped.....	164
	Hydrogen and aluminum doped.....	164
	Figure of Merit.....	165
	Aluminum doped.....	165
	Hydrogen and aluminum doped.....	166
	Structural Characteristics.....	166
	Surface Roughness.....	167
	Aluminum doped.....	167
	Hydrogen and aluminum doped.....	167
	Conclusions.....	168

LIST OF REFERENCES.....	181
BIOGRAPHICAL SKETCH.....	189

## LIST OF TABLES

<u>Table</u>		<u>page</u>
2-1	Approximate solubility product of commonly chemically bath deposited compounds. ...	52
3-1	Reference data for NREL device S2117-A2.....	87
4-1	Recipe for the preparation of the chemical bath solution for five different zinc compositions. ....	111
4-2	Resulting chemical bath solutions for five different zinc compositions.....	111
4-3	Zinc cadmium sulfide film thicknesses for five values of prepared fractional composition of zinc at 85°C.....	111
4-4	Comparison of measured fractional zinc composition in films deposited for 45 minutes with five prepared zinc compositions at 85°C. ....	112
4-5	Average transmission of three wavelength ranges for ZnCdS films deposited for 45 minutes with five prepared zinc compositions at 85°C. ....	112
5-1	Average thickness of AZO films at flowrates of 30.0, 40.0, 50.0, and 60.0 sccm. ....	139
5-2	Average thickness of HAZO films at flowrates of 20.0, 30.0, 40.0, and 50.0 sccm. ....	139
6-1	International Centre for Diffraction Data fingerprint for ZnO. ....	169
6-2	Thermal treatment results for AZO films. ....	169
6-3	Thermal treatment results for HAZO films. ....	169
6-4	Surface roughness of annealed AZO and HAZO measured by AFM. ....	170

## LIST OF FIGURES

<u>Figure</u>	<u>page</u>
2-1 A p-n junction photovoltaic device.....	53
2-2 Band diagram of the photoelectric effect in a p-n junction photodevice.....	54
2-3 Solar spectrum at AM0 and AM1.5.....	55
2-4 Chronological progress of a-Si, CdTe, and CIS thin film technologies from 1975 to 2005.....	56
2-5 Ion-by-ion growth of CdS crystals.....	57
2-6 Growth of CdS crystals via the hydroxide cluster mechanism.....	58
2-7 Typical sputter deposition chamber.....	59
3-1 Structure of a typical CIGS/ZnCdS device fabricated at UF.....	88
3-2 Chemical bath deposition apparatus.....	89
3-3 Chemical bath deposition reaction vessel.....	90
3-4 Chemical bath deposition apparatus and reaction vessel schematic.....	91
3-5 Perkin-Elmer Model 4400 Production Sputtering System.....	92
3-6 Perkin-Elmer Model 4400 Production Sputtering System schematic drawing.....	93
3-7 Simplified operation of a scanning electron microscope.....	94
3-8 Common experimental arrangement for ellipsometry measurements.....	95
3-9 Simplified UV/vis spectrophotometer schematic.....	96
3-10 Four-point probe configuration schematic.....	97
3-11 Example of a typical $I$ - $V$ curve.....	98
4-1 Film thickness as a function of deposition time for ZnCdS chemically bath deposited at five prepared fractional zinc compositions at 85°C.....	113
4-2 Measured fractional zinc composition ( $x_f$ ) of five films chemically bath deposited at 85°C for 45 minutes at five prepared zinc compositions, $x_p = 0.1, 0.2, 0.3, 0.4,$ and $0.5$ .....	114

4-3	As deposited fractional zinc composition, $x_p$ , as a function of deposition time for five prepared zinc compositions, $x_p = 0.1, 0.2, 0.3, 0.4,$ and $0.5,$ at $85^\circ\text{C}.$ .....	115
4-4	Comparison of measured zinc composition of films deposited at $85^\circ\text{C}$ for 45 minutes with prepared fractional zinc compositions of $x_p = 0.1, 0.2, 0.3, 0.4,$ and $0.5.$ .....	116
4-5	Optical transmission as a function of wavelength for films deposited at $85^\circ\text{C}$ with a prepared fractional zinc composition of $x_p = 0.1,$ at deposition times of 15, 25, 35, and 45 minutes. ....	117
4-6	Optical transmission as a function of wavelength for films deposited at $85^\circ\text{C}$ with a prepared fractional zinc composition of $x_p = 0.2,$ at deposition times of 15, 25, 35, and 45 minutes. ....	118
4-7	Optical transmission as a function of wavelength for films deposited at $85^\circ\text{C}$ with a prepared fractional zinc composition of $x_p = 0.3,$ at deposition times of 15, 25, 35, and 45 minutes. ....	119
4-8	Optical transmission as a function of wavelength for films deposited at $85^\circ\text{C}$ with a prepared fractional zinc composition of $x_p = 0.4,$ at deposition times of 15, 25, 35, and 45 minutes. ....	120
4-9	Optical transmission as a function of wavelength for films deposited at $85^\circ\text{C}$ with a prepared fractional zinc composition of $x_p = 0.5,$ at deposition times of 15, 25, 35, and 45 minutes. ....	121
4-10	Optical transmission as a function of wavelength for films deposited at $85^\circ\text{C}$ for 45 minutes with five prepared fractional compositions, $x_p = 0.1, 0.2, 0.3, 0.4,$ and $0.5.$ .....	122
4-11	Average transmission of three wavelength ranges for ZnCdS films deposited at $85^\circ\text{C}$ for 45 minutes with five prepared zinc compositions, $x_p = 0.1, 0.2, 0.3, 0.4,$ and $0.5.$ .....	123
5-1	Thickness contour plot of AZO film deposited at 0.4 kW with 40 sccm argon working gas flowrate.....	140
5-3	Average AZO film thickness deposited at 0.4 kW with working gas flowrates of 30.0, 40.0, 50.0, and 60.0 sccm argon. ....	142
5-4	Thickness contour plot of HAZO film deposited at 0.4 kW with 40 sccm hydrogen-doped argon working gas flowrate.....	143
5-5	Average HAZO film thickness deposited at 0.4 kW with working gas flowrates of 20.0, 30.0, 40.0, and 50.0 sccm hydrogen-doped argon. ....	144
5-6	Comparison of AZO and HAZO average film thickness as a function of sample position and working gas composition and flowrate. ....	145

5-7	Sheet resistance contour plot of AZO film deposited at 0.4 kW with 40 sccm argon working gas flowrate.....	146
5-8	Minimum AZO sheet resistance deposited at 0.4 kW with working gas flowrates of 30.0, 40.0, 50.0, and 60.0 sccm argon. ....	147
5-9	Maximum AZO sheet resistance deposited at 0.4 kW with working gas flowrates of 30.0, 40.0, 50.0, and 60.0 sccm argon. ....	148
5-10	Sheet resistance contour plot of HAZO film deposited at 0.4 kW with 40.0 sccm hydrogen-doped argon working gas flowrate. ....	149
5-11	Minimum HAZO sheet resistance deposited at 0.4 kW with working gas flowrates of 20.0, 30.0, 40.0, and 50.0 sccm hydrogen-doped argon. ....	150
5-12	Maximum HAZO sheet resistance deposited at 0.4 kW with working gas flowrates of 20.0, 30.0, 40.0, and 50.0 sccm hydrogen-doped argon. ....	151
5-13	Minimum sheet resistance of AZO and HAZO films deposited at 0.4 kW with working gas flowrates of 30.0, 40.0, and 50.0 sccm.....	152
5-14	Maximum sheet resistance of AZO and HAZO films deposited at 0.4 kW with working gas flowrates of 30.0, 40.0, and 50.0 sccm.....	153
5-15	Minimum resistivity of AZO and HAZO films deposited at 0.4 kW. ....	154
5-16	Average transmission of AZO and HAZO films deposited at 0.4 kW. ....	155
5-17	Figure of merit for AZO and HAZO films deposited at 0.4 kW. ....	156
6-1	Rapid thermal processing schematic.....	171
6-2	Minimum and maximum resistivity of AZO films before and after annealing in forming gas, argon, and nitrogen ambients.....	172
6-3	Minimum and maximum resistivity of HAZO films before and after annealing in forming gas, argon, and nitrogen ambients.....	173
6-4	Average transmission of AZO films before and after annealing in forming gas, argon, and nitrogen ambients.....	174
6-5	Average transmission of HAZO films before and after annealing in forming gas, argon, and nitrogen ambients.....	175
6-6	Figure of merit of AZO films before and after annealing in forming gas, argon, and nitrogen ambients.....	176
6-7	Figure of merit of HAZO films before and after annealing in forming gas, argon, and nitrogen ambients.....	177

6-8	Cross-sectional image of HAZO annealed in argon ambient taken with a field-emission scanning electron microscope.....	178
6-9	Atomic force microscopy of AZO films a) as-deposited, and annealed in b) forming gas, c) argon, and d) nitrogen ambients. ....	179
6-10	Atomic force microscopy of HAZO films a) as-deposited, and annealed in b) forming gas, c) argon, and d) nitrogen ambients. ....	180

## LIST OF ABBREVIATIONS

AES	Auger electron spectroscopy
AFM	Atomic force microscopy
AZO	Aluminum-doped zinc oxide
a-Si	Amorphous silicon
CBD	Chemical bath deposition
CIS	Copper indium diselenide
CIGS	Copper indium gallium diselenide
CGS	Copper gallium diselenide
CVD	Chemical vapor deposition
EDS	Energy dispersive (x-ray) spectroscopy
EDX	Energy dispersive x-ray spectroscopy
FWHM	Full-width, half maximum
GIXRD	Grazing incidence x-ray diffraction
H-AZO	Hydrogen-aluminum-doped zinc oxide
IBE	Ion beam etching
IBS	Ion beam sputtering
ICP	Inductively coupled plasma spectroscopy
ITO	Indium tin oxide
MBE	Molecular beam epitaxy
MOCVD	Metal-organic chemical vapor deposition
MSP	Magnetron sputtering
PACVD	Plasma-assisted chemical vapor deposition
PCVD	Plasma chemical vapor deposition
PMEE	Plasma migration enhanced epitaxy

PVD	Physical vapor deposition
RF	Radio frequency
SEM	Scanning electron microscopy
SIMS	Secondary ion mass spectroscopy
TCO	Transparent conductive oxide
XPS	X-ray photoelectron spectroscopy
XRD	X-ray diffraction

Abstract of Dissertation Presented to the Graduate School  
of the University of Florida in Partial Fulfillment of the  
Requirements for the Degree of Doctor of Philosophy

CHEMICAL BATH DEPOSITED ZINC CADMIUM SULFIDE AND SPUTTER DEPOSITED  
ZINC OXIDE FOR THIN FILM SOLAR CELL DEVICE FABRICATION

By

Andre Baran V

August 2009

Chair: Oscar D. Crisalle  
Major: Chemical Engineering

Chemical bath deposition, or CBD, is used to successfully deposit ZnCdS buffer layers that have many benefits over the traditional CdS thin films used in photovoltaic devices. The characteristics of films growth such as growth rate, optical transmission, and film composition is analyzed. The addition of Zn to CdS has important benefits that aid in improving device performance and therefore it is important to determine how the incorporation of zinc affects film characteristics. Film thickness is found to increase with deposition time and growth rate is determined to be a function of the prepared bath zinc composition. The zinc composition in the prepared bath is also found to affect the optical transmission of deposited film, most notably in the short wavelength region.

The transparent conductive oxide ZnO is deposited via RF magnetron sputtering. The effect of aluminum and hydrogen doping is studied by sputtering an aluminum-doped zinc oxide target with argon (AZO) and an argon mixture with hydrogen (HAZO). The addition of hydrogen to the working gas decreases film resistance in addition to improving other characteristics. The working gas pressure and position under the target are also found to have a significant effect on film properties. A figure of merit calculation allows for a single valued representation of the combined characteristics of the deposited films. The figure of merit

calculation takes into consideration film resistivity, optical transmission, and provides a quantitative value of the potential performance in photovoltaic devices.

The effect of thermal treatments on sputter deposited AZO and HAZO films are determined by way of rapid thermal annealing. High temperature annealing of ZnO is found to improve film characteristics. The gas ambient used in the thermal treatment process is found to be a critical parameter in post-anneal film quality. Gas ambients of nitrogen, argon, and forming gas, a nitrogen and hydrogen mixture, were employed in the thermal treatment studies. In general, optical transmission and resistivity improve for all films under each ambient, although films annealed in forming gas show the most improvement, with resulting figure of merit values two to three times their as deposited values.

## CHAPTER 1 INTRODUCTION

Renewables, broadly speaking, are fuels whose use today do not reduce the supply for tomorrow. The major sources of renewable energy are solar, wind, and hydropower. These energies are by definition nondepletable. They cannot be completely used up as they are continually being replenished. Renewable energies are also sustainable, meaning that they can provide for the energy needs of the present without reducing the availability of energy in the future.

Renewable energy is a promising alternative to the fossil fuels that have become vital to our industrialized society supplying the majority of our energy needs. Problems with fossil fuels have led to re-examination of their use and a search for alternatives. Some of the problems that exist with fossil fuels are environmental damage, unequal distribution of resources, price instability, and supply constraints. Renewable energy offers solutions to the problems that have risen with traditional forms of energy by being relatively clean, widely available, and having a virtually unlimited supply. There have been impressive technical advances in renewable technology, specifically for electricity generation. The costs of renewable energy have dropped considerably and are almost competitive with fossil fuels.

Typically, the majority of people seem to like the idea of renewables. Polls have shown strong and consistent public support. Trends in the polls show long-standing preference for renewables compared to other energy forms. These trends have been consistent in the poll data for 20 years making it one of the strongest patterns in all the US national poll data on energy and the environment [1].

Renewable energy, however, is not a ‘no problems’ solution to replacing fossil fuels. A close look at renewable energy reveals that they too have their limitations. Costs have come

down, but they are still more expensive than fossil fuels in several cases. In addition, not all renewable resources are widely available or evenly distributed, and each has their own set of environmental impacts. For example, wind can be intermittent and therefore a poor solution for some electricity systems.

Given the limitations we need to make the best use of renewables. One approach to achieve this is through a government policy to promote greater use of renewable energy. Our energy system is heavily regulated and publicly controlled, and always has been. This is changing, but government still plays a significant role in energy. Changes in government policy are the first step to inducing changes in the energy system. The industrialized worlds' energy system provides dependable light, heat, and industrial power and supplies, and is in many ways an impressive success. Though, it does have its share of problems, problems that are becoming more apparent and require attention. These problems again are environmental damage, inequitable distribution of fossil fuel resources, depleting supplies, and economic damage due to price volatility.

Eighty percent of the world's energy is provided by fossil fuels, oil, coal, and natural gas. The burning of these fuels creates several urgent environmental problems. Climate change, the warming of the earth due to human induced increases in certain atmospheric gases, specifically CO<sub>2</sub>, is due largely to the burning of fossil fuels. Burning also results in emissions of other pollutants such as sulfur oxides, nitrogen oxides, and other particulates. These pollutants raise many public health and environmental concerns. Biomass and waste accounts for 11% of the worlds energy consumption, nuclear accounts for 7%, hydropower accounts for 2%, and geothermal, wind and solar accounts for less than 1%.

Renewable forms of energy are considered to be low impact on the environment in comparison to fossil fuels. Wind power, solar power, and hydropower contribute little or no CO<sub>2</sub> to the environment. Therefore, they do not directly contribute to climate change. However, some will argue that hydropower contributes to climate change due to the methane produced from biological matter in dammed areas. There are no direct air emissions from hydropower, solar power, or wind power fueled facilities so they are not responsible for any local or regional air quality problems. Wind and solar energies do not require mining or fuel transport systems. This eliminates them from being associated with environmental damage. Although they are not entirely innocuous, in general, renewables are cleaner and more environmentally friendly than fossil fuels.

As mentioned, the distribution of energy, a universal human need, is uneven across the planet. The uneven distribution of what has become a necessary resource results in international tensions, trade deficits, and constraints on global development. For example, the US is responsible for 26% of annual petroleum consumption but only 12% of its production [2]. Approximately two-thirds of the world's crude oil reserves are in the Middle East, and although Asia has 56 % of the world's population, it has less than 30% of the world's recoverable coal reserves [2].

Fossil fuel resources are being depleted, and there are disagreements over just how much oil, natural gas, and coal are left and when it will become necessary to find alternatives. What is not in dispute, however, is that fossil fuel resources are finite, and whether their lifetime is another 30 years, or 300 years, eventually those resources will run dry and it will become necessary to find one, or many, replacements. Another concern of fossil fuels is the economic damage being caused as a result of its price volatility. The prices of oil and natural gas are

alarmingly volatile. For example, in the United States, the price of electric utilities paid for natural gas fluctuated between \$2-\$3 per 1000 ft<sup>3</sup> for most of the 1980s and 1990s. Then, in 2000, gas prices started to climb and reached over \$8 per 1,000 cubic feet by December 2000. In January 2001 the price peaked at \$9.47 but by December 2001 they had fallen to \$3.11 [3]. The behavior of the prices of crude oil behaved similarly to the prices of natural gas during that time period as the price of crude oil went from \$10.60 in January 1999 to \$25.60 in January 2000 [2]. Fluctuations such as these have the ability to cause considerable economic damage and complicate financial planning and forecasting.

Technologies go through several stages as they progress from conceptual ideas to widespread use. They can be broken down into three major stages. Stage one is proof-of-technology. It involves moving from a concept to more detailed plans, and eventually to a working model, larger-scale test plant, and then an operating facility. The next stage is designing to market. This means fine-tuning the engineering and design, tailoring the performance to meet users' needs, and reducing cost, which is especially important for electricity generation. The third and last stage is market penetration. This is the stage in which the technology moves from a market ready idea to widespread use. Some renewable electricity-generating technologies are still at the proof-of-technology stage. However, many are at the third stage of development struggling to make the jump from a proven technology to widespread use. Some of these technologies include wind power, photovoltaics, biomass, landfill methane, and geothermal power.

It is misleading to talk about renewable energies as a whole without specifying exactly which technology is being discussed. This work focuses on renewable energy converted from incoming radiation from the sun, or solar energy. Photovoltaics (PV), convert sunlight into

electricity and have many attractive features. Photovoltaic devices are quiet, dependable, have no moving parts, no noise or waste products, can be quickly installed, and can be sized to power anything from a single bulb to an entire community. They are, however, quite expensive. Current costs are around \$0.20-\$0.40 per kWh for grid connected systems compared to \$0.03-\$0.05 per kWh for coal or natural gas. Costs have decreased drastically in recent years and will continue to decrease. However, at the moment, PV devices are nowhere near being cost-competitive with fossil fuels. Fortunately, these high costs haven't kept solar cell installations from booming. Photovoltaic production is growing worldwide at about 25% per year. Total electricity production from PV devices is minute in comparison to coal and other fossil fuels, but the use of solar cells in niche markets keeps growing which means continued technological and production advances leading to eventual decreases in price.

The solar resource is huge and could solely supply the world's energy needs many times over. For example, assuming a module conversion efficiency of 10%, a capacity factor of 22%, and insolation of 1 kW/m<sup>2</sup>, 14,000 square miles of PV panels (about 15% the land area of Nevada) could provide enough electricity for the entire United States, or 800 gigawatts. Obviously, a system like this would be immensely impractical. It wouldn't generate electricity at night and would require massive construction of new transmission lines. Fortunately, solar cells work anywhere the sun shines, not just Nevada. Clearly they will produce more electricity in sunnier areas with increased levels of solar insolation, but even on a cloudy day, there is enough sunshine to produce electricity. Of all the forms of renewable energy, photovoltaics are the least resource-constrained.

There are two basic types of PV modules, crystalline silicon and thin film devices. Crystalline silicon modules are used in almost all commercial-scale PV systems. Commercial

PV systems are those producing electricity for resale rather than for direct use. A crystalline silicon system consists of silicon and is mixed, or doped, with a small amount of a substance with a different number of electrons such as boron or phosphorous. As light hits the PV material, electrons dislodge and this movement of electrons creates an electric current.

Crystalline silicon modules have relatively high conversion efficiencies of approximately 12-14%. Efficiency is defined as the percentage of energy in the sunlight striking the module that is converted into electricity. Crystalline silicon modules are made from readily available materials, often from waste silicon from semiconductor chip manufacturing plants. Unfortunately, crystalline silicon modules are expensive to manufacture, which hinder the overall cost of solar energy based on those modules.

Thin film PV technology works on the same general principle as crystalline silicon modules but has the advantage of generating electricity from a very thin film. For example, thin film modules can be incorporated into building materials such as roofing tiles. Thin film PV devices typically require less material to manufacture than crystalline silicon and are easier to produce on a large scale. Although material and production costs are lower, current thin film photovoltaic devices have lower efficiencies than crystalline silicon modules. This is expected to change over the next five to ten years as thin film technologies advance.

Photovoltaic modules, also known as panels, can have a peak power output from of 50-300 W. Panels can be assembled into arrays, consisting of as little as two panels (for a small residential system) to thousands of panels for a utility-scale system of 100 kW or more. These panels are the fundamental component of a PV system but definitely not the sole component. PV systems consist of mounting brackets, supports, hardware, and inverters. The costs of these other components are significant often consisting of one-third to one-half of the total system costs.

In general, there is not a definitive answer to the cost of photovoltaic power as costs can vary widely. Some of the reasons for this variation come from the definition of cost itself, what parts are included, the size and application of the system, the proposed location of the system, when the system is built, and whether it is an actual or projected cost. Several studies have been carried out in order to paint a more complete picture of PV power and installation cost. An analysis of 220 grid-connected PV systems in the US found average first costs to be in the range of \$7,400 per kW [4]. The majority of systems analyzed are sized for rooftops and were approximately 4.9 kW in size and were installed around 1998. An analysis of 23 large-scale (>70kW) US PV systems found that costs for large PV systems are dropping and that this trend is likely to continue. PV system costs dropped by 31% from an average of \$1,035 per kW in 1996-1997 to an average of \$810 per kW in 1999-2000. The PV modules accounted for approximately two-thirds of the cost, while the remainder was for balance-of-system costs and installation.

Operating costs for photovoltaic systems are uncertain as there are few in operation. Fuel costs are zero and scheduled maintenance consists mostly of washing the modules to remove dust and dirt. Technical failures of the panels themselves are rare. Inverters have been a source of problems however they are showing improved reliability in recent years. One review found maintenance costs for actual grid-tied systems to vary from 0.4-9.5 US cents per kWh [5]. Making reasonable, but arguable assumptions, these costs add up to about 40 US cents per kWh, which assumes a first cost of \$8,000 per kW, \$0.01 per kWh in operation and maintenance costs, a 22% capacity factor, and a lifetime of twenty years. This is about ten times more expensive than that of new natural gas turbines. There are other published estimates that are lower than 40 cents per kWh, but are still higher than most fossil fuel-based technologies.

Despite the increased cost of solar energy, the photovoltaic market is booming. PV production worldwide grew from 70 MW in 1994 to over 200 MW in 1999. Technical advances in thin film production paired with a growing interest in photovoltaics, thin film devices in particular, will allow for the continued rapid growth of the PV market. As mentioned, the current issues hindering industrial-wide thin film deployment are manufacturing costs, outdoor reliability, and most importantly, efficiency. However, much progress and success on these drawbacks is taking place in laboratories around the world. Recently, efficiencies in excess of 17% have been reported for thin film devices based on  $\text{CuInSe}_2$ ,  $\text{CuGaSe}_2$ , and  $\text{CuInGaSe}_2$ . The major drawback holding back these devices, from an industrial point of view, lie in the manufacturing costs. Thin film devices are cheaper to manufacture than crystalline silicon cells, however they often require complex deposition procedures and strategies. Hence, this research focuses on improvement in the quality of these thin film materials along with growth of thin film solar cell constituents via cost saving methods.

Chapter 2 of this work provides a technology overview of photovoltaic devices. The physics of photodevices are discussed, including the photoelectric effect and the role of solar radiation and band gap in a solar cell device physics. Typical solar cell materials are discussed beginning with the most common silicon-based photovoltaic devices, followed by the emergence of thin film devices based on  $\text{CdTe}$ ,  $\text{CuInGaSe}_2$  alloys,  $\text{CdS}$  buffer layers, and transparent window layers such as  $\text{ITO}$  and  $\text{ZnO}$ . An overview of the two main deposition processes discussed in this work, chemical bath deposition and rf magnetron sputtering, are detailed, including fundamentals of CBD film growth to types of targets and sputter sources, respectively.

Chapter 3 details the methods and techniques used in this research. The stringent substrate cleaning procedure used on all samples is explained, along with the method for absorber layer

fabrication at UF. The apparatus used to chemically bath deposit ZnCdS buffer layers is discussed along with the sputtering system responsible for ZnO TCO growth. The large number of characterization techniques used in analysis of research in this work are detailed, which include inductively coupled plasma, x-ray diffraction, and secondary ion mass spectroscopy, for example. Last is a discussion on photovoltaic device performance physics and the techniques used to measure device performance, including the  $I$ - $V$  measurement and quantum efficiency techniques.

Chapter 4 presents work focusing on the growth and characterization of  $Zn_xCd_{1-x}S$  thin film buffer layers which are deposited via chemical bath deposition. The CBD process used to deposit ZnCdS is detailed including substrate and equipment cleaning, preparation of dose solutions, and bath temperature conditioning. The difference between the fractional composition of zinc in the prepared solution and the as-deposited films is compared, where the subscript  $p$ ,  $b$ , and  $f$  are used to denote fractional zinc concentration in the prepared dose solutions, the actual bath solution, and the as-deposited film, respectively. Prepared fractional concentrations of zinc ranging from  $x_p = 0.1$  to  $x_p = 0.5$  are deposited on Corning 1737 glass substrates and the resulting fractional composition of zinc in the film ( $x_f$ ) is reported. The addition of Zn to buffer layer thin films is important, as it has the ability to change the band gap of the film, thereby altering its optical transmission as ZnS has a larger band gap value than CdS. Therefore, it is important to know the correlation between prepared fraction of Zn and the amount of Zn that is actually deposited during the chemical bath process.

Chapter 5 details the sputter deposition of ZnO thin films, one of the most popular transparent conductive oxides used in solar cell applications. Although ZnO can be deposited by other methods such as spray pyrolysis or chemical vapor deposition, sputtering is generally the

preferred method of deposition and has the ability to produce high quality films at low costs. This work intends to improve upon the quality of ZnO, in particular H-doped and Al-doped ZnO, films by investigating a number of factors that affect film thickness, sheet resistance, optical transmission, and structural characteristics. Films deposited at higher base pressures of approximately  $2.5\text{-}3.0 \times 10^{-6}$  Torr are studied as higher base pressures have the potential to lower the cost of thin film PV devices, as an increase in industrial throughput can be achieved without the need for lower base pressures. The overall quality of Al:ZnO (AZO) and H-Al:ZnO (HAZO) sputter deposited films is characterized by a figure of merit calculation which takes into account resistivity and average transmittance from 400 nm to 800 nm. The figure of merit calculation provides an easy way to estimate the proposed effectiveness of a sputter deposited ZnO film for use in thin film solar cells or any other photodevice.

Chapter 6 takes the sputtering of AZO and HAZO thin films a step further and aims to investigate the effect of thermal treatment under three different ambient conditions, argon, nitrogen, and forming gas (96% N<sub>2</sub>, 4% H<sub>2</sub>). A brief discussion of the thermal annealing equipment is provided. Both AZO and HAZO films are annealed at 450 °C for one hour, with 10 min ramp and 15 min cool down cycles before and after, respectively. Structural, electrical, and optical characterization is performed to determine the effect of ambient gas on post-annealed AZO and HAZO films. Atomic force microscopy provides a look at surface roughness variations between as-deposited ZnO and those films subjected to thermal annealing treatment. Secondary ion mass spectroscopy is also employed to elucidate any depth profile changes which might result as a factor of the annealing treatments.

## CHAPTER 2 TECHNOLOGY OVERVIEW

### **Solar Cell Device Physics**

The design and materials used in fabricating a solar cell device is critical to its performance. Understanding the principals of photovoltaic device operation allow for a better understanding of how different materials can produce devices with a wide range of performance parameters. This chapter presents an overview of photovoltaic devices, the physics that drive their operation, and the most common parameters used to describe device performance.

#### **Photodevices**

There are two basic types of semiconductor photodevices, which are classified according to whether they convert electrical energy into photo-energy or vice-versa. Photodevices that convert photo-energy into electrical energy are termed photodetectors or solar cells, depending on whether the purpose of the energy conversion is to detect information regarding the photo-energy (photodetectors) or to produce electrical power (solar cells). The purpose of the second type of photodevice is to produce photo-energy from electrical energy. Light emitting diodes (LEDs) and laser diodes are two examples of this type of photodevice [6].

#### **The Photoelectric Effect**

The first conversion of photo-energy to electrical power is credited to Edmond Becquerel, who discovered the process in 1839. This conversion of sunlight to electrical energy at the atomic level has become known as the photoelectric or photovoltaic effect. The production of electricity by the photoelectric effect requires that a photovoltaic device, or solar cell, absorb a certain amount of light. The light radiation incident on solar cells is not always fully absorbed, as a percentage of the radiation can be reflected or pass through the device. Electrical energy is only the result of incident light that is absorbed by the solar device.

Once light is absorbed by a solar cell, its energy is transferred to electrons that use this energy to escape from their normal positions in the photovoltaic material. These electrons become free to flow as current through an electrical circuit. The force to drive the current through an external circuit is provided by a built-in electric field. This electric field is created by contacting an n-type semiconductor, which has a surplus of electrons, with a p-type semiconductor, which contains an abundance of holes. Joining these two materials creates a p-n junction, an example of which is pictured in Figure 2-1. When the n-type and p-type materials are contacted, a buildup of positive and negative charge occurs on the side of the n-type and p-type layer, respectively. This creates an electric field at the p-n junction that is capable of moving electrons towards the negative surface and holes towards the positive surface, thereby driving current through an external device. A band diagram depicting the creation of electrons and holes in a p-n junction via the photoelectric effect is shown in Figure 2-2 [7]. It can be seen that electrons travel to the n-type layer while holes travel to the p-type side of the junction.

### **Solar Radiation**

The Sun is the star at the center of our Solar System, and is responsible for providing energy to Earth in the form of sunlight. This sunlight is responsible for all natural processes, such as creation of fossil fuels via photosynthesis, and can be harnessed for use in synthetic processes, such as heating or electrical conversion via the photoelectric effect. The Sun has a surface temperature of approximately 5,800 K and therefore has a stellar classification of G2V. The surface of the Sun is believed to consist primarily of helium and hydrogen, with trace quantities of other elements.

The radiation spectrum emitted by the Sun is very closely approximated by blackbody radiation at 5,800 K, as can be seen in Figure 2-3 [6]. The solar radiation spectrum lies in the ultraviolet, visible, and infrared portions of the electromagnetic spectrum spanning 100 nm to

$10^6$  nm. The solar constant is defined as the amount of solar radiation that hits Earth per unit area. When measured at the outer surface of the Earth's atmosphere, the solar constant is approximately  $1350 \text{ W/m}^2$ . This level of radiation is termed Air Mass 0, or AM0, as it has yet to pass through the Earth's atmosphere. As the Sun's radiation enters the atmosphere it becomes subject to energy loss as a result of absorption and scattering, factors that are dependent on the incident angle of the incoming solar energy. The level of Air Mass incoming radiation experiences is calculated as

$$\text{Air Mass (AM)} = \frac{L_1}{L_2} = \frac{1}{\cos \theta} \quad (2-1)$$

where  $\theta$  is the solar zenith angle,  $L_1$  is the path length the solar energy actually travels, and  $L_2$  is the shortest possible path length. An Air Mass level of 1.5 ( $\theta = 48.19^\circ$ ) is most often used for photovoltaic device testing, which correlates to a solar constant of approximately  $1000 \text{ W/m}^2$ .

### **Band Gap Energy**

Solar radiation incident on photovoltaic material has the ability to free electrons from the material's crystal lattice. In general, only photons with a certain level of energy can free electrons. This energy level is required to free an electron is known as the band-gap energy, and is unique to each material. In cases where incident photons carry a higher energy than a material's band-gap energy, electrons are released along with the extra energy of the photons, which is given off as heat. This undesired heat is often difficult to avoid as a large majority of incoming solar radiation is either below the band-gap energy of the photovoltaic material, or carries excess energy.

### **Solar Cell Materials**

Photovoltaic devices can be manufactured from a variety of different semiconductor materials, including silicon, and polycrystalline and single crystalline thin films. Each of these

materials possess certain properties that allow their use in solar cell devices. The crystallinity of a photovoltaic material refers to the degree of order found in its crystal structure. Single crystalline, multicrystalline, polycrystalline, and amorphous semiconductor materials have all found use in photovoltaic devices. Absorption is an important property of solar cell materials and specifies the ability of a material to absorb incident light. The absorption coefficient of a material is typically a function not only of the material itself, but also of the wavelength of the light to be absorbed. If the energy of incoming radiation is below the band gap energy of the material, the light will not be absorbed. The band gap energy of a material refers to the minimum energy needed to free an electron, or more specifically, to move an electron from the low energy valence band to the high energy conduction band.

### **Thin Film Solar Cell Materials**

The solar cell market is currently dominated by crystalline and polycrystalline silicon. The price of traditional silicon based photovoltaic devices has been significantly reduced over the past few years as a result of increased production volume. Unfortunately, even economies of scale are not expected to aid silicon in meeting cost per watt efficiencies demanded by consumers and industry, which is typically in the range of \$3-5/Wp (watt peak power). Solar cell devices based on thin film technologies have made remarkable progress in terms of high conversion efficiencies, long-term stability, and industrial scale manufacturing capabilities, which is why thin film devices are believed to be capable of reaching the desired cost per watt goals.

Thin film technologies are gaining industrial interest as they have the possibility to drastically cut manufacturing costs as compared with traditional silicon cells. Photovoltaic devices based on thin film technologies use less material, generally require fewer processing steps, allow for simple device processing, and are capable of being cheaply manufactured for use

in large-area modules and arrays. The manufacturing cost reduction stems from the fact that design and manufacture of solar cells based on thin film technologies contain many common elements and steps.

In general, large scale manufacture of solar cells aims to choose a given technology based on high efficiency, ease of manufacture, reliability, material availability, and environmental sensitivity. Alloys of amorphous silicon (a-Si:H), cadmium telluride (CdTe), and multinary copper indium selenide (CIS) and its alloys with Ga are three thin film technologies that are the current leading contenders for large scale manufacture. Figure 2-4 shows the chronological evolution of conversion efficiencies of a-Si, CdTe, and CuInSe<sub>2</sub> thin film technologies from 1975 through 2005 [8]. In the figure it can be seen that CIS based thin film technology shows the promise of exceeding the required cost/performance levels to compete with other sources of energy. All three of these thin film technologies are only beginning to become commercialized on a large scale. Although leading on paper, CIGS based technology trails in commercialization with a current production capacity of approximately 100 kW/y compared to around 1 MW/y and 35 MW/y for CdTe and a-Si technologies, respectively.

### **Amorphous Silicon Alloys Solar Cells**

Among thin film technologies, p-i-n junction-type devices based on a-Si:H and its alloys are the most developed and commercially available, a result of specific technical properties of the material. They use the p-i-n type device configuration as a-Si:H and its alloys have intrinsically high defect densities and low minority carrier lifetimes, and require field assistance for collection of photoelectric generated carriers. Amorphous silicon and its alloys have high optical absorption coefficients of around  $10^5 \text{ cm}^{-1}$ , a band gap that can be adjusted from 1.1 eV to 2.5 eV depending on the level alloying, are fairly easy to fabricate with many different techniques under low temperatures, and are capable of being used in multijunction devices,

which are extremely efficient at utilizing incoming solar radiation. There are also a number of disadvantages of amorphous silicon thin film technology, such as severe cell efficiency degradation by as much as 15-20%. Electronic properties of the material also tend to degrade with increased deposition rates larger than a few Å/s, which limits throughput of device fabrication. Module efficiencies are typically lower than other thin film technologies, as seen in Figure 2-4. Significant amounts of research has helped to diminish these disadvantages and much progress has been made in achieving increased deposition rates and higher efficiencies.

### **Amorphous Silicon Growth Methods**

Many deposition techniques can be used to grow a-Si:H alloy materials for use in photovoltaic devices. Some of the most common techniques include sputtering, plasma-enhanced chemical vapor deposition (PECVD), electron-cyclotron resonance glow discharge (ECR), photo CVD, and plasma CVD. Plasma-enhanced chemical vapor deposition is perhaps the most widely used deposition method, however it suffers from very low deposition rates, especially of i-layer amorphous silicon, which is the bottleneck for all deposition techniques. These low deposition rates, around 1-2 Å/s, are not desirable for commercial purposes as they negatively affect throughput and do not result in cost reduction. Extensive efforts have been aimed at increasing growth rate of the i-layer, and increased deposition rates of 10 Å/s [9] and up to 15 Å/s [10] have been achieved using very high frequency RF plasma-enhanced chemical vapor deposition (VHF-PECVD).

Higher deposition rates of a-Si:H alloys have been achieved with a hot-wire chemical vapor deposition process (HWCVD), with device quality films grown at rates up to 167 Å/s. The HWCVD process has been used to create a-Si:H devices with efficiencies of 5.5% at 18 Å/s, 4.8% at 35 Å/s, 4.1% at 83 Å/s, and 3.8% at 127 Å/s [11]. Although efficiencies decrease, the HWCVD technique is capable of increasing deposition rates, thereby increasing throughput and

possibly decreasing cost. Unfortunately, cells fabricated by the HWCVD process have exhibited significant photoinduced degradation. Very high deposition rates of 0.3  $\mu\text{m/s}$  to 1.6  $\mu\text{m/s}$  have been achieved using an atmospheric pressure plasma CVD technique which employs 150 MHz VHF power to generate a plasma of a He, H<sub>2</sub>, and SiH<sub>4</sub> gas mixture [12]. Despite the high quality films produced at high deposition rates, this atmospheric pressure plasma CVD process has not been used for photovoltaic device fabrication.

### **Copper Indium Diselenide**

Research of semiconductor materials for thin film devices has extended to the investigation of ternary and quaternary materials where CuInSe<sub>2</sub>-based solar cells are being considered a promising potential. CuInSe<sub>2</sub> is a direct band gap material with excellent photovoltaic properties as a polycrystalline absorber layer for thin films. CIS has a band-gap energy between 1.5 eV and 1.55 eV, smaller than the band-gap of silicon but an excellent match for the solar spectrum [13]. Efficiency ( $\eta$ ) of the conversion process is a basic parameter that is used to evaluate all solar cells. Thin film solar cells based on CIS have achieved 12.2% total area efficiency in 1996 [14] and 11.4% total area efficiency prepared by rapid thermal processing in 2001 [15]. The maximum theoretical efficiency of CIS is 28.5% [16]. The efficiency of CIS devices is assisted by its ability to invert via deposition of CdS and become n-type even though the bulk of the sample is p-type.

CIS devices normally have a low open circuit voltage (0.729 V) to band gap ratio compared to silicon devices and a large short circuit current creating a relatively large series resistance loss and compromising cell performance [17]. From 1978-1981, efficiencies of CIS cells increased from approximately 4% to 10%. This improvement stemmed from the research

efforts that went into solar cells as a result of the energy crisis of the 1970s. Research has continued to today resulting in the variety of commercial products now available [18].

Absorbance of CIS can be as high as  $10^5 \text{ cm}^{-1}$ , making it the most light absorbing semiconductor known. With CIS, it is possible to achieve high efficiencies with considerably less material consumption than traditional PV technology. Only half a micron of CIS is sufficient to absorb 90% of incoming photons [19]. PV devices created with CIS exhibit long life and consistent performance as a result of the excellent stability and radiation hardness of CIS [20]. CIS efficiencies have reached 18.8% for lab-sized cells and over 10% for complete modules [21]. Siemens Solar Industries have recently entered the market as a commercial product for terrestrial applications with CIS-based devices [22]. These applications include generating power for remote locations, generating power for developing countries without suitable power infrastructures, and the space industry.

### **Copper Gallium Diselenide**

The ternary compound, copper gallium diselenide (CGS), has a relatively large band gap of 1.7 eV [13] and a high absorption coefficient of  $\alpha = 3 \times 10^4 \text{ cm}^{-1}$  at 1.7 eV [23]. CGS is a member of the I-III-VI<sub>2</sub> semiconductors. CGS band gap energy will decrease as the Cu/Ga ratio increases [24]. The theoretical limit for CGS device efficiency is 26%, however only recently have CGS-based solar cells overcome efficiencies of 6.2% [25]. Now, efficiencies have reached 9.7% for single crystal devices and 9.3% for thin films [26]. Both of these recorded values are still well below the theoretical limit.

In comparison to the rapid progress made with CIS and CIGS based solar cells, the efficiency of CGS cells are still low, even though CGS cells have been investigated for more than 25 years. The most recognized downfall of CGS based solar cells is the low open-circuit

voltage compared to the band gap. Theoretically, CGS-based photovoltaic devices should be capable of producing an open-circuit voltage of approximately 1.2 V. However, in practice, solar cells with CGS absorbers have been limited to open-circuit voltages of 0.9 V and 0.75 V, using Ga-rich and Cu-rich absorber layers, respectively [27, 28]. Decreased defect densities and a decrease in tunneling-enhanced recombination has been determined as the cause for improved device performance of Ga-rich CGS films [29].

CGS wide gap chalcopyrites have material and growth related defects that limit device performance. CGS tends to exhibit a tetragonal structure, as a result of this arrangement it is susceptible to a large concentration of vacancies and anti-site defects. Slightly Cu-poor CGS absorbers have shown to have better performance than stoichiometric ones. For Cu-rich CGS, deviation from stoichiometry is facilitated by the formation of a second phase, and therefore the material develops more defects.

CGS is often used as a top cell in tandem cells. It responds to the short wavelength portion of the solar spectrum. In addition, it allows long wavelength photons to pass through and reach the bottom layer of the tandem cell, often a CIS layer. It has been estimated that a CGS/CIS tandem structure could reach efficiencies greater than 30%.

### **Copper Indium Gallium Diselenide**

Adding gallium to copper indium diselenide forms a  $\text{CuIn}_{1-x}\text{Ga}_x\text{Se}_2$  alloy known as CIGS and can increase the band gap energy to approximately 1.7 eV therefore enhancing the open-circuit voltage of the solar cell creating a higher performing device. The Ga content can be adjusted with the goal of optimizing the CIGS absorber band gap profile, improving the open-circuit voltage, and the short-circuit current. High performance CIGS-based devices generally require an extremely high temperature to produce the absorber layer, the reasons for which are not entirely clear.

CIGS cells have reached higher efficiencies than CGS-based thin film devices. The maximum conversion efficiency achieved for a CIGS thin film solar cell is 19.5% ( $V_{OC} = 0.694$  V,  $J_{SC} = 35.2$  mA/cm,  $FF = 79.7\%$ ), which was constructed at the National Renewable Energy Laboratory [30]. NREL was also the first to reach efficiency greater than 20% for a CIGS thin film solar cell. The maximum theoretical efficiency for a single junction CIGS solar cell is 27.5% [16].

### **Cadmium Sulfide**

In fabrication of thin film photovoltaic devices, deposition of the buffer layer occurs on top of the absorber layer. The buffer layer of a solar cell is intended to prevent diffusion of impurities into the absorber layer from deposition of the transparent conducting oxide layer. The most common buffer layer for high efficiency devices is a CdS buffer layer, although interface passivation and the establishment of an inverted region in the absorber are other proposed benefits [31]. CdS buffer layers are highly resistive and are most often deposited via chemical bath deposition, although other techniques are very common such as the successive ionic layer adsorption and reaction (SILAR) technique.

The band gap of CdS is very low, 2.4 eV, and is not able to transmit all useful incoming radiation. Therefore, optimization of device structures based on the thickness of the CdS buffer layer is necessary, as unacceptable absorption occurs if the CdS buffer layer is too thick, blocking out a large section of incident photons. This absorption results in poor device performance as a result of decreased short-circuit current. On the other hand, the device open-circuit voltage can be hampered if the deposited CdS buffer layer is too thin [32]. Diffusion of cadmium ions into CIGS absorber layers is thought to create such high efficiencies by formation of a pn-junction.

Although CdS is perhaps the most widely used buffer layer, one of the main problems of CdS technology is its relatively low band gap value of 2.4 eV. This reduces the current that can be collected as there is a constraint on the short wavelength portion of the solar spectrum that reaches the absorber. For higher band gap cells, this limit of the short wavelength part of the solar spectrum can become a severe hindrance for device performance [33].

### **Zinc Sulfide**

Zinc sulfide is an attractive alternative buffer layer on CGS-based thin film solar cells as it exhibits a wide optical band-gap energy (3.8 eV) [34] coupled with the fact that ZnS raises fewer ecological concerns than CdS. Photovoltaic devices fabricated with ZnS buffer layers have reached efficiencies of 18.6% [35]. Unfortunately, the ZnS comes with some downfalls, such as the difficulty of ZnS diffusion into CIGS films compared to CdS. An external force, such as heat, is required to enhance the diffusion into CIGS to create the buried p-n homojunction. Compared to the best performing CdS/CIGS solar cells with a total area efficiency of 19.5% AM1.5G, ZnS-based buffer layers are a very promising replacement for CdS buffer layers on CIGS cells [36].

### **Zinc Cadmium Sulfide**

Zinc cadmium sulfide is used as an alternative to CdS buffer layers in an effort to produce a more environmentally friendly CIGS solar cell by reducing the amount of the toxic cadmium component used. These ZnCdS buffer layers also have the best lattice matching to CGS absorber layers. Addition of Zn to CdS results in a band-gap energy that is between CdS (2.4 eV) and ZnS (3.8 eV). The result of this increased band-gap energy is increased short-circuit current in the short wavelength region.

In an effort to maximize photovoltaic device potential, absorber and buffer layers electron affinities should match, yielding an increase in the open-circuit voltage. A loss of current occurs

in cells fabricated with CdS buffer layers and CGS absorber layers as CdS has a larger electron affinity, 4.5 eV for CdS and 3.9 eV for CGS. Adding Zn to CdS buffer layers results in electron affinity ranges from 3.7 eV to 4.5 eV. Substituting ZnCdS for CdS buffer layers minimizes current loss in the cell and maximizes the open-circuit voltage. Another benefit of the addition of Zn to CdS is the improved lattice matching to CIS and CGS based absorbers. Addition of zinc decreases the lattice parameter of ZnCdS from 5.82 Å (CdS) to 5.42 Å (ZnS), which more closely matches that of CGS (5.61 Å) and CIS (5.78 Å). Although increased lattice matching is beneficial, the increase in Zn content also results in films with increased resistivity [37]. It has been proposed that a ZnCdS buffer layer film with 30% zinc content should be a successful buffer layer for CGS absorbers [38].

### **Zinc Selenide**

Zinc selenide is another buffer layer that is good for use in a wide band-gap CGS solar cell. It provides another alternative buffer layer to replace the use of toxic CdS in CIGS photovoltaic devices. Zinc selenide is a wide band-gap materials with a band-gap energy of 2.7 eV [34]. The deposition of ZnSe (5.668 Å) buffer layers on CGS (5.614 Å) absorber material creates a practically strain-free interface with a lattice mismatch of less than 1%. This is a large improvement in comparison to the lattice mismatch of approximately 4.2% between CdS and CGS. Unfortunately, conversions efficiencies using ZnSe are much lower than those using CdS, as CGS solar cells using ZnSe buffer layers deposited by MOVPE have only reached 3.3% conversion efficiency [39]. Using CIGS absorber layers, conversion efficiencies of 13.7% have been obtained with ZnO/ZnSe/Cu(In,Ga)(S,Se)<sub>2</sub> device structures [40]. Further experimentation of ZnSe buffer layers is needed in order to increase solar cell conversion efficiencies.

## Indium Tin Oxide

Indium oxide, doped with tin (ITO), was developed in the early 1950s and has the lowest resistivity, on the order of  $\sim 1 \times 10^{-4} \Omega \cdot \text{cm}$ . Indium tin oxide is the most widely used transparent conductive oxide in optoelectronic devices [41], as they have been studied extensively because of their combined unique transparent and conductive properties. Indium tin oxide thin films were the first TCOs that were actually useful in any practical application.

A stable supply of ITO may be difficult to achieve for the growing market of optoelectronic devices due to the expense and availability of indium [42]. Half of the indium worldwide is used in flat panel display applications [41]. This problem is compounded by the fact that the amount of indium available in nature is very small causing it to be quite and expensive material. There are no mines built specifically to remove indium from nature due to the trivial amount available, it is only obtained as a byproduct from zinc mines and other metals. In 1995, the price of indium spiked at \$550 per kilogram, creating economical as well as technically motivation for the creation of alternative transparent conductive oxides.

Indium tin oxide thin films are highly degenerate n-type semiconductors with low electrical resistivity. The low resistivity of ITO is due to a high carrier concentration as a result of the Fermi level being located above the conduction level [41]. Several deposition techniques can be used to deposit ITO thin films, such as chemical vapor deposition, magnetron sputtering, evaporation, and spray pyrolysis. These techniques require either a high substrate temperatures during deposition or high temperature thermal treatment, annealing, after deposition. These high temperatures often cause damage to the surface of both the substrate and the film. Deposition of ITO in the manufacturing environment is usually performed by dc-magnetron sputtering. The choice of target materials, ceramic or metal, is dependant of the film quality sought and the amount of process control available. Variables that are adjusted during process optimization

include oxygen partial pressure, total gas working pressure, residual water vapor partial pressure, substrate and target temperature, sputter power, and target composition and configuration.

### **Zinc Oxide**

Zinc oxide thin films were developed in the 1980s as an alternative to ITO with similar resistivity. Zinc oxide is one of the few metal oxides that can be used as a transparent conductive oxide. It has advantages over other materials such as  $\text{In}_2\text{O}_3$  and  $\text{SnO}_2$  due to its unique combination of interesting properties. Zinc is abundant, inexpensive, non-toxic, has good electrical, optical, and piezoelectric behavior, and is stable in a hydrogen plasma atmosphere. It is a wide band-gap semiconductor with a band-gap energy of 3.43 eV. Techniques such as sputtering, spray pyrolysis, and chemical vapor deposition have been used to deposit intrinsic zinc oxide thin films. Aluminum and gallium doped zinc oxide films have recently received attention for use as transparent electrodes in thin film solar cells with resistivity on the order of  $1 \times 10^{-4} \Omega \cdot \text{cm}$  have been achieved. It has been found that at temperatures greater than  $150^\circ\text{C}$  the electrical properties of zinc oxide become unstable. This problem can be resolved by using extrinsically doped films.

Thin film ZnO can be deposited with extremely high transparency while still maintaining high conductivity, especially when doped with aluminum or gallium. The high transparency of zinc oxide films allows for increased transmission in solar cells allowing more light to reach the absorber layer, resulting in the creation of more electron-hole pairs. Conductive ZnO films easily form ohmic contacts with aluminum. This ohmic contact is essential for collecting the current generated from photovoltaic devices. The use of ZnO has been researched extensively for use in other applications such as organic light-emitting diodes and transistors. Thin films of zinc oxide have most often been prepared using various techniques such as spray pyrolysis, evaporation, chemical vapor deposition, and sputtering.

## Chemical Bath Deposition

The deposition of materials via chemical bath deposition is a technique that has been in use as far back as 1835, when CBD was used to deposit silver in the fabrication of mirrors. In CBD, chemical deposition occurs on a solid substrate from a reaction that occurs in a chemical bath solution. The deposition can proceed along different pathways depending on whether the reaction in solution occurs homogeneously, heterogeneously, or via decomposition of a complex. The type of reaction pathway must be known in order to understand how to control the rate of growth, especially when stoichiometry of the deposited material is important.

### Fundamentals

The solubility product of a salt is a fundamental concept behind the mechanics of chemical bath deposition. A sparingly soluble salt, such as CdS, when dissolved in water will result in the following equilibrium



where CdS is in the solid phase. The small concentration of  $Cd^{2+}$  and  $S^{2-}$  ions that are present in the solution is given by the solubility product

$$K_{sp} = [Cd^{2+}][S^{2-}] \quad (2-3)$$

which is defined as the product of the ion concentrations.

As a salt become more soluble, the concentration of dissolved ions increases which results in a larger solubility product  $K_{sp}$ . Since the number of ions dissolved affects the size of the solubility product, it can be more accurately written as

$$K_{sp} = [M^{n+}]^a [X^{m-}]^b \quad (2-4)$$

where the dissolution of salt MX results in the following equilibrium



The solubility products of many popular chemically bath deposited compounds are listed in Table 2-1. Cadmium sulfide and zinc sulfide, two compounds studied in this research, have solubility products of  $K_{sp} = 1 \times 10^{-28}$  and  $K_{sp} = 3 \times 10^{-25}$ , respectively.

The majority of chemical bath deposition reactions are conducted in alkaline solutions. Under these conditions the concentration of  $\text{OH}^-$  can impede deposition of the desired compound. For example, water at  $\text{pH} = 10$  has an  $\text{OH}^-$  concentration of approximately  $9 \times 10^{-4}$  at  $60^\circ\text{C}$ . With such a high concentration of ions, the precipitation of metal hydroxides removing metal ions from solution becomes a problem. Therefore, a complexing agent, or ligand, is often added to the solution in order to prevent precipitation of the metal hydroxide. Addition of the complexing agent also serves the secondary purpose of impeding bulk precipitation of the desired compound by reducing the concentration of the free metal ions. Ammonium hydroxide is often used as a complexing agent for the chemical bath deposition of cadmium, and forms a cadmium tetraamine complex given as



with a solubility product of

$$K_{sp} = \frac{[\text{Cd}(\text{NH}_3)_4^{2+}]}{[\text{Cd}^{2+}][\text{NH}_3]^4} = 1.3 \times 10^7. \quad (2-7)$$

## Nucleation

Nucleation is a physical process that describes how precipitate particles of a compound will form once the solubility product is surpassed by the concentration of ions in solution. Thermodynamics and kinetics play a large role in determining the precipitation of dissolved ions. This precipitation can occur via homogenous or heterogeneous nucleation, which refer to nuclei formation in the solution or on a substrate, respectively.

Homogeneous nucleation generally refers to precipitate in the bulk solution. First, embryos are formed from the collision of molecules or individual ions. Embryos are not considered nuclei at this stage as they are typically unstable and have the ability to redissolve. The embryos can grow in size as a result of additional collisions with ions or molecules, or with other embryos, which necessary in order to form stable nuclei. If an embryo is too small, it will be thermodynamically unstable as a result of high surface energy and have an increased likelihood of redissolution. Low temperatures aid in the formation of thermodynamically stable nuclei by kinetically stabilizing smaller embryos long enough to grow in size. A critical radius exists where particles have an equal chance of forming stable nuclei or redissolving into solution, and is a function of volume and surface energies of the embryo. The surface energy required for embryo formation is

$$E_s = 4\pi\sigma R^2 \quad (2-8)$$

where  $\sigma$  is surface energy per area and  $R$  is embryo radius. When an embryo is formed the amount of energy released is

$$E_v = \frac{4}{3}\pi\rho HR^3 \quad (2-9)$$

where  $H$  is the heat of solution and  $\rho$  is solid density. In general, the average critical radius is around 100 molecules, which is approximately 0.5 nm to 1 nm.

Heterogeneous precipitation occurs when ions or unstable embryos precipitate, or absorb, onto a surface or substrate. In this case, nucleation occurs on an interface and there requires less energy than homogeneous nucleation, which tends to require a high degree of supersaturation in order to form stable nuclei. As a result, heterogeneous nucleation is energetically favored and generally dominates homogenous nucleation. Nuclei absorbed onto a surface can increase in size

by addition of particles from the solution or surface diffusion. In many cases it is possible for individual ions to chemisorb onto substrates to create nuclei that can further react and grow.

Solid precipitate in the solution is not always evidence of homogenous nucleation and growth. Inherently, heterogeneous nucleation will result in film growth on all surfaces in a chemical bath deposition reaction vessel, which includes any contamination that may be present in the system. Any foreign material present in the solution will act as heterogeneous nucleation sites. These particles can then collide with other embryos or surfaces, which leads to the possibility of sample contamination. Therefore, it is extremely important that chemical bath solutions be well filtered to prevent pollution of the sample with foreign particles.

### **Film Growth**

The film growth mechanism of chemically bath deposited films is generally divided into two main categories. The first involves reaction of free ions in solution, known as the ion-by-ion mechanism. The second involves the clustering of molecules that eventually result in the formation of film particles or crystals, known as the hydroxide cluster mechanism.

### **Ion-by-ion mechanism**

The sequential reaction of free ions in solution is the basis of the ion-by-ion mechanism, and is generally considered the mechanism responsible for the majority of film growth. Heterogeneous nucleation occurs on all surfaces present in the chemical bath deposition reaction vessel. Van der Waals and electrostatic interaction are primarily responsible for adhesion of one particle to surfaces or one another. These interactions result in film adhesion to a variety of surfaces, including hydrophobic materials such as Teflon. Film growth is slowest during the initial nucleation stage, as deposition occurs faster after nuclei have formed on a given surface. Once nuclei are formed, crystals grow until terminated by absorption of foreign particles from solution or steric hindrance by nearby crystals.

A schematic showing the deposition and growth of cadmium sulfide crystals via the ion-by-ion mechanism is shown in Figure 2-5 [43]. First, cadmium and sulfide ions diffuse through the solution towards the surface or substrate. Once reached, the surface aids in nucleation of the ions and CdS nuclei form. The flux of cadmium and sulfide ions to the surface continues which results in formation of new nuclei or further growth of CdS crystals. Finally, crystals continue to grow in size until growth is terminated by steric hindrance or absorption of foreign particles.

### **Hydroxide cluster mechanism**

Nucleation via the hydroxide cluster mechanism is considered simpler than ion-by-ion growth, as the solid phase is already present in the form of a metal hydroxide. Deposition begins with the adhesion of this metal hydroxide to the surface or substrate. These clusters are then converted in deposits of the desired compound. Film growth proceeds by the adhesion and conversion of additional metal hydroxide clusters to bare substrate or deposits that have already been converted. Also, metal hydroxide clusters exist in the bulk solution where they can be converted without adhering to any surface or substrate. In general, the hydroxide cluster mechanism results in a small crystal size distribution as compared to ion-by-ion growth where crystal growth can proceed via nuclei already present.

A schematic depicting the hydroxide cluster mechanism applied to the chemical bath deposition of cadmium sulfide is shown in Figure 2-6 [43]. First, cadmium hydroxide clusters present in the solution slowly diffuse towards and adhere to the surface or substrate. Sulfide ions react with cadmium hydroxide clusters, both in solution and adhered to the surface. The reaction results in the inward exchange of hydroxide ions by sulfide ions, and continues until essentially all of the hydroxide ions are replaced. The resulting clusters aggregate on the surface or substrate to form the cadmium sulfide film.

## **Sputter Deposition**

Sputtering is a complex subject that involves many physical and chemical processes that are all interrelated. Although many complex details of the process remain unknown, sputter deposition is a widely used technology that finds many applications in research and industry, including optical coatings for mirrors and filters, solar cells, magneto-optical storage media, transparent conducting electrodes, and wear-resistant coatings. There are many advantages of sputter deposition that are the cause for its popularity, including the ease with which research-level results can be scaled to industrial processes. Sputter deposited films generally exhibit excellent film uniformity, even over larger substrates, and film thickness and roughness can generally be well controlled. Film uniformity is dependant on source geometry and size, operating pressure, and target-to-substrate distance. Substrate motion and aperture masking (uniformity shields) are both used to improve film uniformity. Films can be deposited with nearly bulk-like properties at high growth rates and show excellent adhesion to a variety of substrates. Sputtering is a kinetic process involving momentum exchange, not a chemical process, and is therefore extremely versatile in its implementation.

There are two main sputter sources used in sputtering, glow discharge sources and ion beam sources. Glow discharge sputter sources include diode, triode, and magnetron sputtering. Although each source has its own configuration and set of advantages, they all function on the same basic mechanism, exchange of momentum between energetic particles and surface atoms, in order to eject particles. Planar magnetron sources are perhaps the most widely used sputter source due to their high efficiency and scale-up ability, however nonmagnetron sources, such as ion beam and rf planar diode sources, are extremely common. Although ion beam sources are typically used for sputter deposition, they can also be used for etching applications.

## **Chamber Features**

Sputtering is a fairly mature technology that is used in a number of industrial applications. Its industrial popularity stems from the straightforward setup of these sputtering system, which all feature very similar components, regardless of application or material being deposited. A schematic depicting the most common features of sputtering systems is shown in Figure 2-7 [44]. Most sputtering vacuum chambers are composed of stainless steel or mild steel. A high vacuum pump is attached to the system to achieve a base system pressure on the order of  $1 \times 10^{-6}$  Torr or lower, depending whether ultrahigh vacuum conditions are necessary. Multiple pressure gauges, including thermocouple, convectron, capacitance monomers, and ion gauges, are typically used to provide accurate measurement in both high and low vacuum conditions.

Mass flow controllers and throttle valves are two methods employed to maintain the working pressure necessary for sputter deposition. Generally, downstream pressure control (throttle valves) is considered superior to upstream control of gas flow (mass flow controllers), although in practice throttle valves are set at a fixed value and the working pressure is controlled upstream. Most systems can generally accommodate a large number of samples and are capable of substrate heating during deposition. Sputtering of numerous samples is accomplished by placing samples on a circular platen that allows multiple samples to be deposited by rotating the platen under the target. Bombardment, or etching, of samples can be accomplished by applying a bias to the substrate holder.

## **Targets**

The sputter target is an integral part of the system that dictates what materials can be deposited and under what conditions. Planar targets are composed of a wide range of materials, and are fabricated by mechanical, sintering, and metallurgical techniques. Two-source sputtering is possible, where two targets are used to sputter deposit a film, which requires substrate rotation

through both target deposition regions. However, the best results are obtained when using targets with alloy compositions identical to those of the desired film. Perhaps the largest concern related to targets is incomplete utilization of target material, especially in magnetron setups. Water-cooling is required for most magnetron sources, where oversize targets are required in order to achieve sufficient cooling. As a result, erosion tracks are generally significantly smaller than target diameters, and therefore target utilization of 25% or less is extremely common.

### **Sputter Sources**

There are two main categories of sputter sources, glow discharge and ion beam sources. Among them, they can be further separated into nonmagnetron and magnetron sputter sources, which use a magnetic field in order to alter the sputter source, target, and substrate interactions.

#### **Nonmagnetron sputter sources**

The simplest sputter source is the planar diode, a disc-shaped cathode target consisting of the material of interest, approximately 5 to 10 cm in diameter. The target is bonded, either by solder or conducting epoxy, and generally water-cooled. The target is protected by a ground shield, which acts to protect the target from sputtering of the support structure and side of the target.

The efficient use of target material in diode sputtering is one of its largest advantages. The diode electrodes are fairly large and the resulting electric field between them is extremely uniform, which results in an ion flux that is almost constant over the entire target surface. On the other hand, the inefficient use of secondary electrons is a large disadvantage of the diode technique. With a diode sputter source, substrates will be bombarded with energetic electrons, which can result in increased substrate temperatures. As a result, diode sputtering is limited to decreased deposition rates as compared to other sputter sources capable of low-pressure operation.

A triode source improves on the diode source by adding a heated filament. This filament provides electrons that are independently able to sustain the glow discharge, which greatly increases ionization efficiency. The advantage of the triode source is that the discharge is able to operate at lower pressures and voltages, and therefore is capable of much higher deposition rates as compared to planar diodes. In some cases, systems that operate with reactive gases can shorten the lifetime of the filament.

### **Magnetron sputter sources**

Magnetron sputtering is capable of coating heat-sensitive materials as its generally considered a 'cold' deposition process. Magnetron sputter sources operate by combining the electric field with a magnetic field of approximately 50 to 500 gauss. This combination is able to control secondary electrons, and confines them to drift in front of the target surface, which results in greatly increased efficiency. As a result, magnetron sputter sources can operate at low pressures and voltages. However, a large disadvantage of the magnetron configuration is the poor utilization of target material, as the erosion of the target is non-uniform. The typical magnetron setup utilizes at most 30% of the original target material. By rotating the target with respect to the magnets, it's possible to increase target utilization to values of 90% or greater.

### **Ion beam sputter sources**

Ion beam sputter sources are unique for a number of reasons. Most setups offer complete isolation of the substrates from the ion generation process and therefore minimal interaction between processes occurring at the target and substrate, respectively. As a result, substrate heating is kept to a minimum. Ion beam sources also offer control of the ion impact angle and spot size along with independent control of ion energy and current density. The sources require low background pressure, which results in less scattering of sputtered particles and gas incorporation. The most common ion beam source is the Kaufman source, which is capable of

providing an Ar ion beam up to 10 cm in diameter, with an energy range between 500 and 2,000 eV.

Table 2-1. Approximate solubility product of commonly chemically bath deposited compounds.

Compound	Solubility Product ( $K_{sp}$ )	Compound	Solubility Product ( $K_{sp}$ )
AgCl	$2 \times 10^{-10}$	CuSe	$2 \times 10^{-40}$
AgBr	$8 \times 10^{-13}$	In(OH) <sub>3</sub>	$6 \times 10^{-34}$
AgI	$1 \times 10^{-16}$	PbS	$1 \times 10^{-28}$
Cd(OH) <sub>2</sub>	$2 \times 10^{-14}$	SnS	$1 \times 10^{-26}$
CdS	$1 \times 10^{-28}$	SnS <sub>2</sub>	$6 \times 10^{-57}$
CdSe	$4 \times 10^{-35}$	SnSe	$5 \times 10^{-34}$
CdTe	$1 \times 10^{-42}$	Zn(OH) <sub>2</sub>	$1 \times 10^{-16}$
Cu <sub>2</sub> S	$1 \times 10^{-48}$	ZnS	$3 \times 10^{-25}$
CuS	$5 \times 10^{-36}$	ZnSe	$1 \times 10^{-27}$

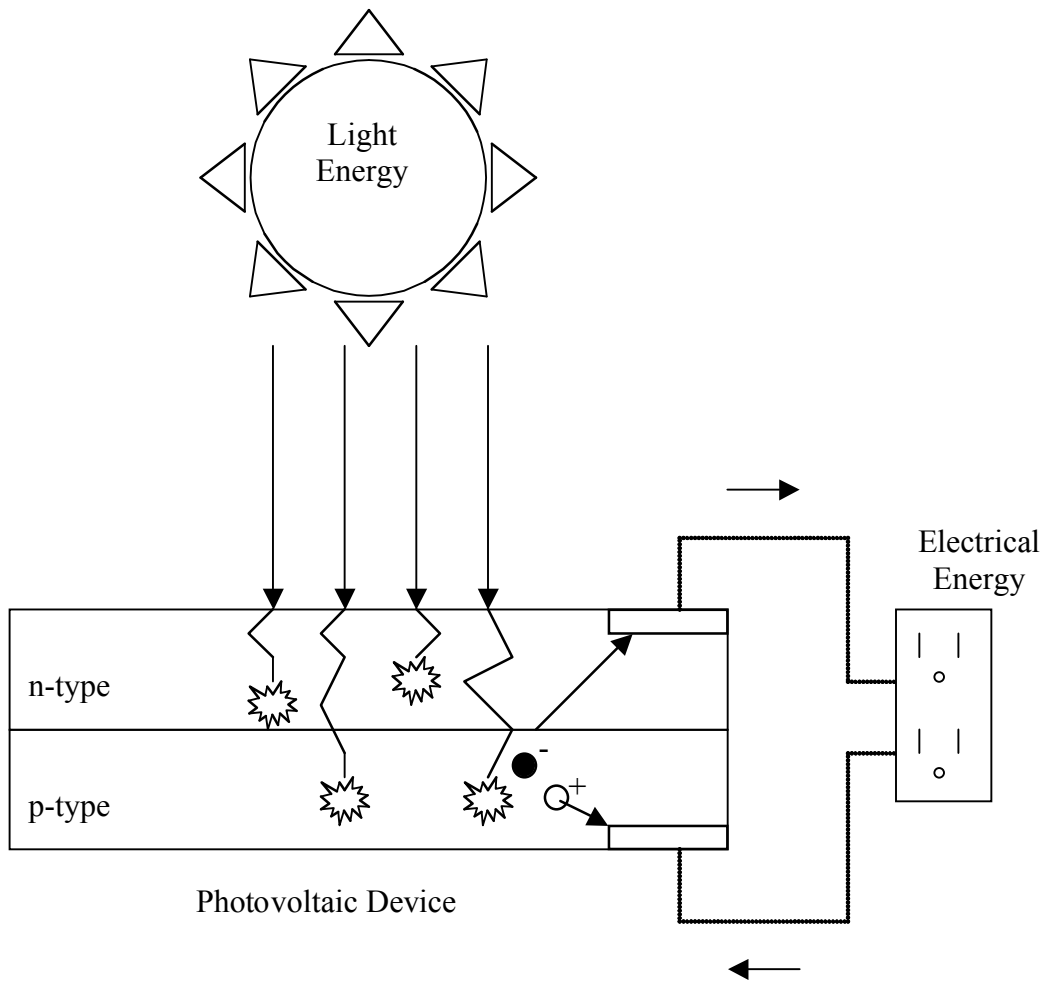


Figure 2-1. A p-n junction photovoltaic device.

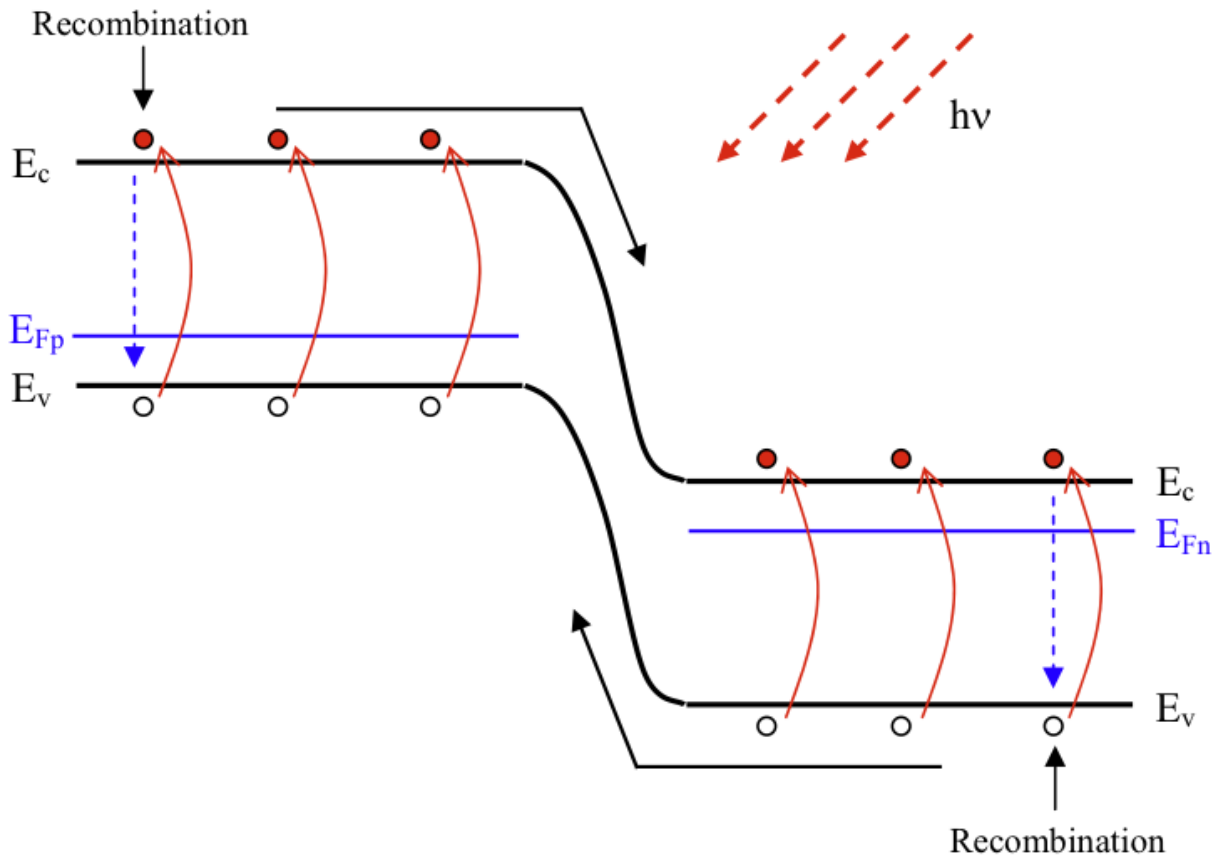


Figure 2-2. Band diagram of the photoelectric effect in a p-n junction photodiode.

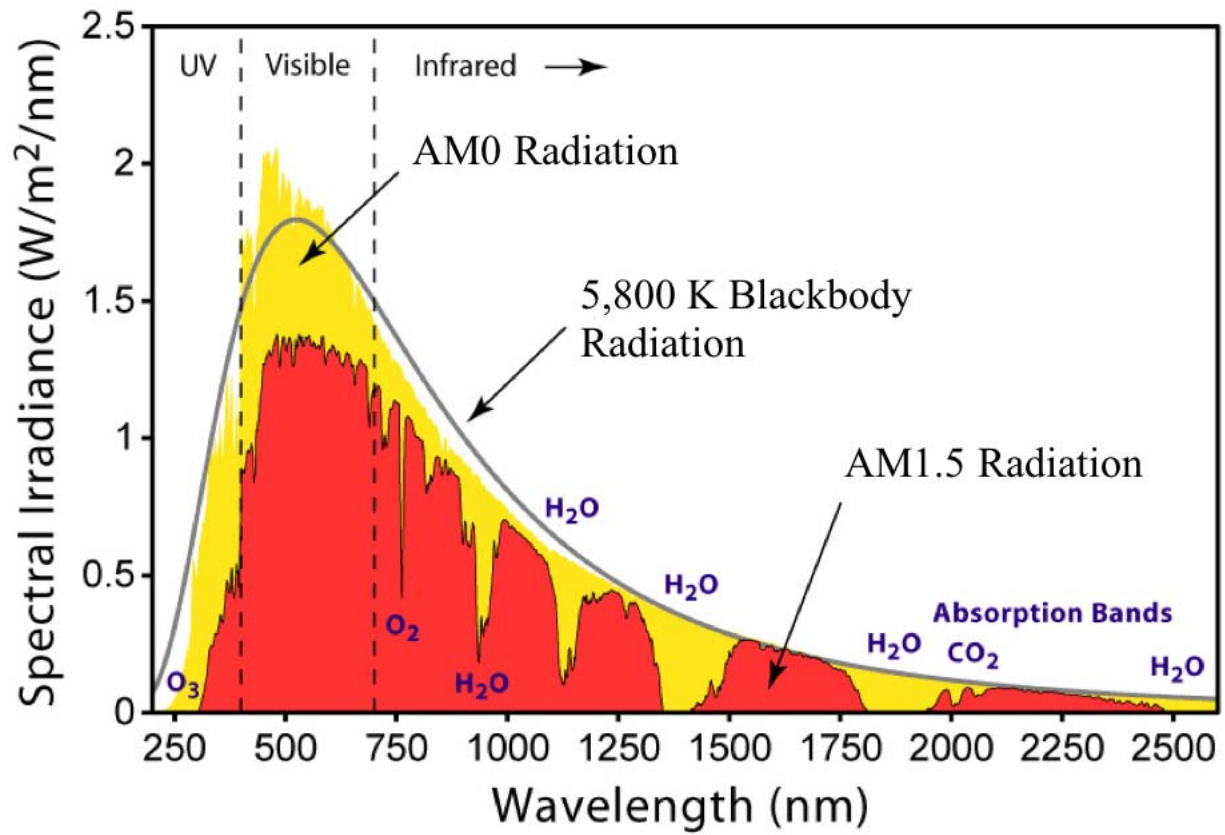


Figure 2-3. Solar spectrum at AM0 and AM1.5.

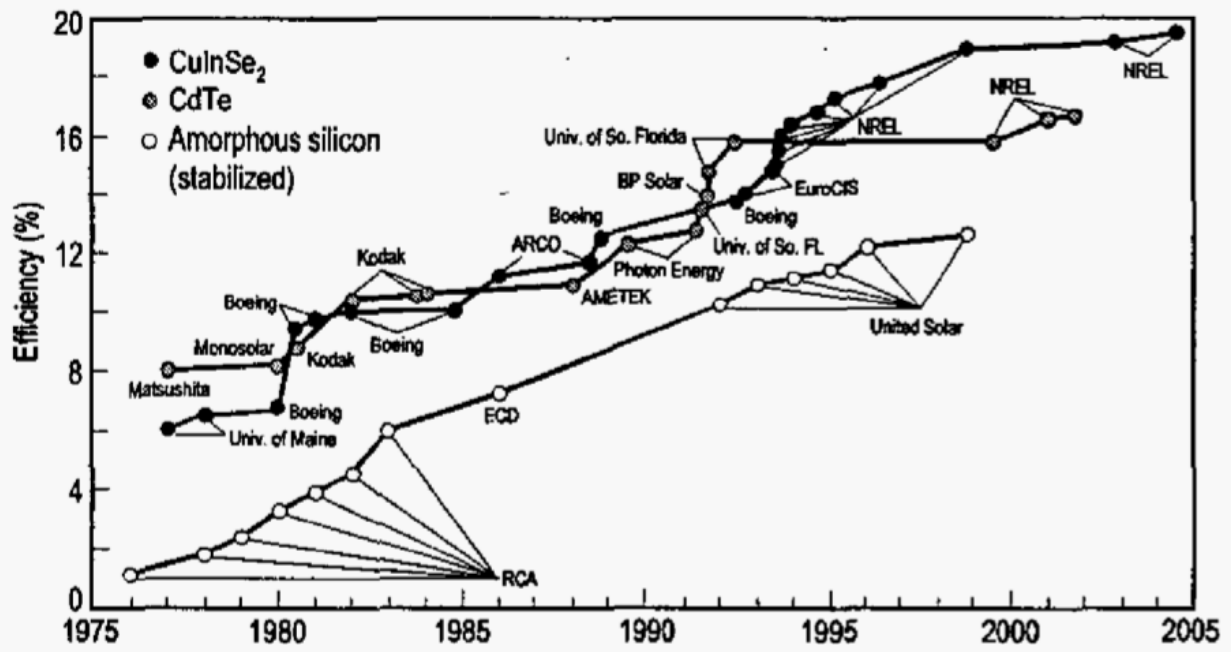


Figure 2-4. Chronological progress of a-Si, CdTe, and CIS thin film technologies from 1975 to 2005.

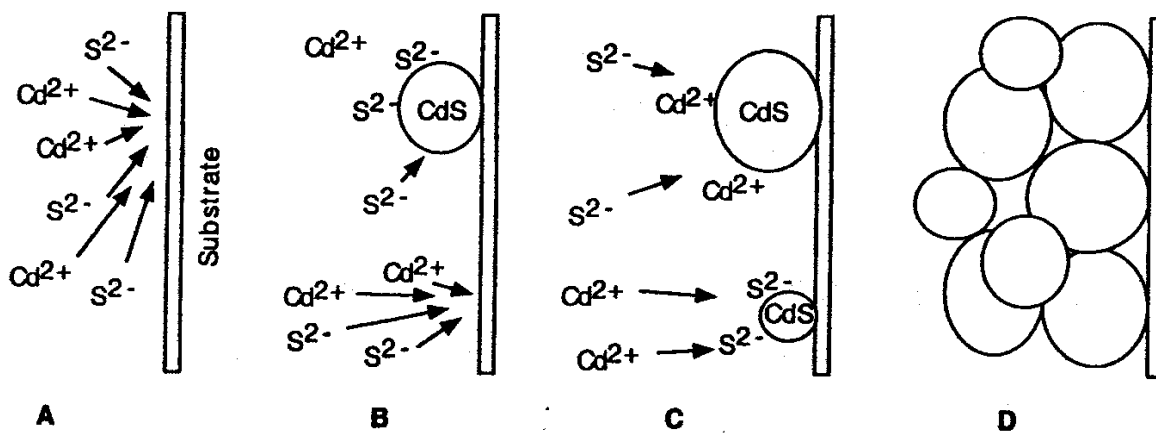


Figure 2-5. Ion-by-ion growth of CdS crystals.

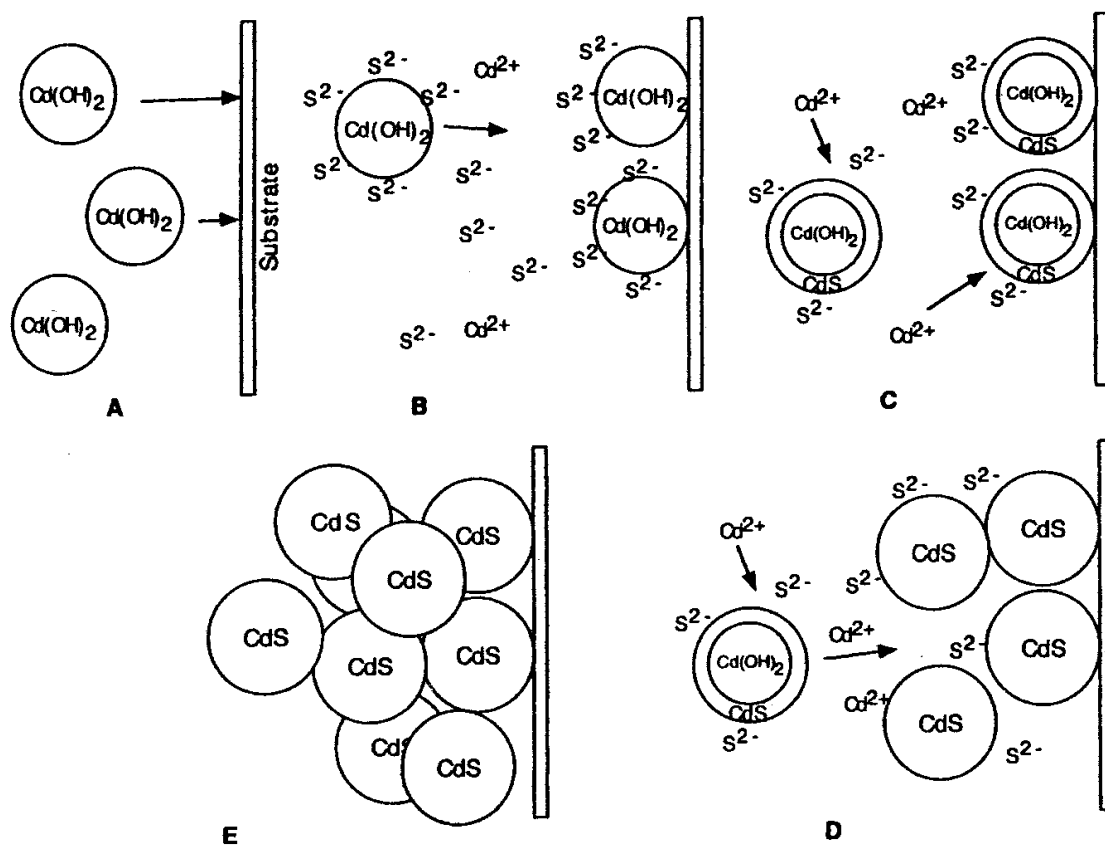


Figure 2-6. Growth of CdS crystals via the hydroxide cluster mechanism.

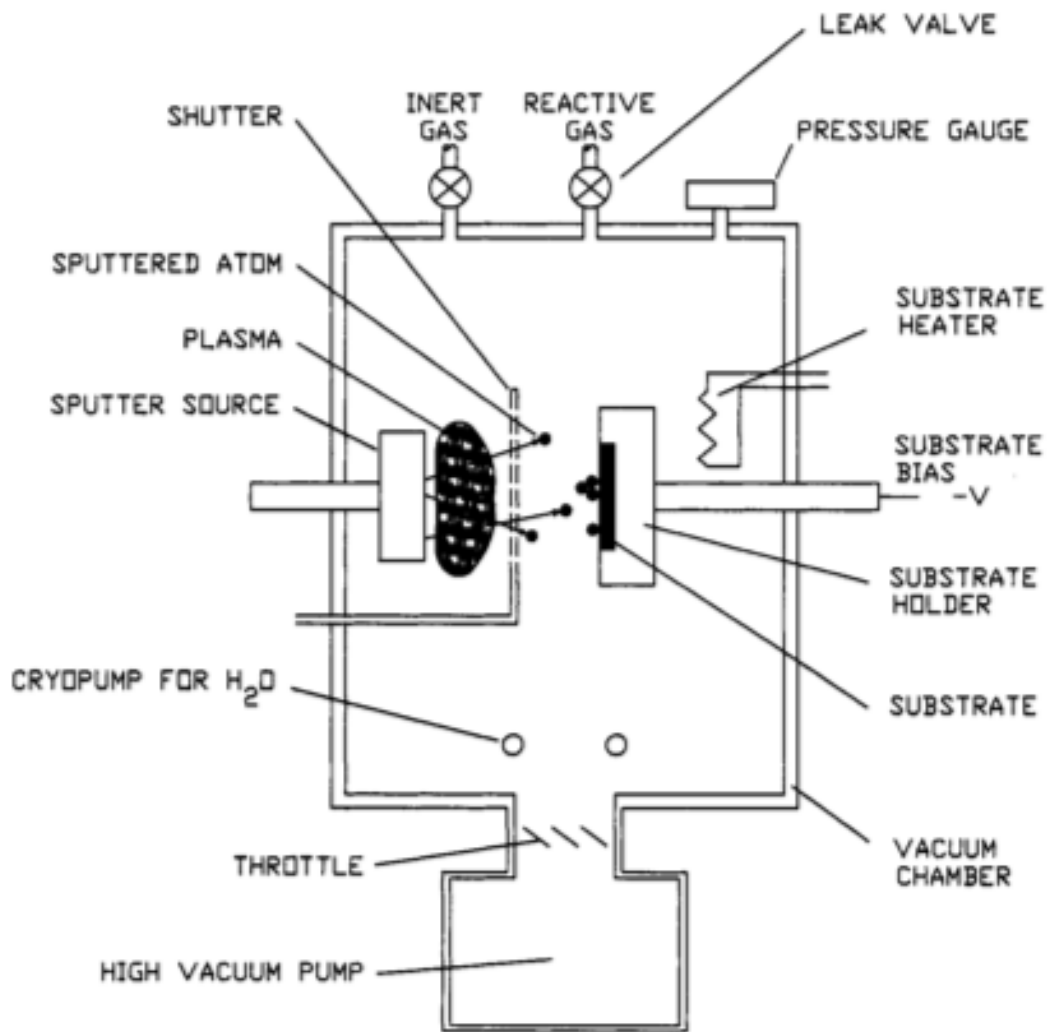


Figure 2-7. Typical sputter deposition chamber.

## CHAPTER 3 METHODS AND TECHNIQUES

This chapter serves to introduce and describe the methods and techniques used in this research. The process of device fabrication begins with proper substrate cleaning along with the deposition of the absorber layer. The procedure for deposition of the buffer layer via chemical bath deposition is presented which is followed by sputter deposition of the transparent conductive oxide layer. Completion of a photovoltaic device is achieved with the addition of top and bottom contacts. A number of thin film characterization techniques are also presented followed by the characterization of solar cell devices.

### **Substrate Cleaning Procedure**

A strict cleaning procedure is adopted to ensure that all substrates are thoroughly cleaned before their use in deposition or characterization. The first preparation step involves thoroughly washing each substrate with deionized water to remove any visible contaminants that may be present on the surface. Once each substrate has been individually rinsed they are placed in a Teflon substrate holder and transported to a hot deionized water bath held at a temperature of 80°C. The substrates remain in this first hot deionized water bath for at least 20 minutes before being removed. Each substrate is individually removed from the holder and mechanically cleaned with an Alconox detergent solution. The substrates are thoroughly rinsed with deionized water to ensure complete removal of the detergent solution. Once all substrates have been mechanically scrubbed and rinsed they are placed back in the substrate holder and delivered to an ultrasonic cleaner for a period of at least 20 minutes. Upon completion of the ultrasonic cleaning, the samples are again placed in an 80°C deionized water bath for at least 20 minutes. The substrates are then removed and placed in a three-step cascade of deionized water and

nitrogen for 30 minutes. Lastly, the substrates are removed from the cascade wash and dried thoroughly with nitrogen gas, and are stored in a clean and dry environment until use.

Once a substrate has been properly cleaned it is ready for use in film deposition, characterization, or any other processing step. All cleaned substrates are placed in vacuum-sealed bags in order to prevent contamination. Samples are removed from the sealed bags as needed for each processing step, thoroughly cleaned with nitrogen gas, and vacuum sealed immediately afterwards. Samples are sealed in 3.5 mm thick 8" by 10" mylar bags with a Mighty Mutt MPV-18 industrial vacuum sealer.

### **Absorber Layer Fabrication**

Absorber layers are often deposited by both vacuum and non-vacuum processes. Non-vacuum processes generally produce photovoltaic devices with lower efficiencies, however the cost of production is quite typically far less than the vacuum process alternative. Typically, vacuum processes, such as co-evaporation or sputtering, are employed in order to achieve optimal device performance. Currently, champion CIGS devices are fabricated using an absorber layer deposited through a co-evaporation process [45].

A high quality and well-controlled absorber layer is essential to the fabrication of high efficiency solar cells. At the University of Florida, CIGS layers are deposited using a PMEE, or plasma migration enhanced epitaxy, system [46]. The PMEE system is a variant of molecular beam epitaxy (MBE), which is a more traditional approach. With PMEE, the substrate is placed on a rotating platen and is sequentially passed under each source. Metal components such as copper, indium, and gallium are sequentially deposited during the exposure to each source. After the metal is deposited, the substrate then rotated into the selenium zone where it encounters a surplus of selenium vapor. Temperatures can reach up to 490°C and at these high temperatures the metals components and selenium vapor react and polycrystalline CIGS is formed. A typical

CIGS photovoltaic device fabricated at UF is pictured in Figure 3-1. During each rotation cycle the substrate is only exposed to each source once. Plasma migration enhanced epitaxy has a low throughput in compared to other PVD processes such as co-evaporation. It has been fairly well established that this process is not economically viable for large-scale photovoltaic production, however it is a useful techniques for exploring the single crystal regime of CIGS-based devices.

### **Buffer Layer Fabrication**

Deposition of a buffer layer is the next step in photovoltaic device fabrication. Deposition of this thin film is most typically achieved via a wet chemical process known as chemical bath deposition, or CBD. Chemical bath deposition is a technique of controlled precipitation of a compound from an aqueous solution and is extremely popular as it does not require a vacuum nor high temperatures, thus making it an extremely economical option for deposition of thin films.

Zinc cadmium sulfide, ZnCdS, is a typical buffer layer deposited at the University of Florida in the fabrication of photovoltaic devices. The incorporation of zinc allows for a reduction in the amount of the toxic cadmium component found in the commonly deposited CdS buffer layer. The recipe used for deposition of ZnCdS at UF is based off a patent by the Boeing company [47].

### **Chemical Bath Deposition Apparatus**

Buffer layers, namely zinc cadmium sulfide, are deposited via the chemical bath deposition apparatus shown in Figure 3-2. This photo shows both the hot water circulator and the chemical bath reaction vessel, which is pictured close-up in Figure 3-3. The CBD apparatus is capable of depositing up to four substrates simultaneously (each 2" x 2") at temperatures up to 90°C using deionized water as the hot bath liquid.

A schematic showing the details of the chemical bath deposition apparatus is portrayed in Figure 3-4. A Julabo F32-HC hot water circulator filled with water serves as the heating agent. The hot water bath is connected to a 1 L Chemglass jacketed beaker that serves as the CBD reaction vessel. The jacketed beaker is placed on a Fisher Scientific hotplate with magnetic stirring capabilities in conjunction with a magnetic mixer placed in the reaction vessel. The heating agent, in this case water, is circulated into the bottom inlet of the jacketed beaker and out of the top. A mercury thermometer is used to measure the temperature of the chemical bath inside the reaction vessel. Manual adjustments are then made to the Julabo hot water circulator control unit set point until the thermometer reveals that the bath has attained its target temperature. A Julabo Pt100 thermocouple sensor is capable of providing communication to the Julabo F32-HC control unit and can be used in place of the mercury thermometer. In this closed-loop setup, the control unit is able to automatically adjust its set point to provide and maintain the desired bath temperature. Entegris D11-0215 Teflon single-substrate dippers are secured to the reaction vessel cover to maintain a vertical position inside the reaction vessel during film growth.

### **Transparent Conductive Oxide Fabrication**

Following deposition of the buffer layer, a transparent conductive oxide layer is deposited, most often via sputtering. An intrinsic zinc oxide layer is first deposited followed by an aluminum-doped zinc oxide (AZO) layer. There are two characteristics of TCOs that have a significant impact on the performance of CIGS-based photovoltaic devices, optical transmission and electrical resistance. Both of these characteristics are impacted by TCO thickness in conflicting ways. Transmission determines the quantity of photons that are able to enter into the device and resistance determines the ability of generated current to flow through the device. Therefore, the thickness of the TCO layer must be adjusted in order to maintain good optical

transmission while achieving low sheet resistance. Decreasing the thickness of the TCO layer would help to improve transmission but would also increase resistance and result in substandard device performance.

### **Sputter Deposition System**

Transparent conductive oxides are deposited via sputter deposition, namely the Perkin-Elmer Model 4400 Production Sputtering System photographed in Figure 3-5. The Model 4400 System operates at room temperature and is capable of depositing a wide variety of materials onto substrates such as ceramics, glass, plastics, metals, and semiconductors, in thickness ranging from a few angstroms to hundreds of microns. Sputter etching can also be performed thereby reversing the process in order to remove material from the surface of the substrate.

The Perkin-Elmer Model 4400 Production Sputtering System consists of a RF impedance matching network, system control unit, target and substrate support assemblies inside a large vacuum chamber, and a load lock with a pallet transfer mechanism. A schematic of the sputtering system can be seen in Figure 3-6. The top of the system houses the impedance matching network. This network serves to match the impedance of the cathode/discharge/anode system to the 50  $\Omega$  impedance of the incoming RF power line. In this system a Randex 2 kW RF generator serves as the RF power source, at a frequency of 13.56 MHz. Without this impedance matching network the impedance mismatch can cause standing waves and heating of cables and certain power generator components as a result of reflected waves traveling back into coaxial cable connected to the power generator. Load and tune controls serve to match real and imaginary parts of the impedance which allows proper matching even under wide variations in deposition parameters.

Three sputter modes are available depending on where the RF power is applied. Sputter deposition can be achieved by grounding the substrate pallet and applying all the RF power to

the target, meaning only the target is bombarded by ions and subsequently sputtered. In the bias sputter mode RF power is again applied to the target, but a small amount of RF power is also applied to the substrate pallet. This results in substrates also being bombarded by ions, but to a far lesser degree than the target. Compared to RF sputtering with grounded substrates, bias sputtering typically yields higher quality depositions. Lastly, applying all RF power to the substrate pallet results in sputter etching, where substrate material is etched away by ion bombardment.

A target selector is used to connect the output of the matching circuitry to any of the three targets installed in the system. Brazing, soldering, or epoxy bonding can be used to bond target materials onto the cathode assembly. Eight-inch molybdenum, zinc, and aluminum oxide doped zinc oxide (2wt%) targets are currently installed in the system. Dark space shields are required for targets less than 8 inches in diameter in order to limit discharge to the target material only, protecting the backing plate from ion bombardment. Target to substrate distance has a large influence on the uniformity of deposited film thickness, and can be adjusted between 5 cm and 9 cm. Water is used for cooling of the targets and substrate pallet.

The substrate pallet has a diameter of 23.1", and can accommodate up to 30 three inch diameter substrates. In fixed mode the substrate pallet is held stationary and sputter deposition is limited to the exposed area of the substrate pallet. The rotary mode allows for the substrate pallet to be rotated according to user specified direction, angular velocity, and oscillatory motion. In this case a uniformity shaper can produce film uniformity within  $\pm 5\%$  resulting in highly identical results from deposition to deposition, assuming all other parameters are held constant.

Transfer of substrates into the main chamber is accomplished via a load lock that allows the sputtering chamber to remain isolated from the atmosphere during loading and unloading of

samples. Use of a load lock results in shorter pump-down times and eliminates the need for repeated cleaning of the targets after introduction of new samples, both of which lead to higher production rates. A transport mechanism carries the substrate pallet from the load lock to the anode, or substrate table, inside the sputtering chamber. An elevator mechanism is then responsible for raising the substrate table to its correct target to substance distance. The system features automatic or manual control of all load lock functions.

The Perkin-Elmer Model 4400 Sputtering System includes two pumps. A Leybold Trivac rotary vane pump (60 ft<sup>3</sup>/min) is used for chamber roughing, and the high vacuum pump is a CTI CryoTorr 8 cryopump, which is attached to the system via a throttle valve. The venetian blind style throttle is open during regular pumping and has a conductance greater than 1100 L/s. The valve is closed during sputtering reducing pumping speed thereby allowing the sputtering gas to fill the chamber. The throttle valve can be adjusted to provide the desired level of pumping. Mass flow controllers (0-100 sccm) are used to regulate the flow of sputtering gas into the system, namely Ar, O<sub>2</sub>, and an Ar /H<sub>2</sub> mix. Normal working pressures are in the range of 10 mTorr to 150 mTorr, which are easily altered by adjustment of the throttle valve and gas flow into the chamber.

Accurate system pressure is measured by combining several different types of pressure gauges. Three thermocouple gauges are employed, effective between 10 Torr to 10<sup>-3</sup> Torr, which operate via a thermocouple that measures the temperature of a heated wire that is cooled by surrounding gas. Two convectron gauges, a type of thermocouple gauge, are attached to the system, which are effective in measuring pressures between 10<sup>-3</sup> Torr and 1000 Torr. A conversion chart is required when measuring a mixed species gas environment, as convectron gauges are sensitive to the type of gas being measured. To combat this problem a MKS Baratron

capacitance manometer is used which measures the change in capacitance of a diaphragm as a result of flexure of the diaphragm caused by a change in pressure. Capacitance manometers are direct measurement gauges and therefore can accurately measure mixed species gas environments in the range of  $10^{-5}$  Torr to 1 Torr, depending on the thickness of the diaphragm.

In order to maintain low substrate temperatures an RF magnetron is used to take advantage of magnetically confined plasma sputtering. The magnetic field induced by the RF magnetron deflects secondary electrons produced in the sputtering process away from the substrates. This magnetic field is superimposed on the plasma, however is sufficiently low enough to only deflect secondary electrons but not strong enough to substantially effect the plasma, thereby resulting in low substrate temperature operation. Water is used to cool the RF magnetron assembly.

### **Photovoltaic Device Fabrication**

Photovoltaic device fabrication requires deposition of additional components such as the back contact, top contacts, and anti-reflective coatings. The back contact usually consists of molybdenum and is deposited on the substrate before the absorber layer. The anti-reflective coating applied is usually  $\text{MgF}_2$  and is deposited on top of the TCO, which is then followed by the evaporation of the top contact, usually a mix of nickel and aluminum.

#### **Back Contact**

A thin layer of molybdenum is deposited, most often by sputtering, on a bare substrate to serve as the back contact for a photovoltaic device. Molybdenum is used as it forms a good ohmic contact with CIGS and at the same time resists reaction with the CIGS film. The Mo back contact also remains stable in the highly corrosive selenium vapor to which it is exposed during absorber growth. For devices fabricated at UF molybdenum-coated soda lime glass (SLG) is provided by Shell Solar Industries (SSI).

## **Metallization and Anti-Reflective Coating**

A dual layer contact grid of nickel and aluminum is deposited onto the transparent conductive oxide, or AZO in the case of devices fabricated at UF, layer to complete device fabrication. Nickel serves as a diffusion barrier preventing aluminum oxide from entering the zinc oxide layer. The grid covers only a very small portion of the device, about 5%, to allow a sufficient amount of light to pass through the contact layer and into the device. While no anti-reflective coating is used in the work at the University of Florida, in an ideal situation, a  $\text{MgF}_2$  anti-reflective coating could be evaporated onto the device to reduce light reflection and permit maximum light entrance into the device.

## **Characterization Techniques**

To fully characterize the thin films under analysis, it becomes necessary to employ a range of modern measurement techniques to probe topics such as surface structure, surface morphology, surface region composition, crystal structure, and film thickness, among others. The following subsections present brief descriptions of techniques that are of particular relevance to this research.

### **Inductively Coupled Plasma**

Inductively Coupled Plasma (ICP) is an analytical technique used for the detection of trace metals in environmental samples. The primary goal of ICP is to cause elements to emit light of a characteristic wavelength which can then be measured. The technology for the ICP method was first employed in the early 1960's with the intention of improving crystal growing techniques.

ICP hardware is designed to generate a plasma, a gas in which atoms are present in an ionized state. The basic set up of an ICP consists of three concentric tubes, most often made of silica. These tubes, denoted outer loop, intermediate loop, and inner loop, collectively make up the torch of the ICP. The torch is situated within a water-cooled coil of a radio frequency (RF)

generator. As flowing gases are introduced into the torch, the RF field is activated and the gas in the coil region is made electrically conductive. This sequence of events forms the plasma.

In order to prevent possible short-circuiting as well as meltdown, the plasma must be insulated from the rest of the instrument. Insulation is achieved by the concurrent flow of gases through the system. Three gases flow through the system--the outer gas, intermediate gas, and inner or carrier gas. The outer gas is typically Argon or Nitrogen. The outer gas serves several purposes, including maintaining the plasma, stabilizing the position of the plasma, and thermally isolating the plasma from the outer tube. Argon is commonly used for both the intermediate gas and inner or carrier gas. The purpose of the carrier gas is to convey the sample to the plasma.

The ICP analysis technique requires that the elements that are to be analyzed be in solution. An aqueous solution is preferred over an organic solution, as the former requires special manipulation prior to injection into the ICP. Solid samples are also discouraged, as clogging of the instrumentation can occur. A nebulizer transforms the aqueous solution into an aerosol. The light emitted by the atoms of an element in the ICP must be converted to an electrical signal that can be measured. This is accomplished by resolving the light into its component radiation, by means of a diffraction grating, and then measuring the light intensity with a photomultiplier tube at the specific wavelength for each element line. The light emitted by the atoms or ions in the ICP is converted to electrical signals by the photomultiplier in the spectrometer. The intensity of the electron signal is compared to previous measured intensities of known concentration of the element, and a concentration is computed. Each element typically has several specific wavelengths in the spectrum that could be used for analysis. Thus, the selection of the best line for the analytical application in hand requires considerable experience with ICP wavelengths.

The advantages of using the ICP analysis include its ability to identify and quantify all elements, with the exception of Argon. Since many wavelengths of varied sensitivity are available for any one element, ICP is suitable for all concentrations from ultra-trace levels to major components. The detection limits are generally low for most elements with a typical range of 1 – 100 g/L. Probably the largest advantage of employing ICP for quantitative analysis is that multi-elemental analysis can be successfully accomplished, and the process is particularly rapid. A complete multi-element analysis can be completed in a period as short as 30 seconds, consuming only 0.5 mL of sample solution. Although in theory all elements except Argon can be determined via ICP, certain unstable elements require special facilities for handling the radioactive fume of the resulting plasma. Also, ICP has difficulty handling halogens where special optics for the transmission of the very short wavelengths of these elements become necessary.

### **Scanning Electron Microscopy**

Scanning electron microscopy (SEM) is possibly the most widely used thin film characterization instrument as a result of its reasonable cost and the wide range of information it is capable of providing. A scanning electron microscope allows one to ‘see’ the surface of a sample visually by providing a highly magnified image. The method used to create these images can greatly simplify the image, and care should be taken to consider the interpretation of SEM images. Magnification of sophisticated equipment can range from 10x to 300,000x, with resolution on the order of a few nanometers. Most SEMs are capable of accelerating voltages ranging from 1 keV to 50 keV, however most are operated around 25 keV.

Figure 3-7 portrays a schematic describing the operation of a scanning electron microscope [48]. A load-lock system is most often used to introduce the sample into the SEM, which is operated under high vacuum conditions. Electrons are emitted from a source, typically

a tungsten or LaB<sub>6</sub> filament, and focused by deflection coils into a fine probe that is rastered over the surface of the sample. A number of interactions take place as these electrons are scanned over and penetrate the surface of the sample, many of which result in the emission of photons or electrons from, or through, the surface. Detectors are used to collect the emissions, and the output is fed to a display device. The x and y inputs of the display device are rastered in sync with the rastering of the electron beam on the sample. The emission of each point on the sample is directly mapped to the corresponding point on the display device. Repeating this for all measured points on the sample results in an image being produced on the display device. Magnification is achieved by reducing the area of the raster pattern on the sample while keeping the display mapped to a fixed level. Secondary electron images, backscattered electron images, and elemental x-ray maps are the three main images types that a SEM is capable of producing.

### **Secondary electron imaging**

Secondary electron imaging is the most common imaging mode, and relies on detection of secondary electrons emitted from the sample. These are very low energy electrons, which originate from a subsurface depth no larger than several angstroms. A detector is used to capture these electrons and produce an output signal. This output signal serves to modulate the intensity of an external display device, which is rastered in sync with the rastering of the primary beam impinging upon the specimen. Images can be magnified by increasing the ratio of scan lengths on the display device to that on the specimen. Sophisticated SEM systems are capable of imaging samples with a resolution on the order of a few nanometers.

### **Backscattered electron imaging**

Backscattered electron imaging relies on detection of backscattered electrons emitted from the sample. These are high energy electrons, which possess nearly the same energy as impinging electrons, that are elastically scattered by the sample. The atomic number of the sample material

determines the level of backscattering, as backscattering of electrons increases with increasing atomic number. Although specific elemental identification is not possible, regions of the sample that exhibit wide differences in atomic number can be easily contrasted.

### **Energy dispersive spectroscopy**

X-rays can often be emitted as a result of inelastic collisions of primary beam electrons with the specimen. Continuum and characteristic x-rays are the two types of x-rays that can be emitted during such a collision. Characteristic x-rays are of greatest importance, however continuum x-rays, analogous to noise, can play a large role in rendering energy dispersive spectroscopy (EDS) spectrum analysis difficult. Characteristic x-rays have unique energies that are related to electronic transitions in every atom. Analysis of these energies is achieved with the use of an energy dispersive spectrometer, which is a detector that is capable of discriminating between x-ray energies. This discrimination allows atoms in the specimen to be identified and, via ZAF (atomic number, absorption, and fluorescence) correction factors, qualified quantitatively.

### **X-Ray Diffraction**

X-ray Diffraction (XRD) is a popular method that is capable of identifying and measuring the structural properties of crystalline phases that are present in a given sample. Grain size, phase composition, epitaxy, strain, preferred orientation, and defect structure of crystalline phases can all be accurately identified. Thickness determination of thin films and multi-layers can also be achieved with XRD. Thin film analysis requires very little sample preparation, does not contact the sample, and is non-destructive, which makes it an ideal in situ characterization technique. Most all materials can be successfully analyzed, however the measurement sensitivity depends on the material in question. Elements with a high atomic number provide strong diffraction intensities and therefore provide increased XRD sensitivity. Sophisticated equipment

can easily measure thin films less than 50 Å and can measure film structure as a function of depth.

X-Ray Diffraction (XRD) is becoming an extremely popular method for determining crystalline phases present in solid samples as a result of the technique's versatile and non-destructive nature, as well as the extremely simple sample preparation requirements. Unknown sample identification is achieved by comparing x-ray diffraction patterns against an international database of known phases.

In XRD, a collimated beam of x-rays, with wavelength  $\lambda = 0.5\text{-}2 \text{ \AA}$ , is incident on a specimen and is diffracted by the crystalline phases in the specimen according to Bragg's law

$$\lambda = 2d \sin \theta, \quad (3-1)$$

where  $d$  is the spacing between atomic planes in the crystalline phase. The intensity of the diffracted x-rays is measured as a function of the diffraction angle  $2\theta$ , and the specimen's orientation. This diffraction pattern is used to identify the specimen's crystalline phase and to measure its structural properties, including strain (which is measured with great accuracy), epitaxy, and the size and orientation of crystallites (small crystalline regions). XRD can also determine concentration profiles, film thicknesses, defects, and atomic arrangements in amorphous materials and multilayers. To collect this structural and physical information from thin films, XRD instruments and techniques are designed to maximize the diffracted x-ray intensities, since the diffracting power of thin films is small.

The full width at half maximum values, easily obtained from high resolution XRD scans, can be used to calculate grain size information. The average grain size  $L$  can be estimated using the Scherrer formula [49],

$$L = \frac{K\lambda}{\beta \cos \theta} \quad (3-2)$$

where  $\beta$  is the full width at half maximum,  $\lambda$  is the x-ray wavelength, and  $\theta$  is the diffraction angle. The shape factor  $K$  is a constant and its value is often taken as 1.0 [50].

### **Profilometry**

Profilers are widely used instruments and routinely used as an alternative to in-situ film thickness measurements. Mechanical profilers operate by recording height displacements as a stylus runs over a surface. By recording the vertical displacement as a function of sample positioning, a profile of the surface can be created. The biggest drawback of surface profilometry is the need for physical interaction with the sample surface, since the stylus must come in contact with the surface in order to perform the measurement. Non-contact alternatives focus around reflectometric and time-of-flight measurements of light passing through the film.

In order to perform thickness measurements on thin films with a surface profiler, a portion of bare substrate is required. Two methods exist to remove a portion of the film. The first method is a type of ‘lift-off’ etching where a portion of the substrate is masked before film deposition. After deposition this mask can be removed either chemically or mechanically, resulting in ‘lift-off’ of the film and exposure of the substrate. The second method involves using a mask to protect a portion of the deposited film rather than remove it. Once the mask is applied to the film, the substrate is placed in an etching solution, resulting in any part of the film not covered by the mask being etched away. A different chemical solution can then be used to remove the mask material from the remaining film. Care must be taken with this method as excessive etching times can result in horizontal etching of the protected film under the mask, which can alter surface profiler measurements.

For this work, a Veeco Dektak 150 Surface Profiler is used for measuring thin film thickness in this work. The Dektak 150 is capable of accommodating samples up to four inches

thick, and can perform long scan of up to 55 mm. The profiler has a vertical measurement range of 512  $\mu\text{m}$  and can perform precise step height measurements of thin films down to 100  $\text{\AA}$  with a repeatability of 6  $\text{\AA}$ . The system also features an X-Y auto stage that can be programmed to provide automated sample mapping. A low force stylus (sensitivity of 0.03 mg) enables non-destructive characterization of delicate surfaces.

### **Ellipsometry**

The technique of ellipsometry, also known as polarimetry and polarization, is over a century old and is used to obtain the thickness and optical constants of films. The method consists of measuring and interpreting the change of polarization state that occurs when a polarized light beam is reflected at non-normal incidence from a film surface. Figure 3-8 shows a schematic depicting a common experimental arrangement for ellipsometry measurements [51]. The light source is first made monochromatic, collimated, and then linearly polarized. Upon passing through the compensator, the light is circularly polarized and then impinges on the specimen surface. After reflection, the light is transmitted through a second polarizer that serves as the analyzer. Finally, the light intensity is measured quantitatively by a photomultiplier detector. The polarizer and analyzer are rotated until light extinction occurs. The extinction readings enable the phase difference ( $\Delta_e$ ) and amplitude ratio ( $\tan\psi$ ) of the two components of reflected light to be determined. From these, either the film thickness or the index of refraction can be obtained [52].

### **Ultraviolet-Visible Spectroscopy**

Ultraviolet-visible spectroscopy is most often used for measuring the transmittance and absorbance of liquid and solid samples. A simple schematic of a UV/vis spectrophotometer can be seen in Figure 3-9. A spectrophotometer measures transmission with a UV/vis source, most

often tungsten and deuterium, which produces light that is then selectively separated by a monochromator. A detector collects the diffracted light that passes through the sample and the signal is passed on to software which then compares the intensity of the transmitted light,  $I$ , to the intensity of the incident light,  $I_o$ . The transmittance of the sample is given by

$$T = \frac{I}{I_o}, \quad (3-3)$$

where the transmittance is expressed as a percentage. Once the transmittance of the sample is known, the absorbance,  $A$ , can be calculated as

$$A = \log_{10}\left(\frac{I_o}{I}\right). \quad (3-4)$$

The relationship of the absorbance coefficient,  $\alpha$ , to the intensity of the transmitted light  $I$  can be derived according to the Beer-Lambert equation, and is given by

$$I = I_o e^{-\alpha t} \quad (3-5)$$

where  $t$  is the film thickness of the sample. When the thickness of the film is known, the transmittance can be used to calculate the absorption coefficient as

$$\alpha = \frac{\ln\left(\frac{1}{T}\right)}{t}. \quad (3-6)$$

Once the absorption coefficient is known, the optical band gap of the film can be calculated by the Tauc equation,

$$(\alpha h\nu)^n = B(h\nu - E_g) \quad (3-7)$$

where  $B$  is a constant, and  $n = 0.5$  for an indirect transition or  $n = 2$  for a direct transition semiconductor [53, 54]. The optical band gap energy can then be obtained from a plot of  $(\alpha h\nu)^n$

vs.  $(h\nu)$ , where a straight line is observed over the absorption onset region. This fitted line can be extrapolated to  $(\alpha h\nu)^n = 0$  to obtain the optical band gap energy,  $E_g$ .

A Perkin-Elmer Lambda 800 UV/Vis spectrophotometer is used to collect optical transmission, absorbance, and band gap data. The system uses twin beams, tungsten and deuterium, to collect transmittance spectra from 200 nm to 900 nm. The preparation of a reference sample is suggested to provide adequate background correction of measured spectra.

### **X-Ray Photoelectron Spectroscopy**

X-ray photoelectron spectroscopy (XPS) is a surface sensitive technique that is capable of detecting binding energies of atoms in different chemical states. XPS is one of the most broadly used surface analysis techniques as a result of its surface sensitivity and its quantitative and chemical state analysis capabilities. Detection of all elements is possible with a sensitivity variation across the periodic table of approximately 30, except for hydrogen and helium. Gaseous, liquid, and solid samples can be measured, although most systems are specifically tailored for solid samples. XPS is most capable of measuring the surface of samples (top two atomic layers) but can also measure from 15 to 20 layers deep, with a resolution of up to 70  $\mu\text{m}$ . It is generally considered a non-destructive technique and a variety of samples can be accommodated, including biological, organic, and polymeric materials.

XPS is based on the Einstein photoelectric law. High energy photons have the ability to ionize atoms and eject free electrons. The kinetic energy of the electron depends on the energy of the photon  $h\nu$  which can be expressed by the Einstein photoelectric law

$$KE = h\nu - BE \quad (3-8)$$

where KE is the kinetic energy of the photoelectron and BE is the binding energy of the electron to the atom. The kinetic energy can therefore be measured to determine the binding energy,

since the energy of the photon ( $h\nu$ ) is known. In a neutral atom, the number of electrons equals the number of protons. These electrons are arranged in pairs of two in orbitals around the nucleus, bound by electrostatic attraction. Each orbital has a discrete energy level, which varies for all elements since the electrostatic attraction will vary with differing nuclei. The binding energy of an electron can therefore be determined by the amount of energy required to remove it from the atom. Experimental determination of the binding energy approximately relates to a discrete energy value, which is specific to a particular atom, thereby identifying that atom [48].

X-ray photoelectron spectroscopy, Auger electron spectroscopy, and secondary ion mass spectrometry are all very widely used surface analysis techniques. XPS is similar to AES in terms of elemental analysis capability and absolute sensitivity. The main advantages of XPS are its more developed chemical state analysis capability, somewhat more accurate elemental analysis, and far fewer problems with induced sample damage and charging effects for insulators [48].

### **Secondary Ion Mass Spectrometry**

Secondary ion mass spectrometry (SIMS) is an analytical technique that is capable of trace-level contaminant detection and can provide quantitative measurements of major and minor components. The technique is destructive, as material must be removed from the sample in order to perform the measurement. Material is sputtered from the sample in the form of neutral and ionized atoms and molecules by a focused ion beam. This sputtered material is accelerated into a mass spectrometer, and is then separated according to mass-to-charge ratios. Depth profiling is the most common application of SIMS, where elemental impurity is measured as a function of depth. Quantitative measurements are possible but require the use of standards.

SIMS is an extremely sensitive analytical technique, capable of detection limits in the parts-per-million to parts-per-billion range. Depth resolution is generally around 2 nm with a lateral resolution between 50 nm and 2  $\mu\text{m}$ . SIMS can accurately measure any elemental impurity, even elemental isotopes, with a detection limit between  $10^{12}$  and  $10^{16}$  atom/cm<sup>3</sup> for most impurities.

Secondary ion mass spectrometry is one of the dominant surface analysis techniques along with x-ray photoelectron spectroscopy and Auger electron spectroscopy. Although SIMS has a lower spatial resolution and speed compared with the other two techniques, neither can match the superior trace analysis capabilities of SIMS. SIMS also has the ability to detect hydrogen and helium, which neither AES nor XPS can detect.

### **Auger Electron Spectroscopy**

Auger electron spectroscopy (AES) is a versatile technique that is used to identify elemental composition and chemical bonding of atoms in the surface region of thin films. It is often combined with ion beam sputtering to provide composition and chemistry analysis as a function of sample depth. AES measures the energy distribution of secondary electrons, notably the Auger electron component, that are released as a result of an electron beam probing the sample surface. J.J. Lander was the first to report the detection of Auger electrons in the secondary electron energy spectra [55].

The technique is surface sensitive and exhibits a sampling depth between 10  $\text{\AA}$  and 100  $\text{\AA}$ , depending on the energy of the Auger electrons measured. Generally, lateral spatial resolution is as low as 300  $\text{\AA}$  and depth resolution as low as 20  $\text{\AA}$ , depending on the electron and ion guns used, respectively. Detectability under good conditions is approximately 100 ppm for most

elements. Unfortunately, the electron beam probe can be destructive to some samples in addition to the ion beam damage that takes place during depth profiling measurements.

The basic Auger process involves the production of an atomic inner shell vacancy, most often by electron bombardment, and the decay of the atom from this excited state by an electronic rearrangement and emission of an energetic electron rather than by emission of electromagnetic radiation. There are four basic contributions responsible for producing Auger electrons found in the energy distribution resulting from the bombardment of a surface with an electron beam. These contributions are the creation of inner shell vacancies in atoms of the sample, the emission of electrons as a result of Auger processes resulting from these inner shell vacancies, the transport of those electrons out of the sample, and the detection and measurement of the energy distribution of the electrons coming from the sample. Auger electrons are generated in transitions back to the ground state of atoms with inner shell vacancies, no matter what process produces the inner shell vacancy. As a result, Auger peaks are observed in energy spectra generated by electron excitation, x-ray excitation, ion exchange, and certain nuclear reactions [48].

There are three main modes of AES analysis. Point analysis mode is the simplest and most often used mode, in which the primary electron beam is positioned in a particular location and an Auger survey spectrum is collected. Another common mode is the depth profiling mode, which is identical to point analysis mode with the addition of an ion beam directed at the sample. The ion beam is used to sputter material off the surface of the sample so that the analysis can measure composition variation as a function of depth. In depth profiling mode, Auger data can be acquired either as a survey spectrum or can be gathered in a narrow scan window in order for detection of a specific element. The final mode of AES analysis, mapping mode, operates with

the goal of specific element detection. In mapping mode, the Auger peak of a specific element is monitored while the electron beam is scanned over the sample area. This results in a two-dimensional horizontal spatial distribution of a specific element, compared to the vertical distribution produced by the depth profiling mode. A three-dimensional spatial distribution of any element can be created by combining the mapping and depth profiling modes.

Auger electron spectroscopy, x-ray photoelectron spectroscopy, and secondary ion mass spectrometry are a very common set of techniques used in thin film analysis and characterization. They are capable of producing similar results, however each has its own strengths and weaknesses. The main advantage of AES is its superior spatial and depth resolution, along with absolute sensitivity to many important elements.

#### **Four-Point Probe**

The four-point probe technique was originally developed to measure the earth's resistivity [56], and is currently one of the most commonly used methods for measuring the resistivity of semiconductor materials [57]. A schematic of the four-point probe configuration is seen in Figure 3-10 and shows four finite metal tips with uniform spacing  $s$ . The outer two metal tips serve to introduce current  $I$  into the sample with the resulting electric potential  $V$  being measured by the inner two tips, or electrodes. The use of a four-probe setup eliminates the appearance of contact resistance in the resistivity measurement since separate electrodes are used for current supply and voltage detection compared to a two-probe system [58, 59]. As a result, the four-point probe technique is much preferred for its ease of data interpretation [60].

The resistivity of bulk and thin film samples can be measured via the four-point probe technique, however a different expression is used in each case. In the case of a bulk sample, where the sample thickness  $t$  is generally much larger than the probe spacing  $s$ , the expression for bulk resistivity is given as

$$\rho = 2\pi s \left( \frac{V}{I} \right), \quad (3-9)$$

assuming equal probe spacing. In the case of a thin film, the film thickness  $t$  is usually much smaller than the probe spacing  $s$ , in which case the sheet resistivity is given as

$$R_s = k \left( \frac{V}{I} \right) = 4.53 \left( \frac{V}{I} \right) \quad (3-10)$$

where  $k = 4.53$  is the geometric factor in the case of a semi-infinite thin film [61]. Given the film thickness  $t$ , the resistivity  $\rho$  can be calculated by

$$\rho = R_s t = 4.53 \left( \frac{V}{I} \right) t. \quad (3-11)$$

The Alessi four-point probe system features 0.05" spaced tungsten-carbide probe tips, which are 0.002" in diameter. Currents of 1  $\mu$ A to 100 mA are supplied by a Crytronics Model 120 current source. The voltage resulting across the inner probes is measured by a Keithley Model 181 Nanovoltmeter which is capable of 10 nV sensitivity.

### **Photovoltaic Device Characterization Techniques**

Current-voltage (I-V) characterization is an important part of analyzing photovoltaic device performance. A solar cell's *I-V* characteristics are directly related to a device's maximum power conversion efficiency. The standard Air Mass 1.5 Global Spectrum (AM1.5G), which is normalized at 1000 W/m<sup>2</sup>, is used for *I-V* measurement of devices. In addition, quantum efficiency (QE) measurements show a device's ability to adsorb radiation at specific incoming wavelengths.

#### **Current-Voltage**

Current-voltage measurements are used to predict the performance of a photovoltaic device. An *I-V* curve can be generated by measuring the current produced by varying load

resistance upon illumination of a solar cell device, most often under AM1.5G conditions. A typical  $I$ - $V$  curve is shown in Figure 3-11, where voltage is plotted on the horizontal axis and current on the vertical axis. The maximum voltage, or open-circuit voltage  $V_{oc}$ , exists when the current across the cell is zero, under infinite load resistance. The maximum current, or short-circuit current  $I_{sc}$ , exists when the voltage across the cell is zero, under zero load resistance. Photovoltaic devices cannot be operated at either the open-circuit voltage nor the short-circuit current, as no power would be produced since no current or voltage exist at the two points, respectively. The maximum power  $P_m$  the cell is capable of generating is given by

$$P_m = I_m V_m \quad (3-12)$$

where  $I_m$  and  $V_m$  are the values that maximize the maximum power as portrayed in Figure 3-x.

The degree to which the maximum power ‘fills’ the  $I$ - $V$  curve is given by the fill factor parameter which describes the degree to which the current and voltage at maximum power ( $I_m$  and  $V_m$ ) match  $I_{sc}$  and  $V_{oc}$ , respectively. The fill factor is given as

$$FF = \frac{P_m}{I_{sc} V_{oc}} = \frac{I_m V_m}{I_{sc} V_{oc}} \quad (3-13)$$

and is generally given as a percentage. The conversion efficiency  $\eta$  of a photovoltaic device describes its ability to convert incident photon energy,  $P_{in}$ , into electrical energy, and is calculated as

$$\eta = \frac{P_m}{P_{in}} = \frac{I_m V_m}{P_{in}} = \frac{I_{sc} V_{oc} FF}{P_{in}} \quad (3-14)$$

where  $\eta$  is the percentage of incident light converted to electricity.

The conversion efficiency of a solar cell is affected by a number of factors that hamper the conversion of incident photon energy to electricity. The band gap of a photovoltaic device refers to the minimum energy required to free electrons, and differs depending on the absorber material

used. The reason that photovoltaic devices are not very efficient is that they are unable to convert all wavelengths of incoming radiation. Photons with energies below the band gap do not possess the required energy and therefore only generate heat in the device. Likewise, photon energy above the band gap is also wasted and ends up being emitted as heat or light.

Another factor affecting solar cell conversion efficiency is recombination, where charge carriers recombine before contributing to the cell's current. Combination of photon-generated electrons and holes is termed direct recombination whereas indirect recombination occurs as a result of impurities or defects in the crystal structure. Temperature can also have a negative affect on devices as conversion efficiency tends to decrease with increasing temperatures.

Reflection of light away from a photovoltaic device's surface is another factor that negatively affected conversion efficiency. The two most common methods for reducing the reflection of incident photons are the application of antireflective coatings and surface texturing. Single or multiple antireflective layers are deposited in order to minimize reflection at different wavelengths. Perhaps the most common antireflective coating applied to CIGS-based solar cells is  $\text{MgF}_2$  [62, 36, 63-66]. Adding texture to the surface of a device increases the probability that incident light will be reflected and strike the surface again, thereby increasing the possibility of absorption.

### **Current-Voltage Measurement**

The *I-V* measurement system employs a tungsten-halogen lamp to produce incident photon energy, which compares well with the energy spectrum of AM1.5G radiation. A reference cell is used in order to calibrate the intensity of the tungsten-halogen lamp, which is adjusted by altering the distance between the lamp and the device being characterized. This distance is modified so that the measured short-circuit current matches the known value of the reference cell used in the calibration. The *I-V* measurement system is calibrated using reference data from a

CIGS solar cell obtained from the National Renewable Energy Laboratory (NREL). This CIGS device, S2117-A2, was fabricated on August 22, 2003, and contains seven cells, each with an area of  $0.430 \text{ cm}^2$ . The reference data obtained from NREL for each cell of the S2117-A2 device is listed in Table 3-1. For example, under the AM1.5G radiation spectrum used by NREL, cell 4 of the device exhibits a short-circuit current  $J_{sc} = -33.43 \text{ mA/cm}^2$ , an open-circuit voltage  $V_{oc} = 0.653 \text{ V}$ , a fill factor  $FF = 74.67 \%$ , and a conversion efficiency  $\eta = 16.291 \%$ . The  $I$ - $V$  measurement system is controlled via a personal computer and data is collected and analyzed using a custom LabVIEW software package [67].

As mentioned, increased device temperature tends to have a negative effective on overall device performance and conversion efficiency. An increase in operating temperature typically results in a decrease in the open-circuit voltage of CIGS devices. To ensure optimal performance, a cooling system is employed to control device temperatures during  $I$ - $V$  measurement. Cooling water circulates through the measurement assembly during measurement and a controller adjusts the flow rate to maintain an operating temperature of  $25 \text{ }^\circ\text{C} \pm 1 \text{ }^\circ\text{C}$ .

### **Quantum Efficiency**

The quantum efficiency (QE) of a solar cell relates the number of charge carriers collected by the device to the number of photons incident upon the device. The QE of a solar cell is given as a function of radiation wavelength, and therefore relates the response of a device to various wavelengths of the incident spectrum. Quantum efficiency exhibits an upper limit of one for the case where all photons of a distinct wavelength are absorbed and the corresponding minority carriers are collected. An incoming photon with energy less than the band gap will not be absorbed, resulting in a QE of zero. In the ideal case, quantum efficiency would be constant for all wavelengths of incoming radiation, resulting in a square shape. Recombination is considered

the main cause of reduced QE. High energy photons are generally absorbed closer to the front surface of devices, where recombination negatively affects the 'blue' portion of the QE spectrum. On the other hand, the 'green' portion of the QE spectrum is negatively affected by the recombination of carriers produced by the absorption of low energy photons in the bulk of devices.

The quantum efficiency of a photovoltaic device can be calculated under two conditions. The first condition includes losses in incident radiation that occur as a result of reflection and transmission through the device. This is generally referred to as the external QE, which takes into account all external losses of radiation. The second condition excludes these losses and focuses solely on light that has not been reflected or transmitted through the device, and is termed internal QE. External QE curves can generally be converted to internal QE curves by correcting for the reflection and transmission of the device.

Table 3-1. Reference data for NREL device S2117-A2.

Cell	Area (cm <sup>2</sup> )	$V_{oc}$ (V)	$J_{sc}$ (mA/cm <sup>2</sup> )	$I_{sc}$ (mA)	$FF$ (%)	Eff (%)	$V_{mp}$ (V)	$I_{mp}$ (mA)	$P_{max}$ (mW)
1	0.430	0.645	-31.83	-13.687	76.66	15.737	0.538	-29.26	15.737
2	0.430	0.649	-32.43	-13.945	75.30	15.858	0.532	-29.79	15.858
3	0.430	0.653	-30.11	-12.947	74.92	14.719	0.534	-27.54	14.719
4	0.430	0.653	-33.43	-14.374	74.67	16.291	0.532	-30.61	16.291
5	0.430	0.655	-33.59	-14.443	74.85	16.458	0.534	-30.80	16.458
6	0.430	0.654	-31.45	-13.524	74.88	15.400	0.532	-28.93	15.400
7	0.430	0.644	-32.97	-14.177	74.27	15.775	0.524	-30.08	15.775

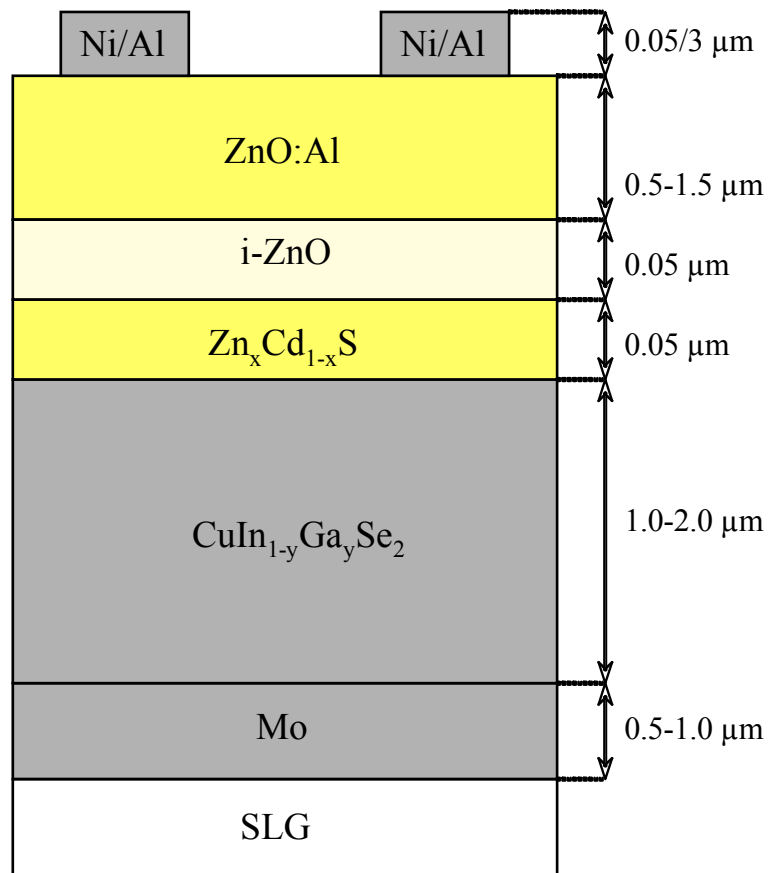


Figure 3-1. Structure of a typical CIGS/ZnCdS device fabricated at UF.

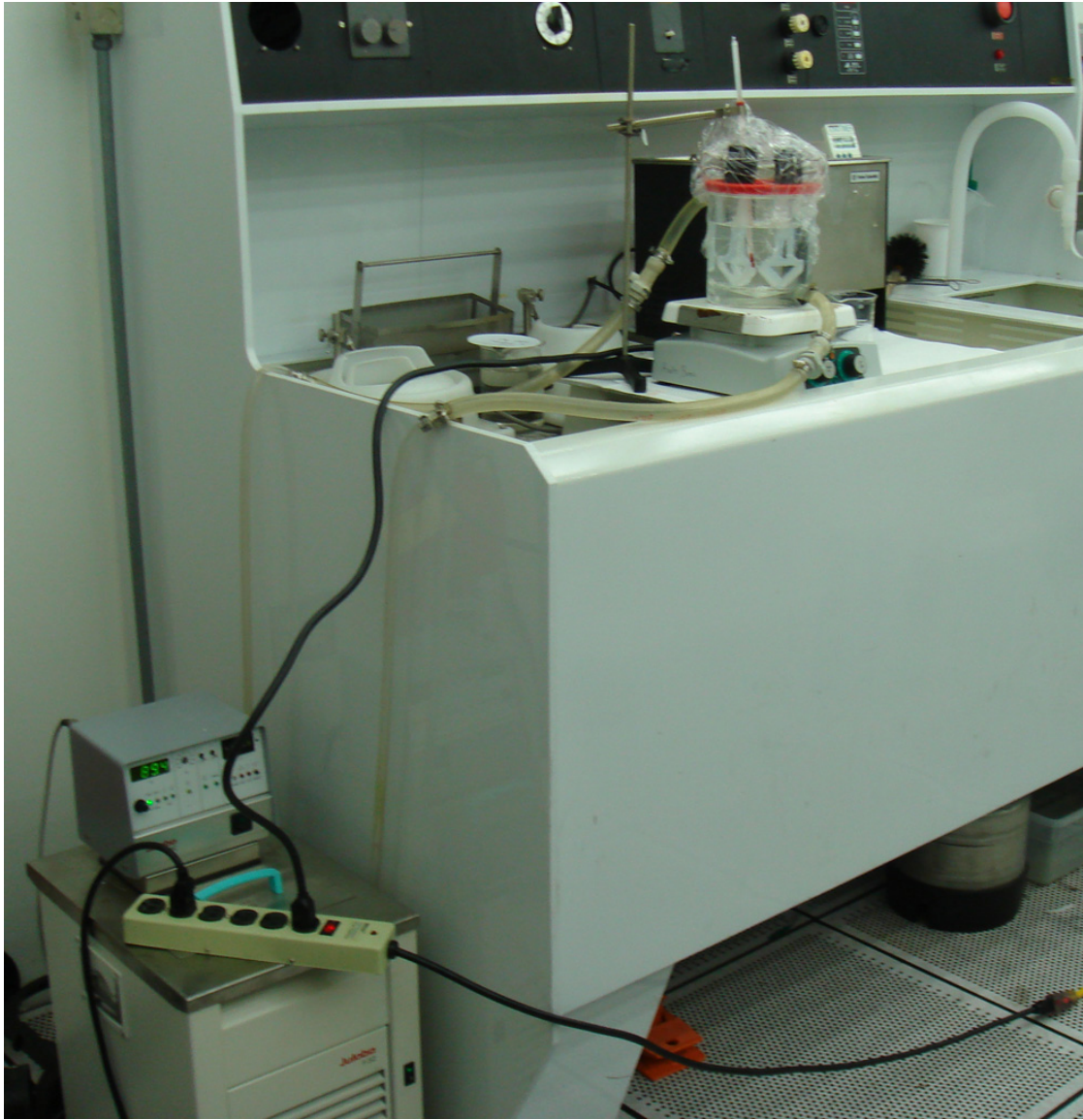


Figure 3-2. Chemical bath deposition apparatus.



Figure 3-3. Chemical bath deposition reaction vessel.

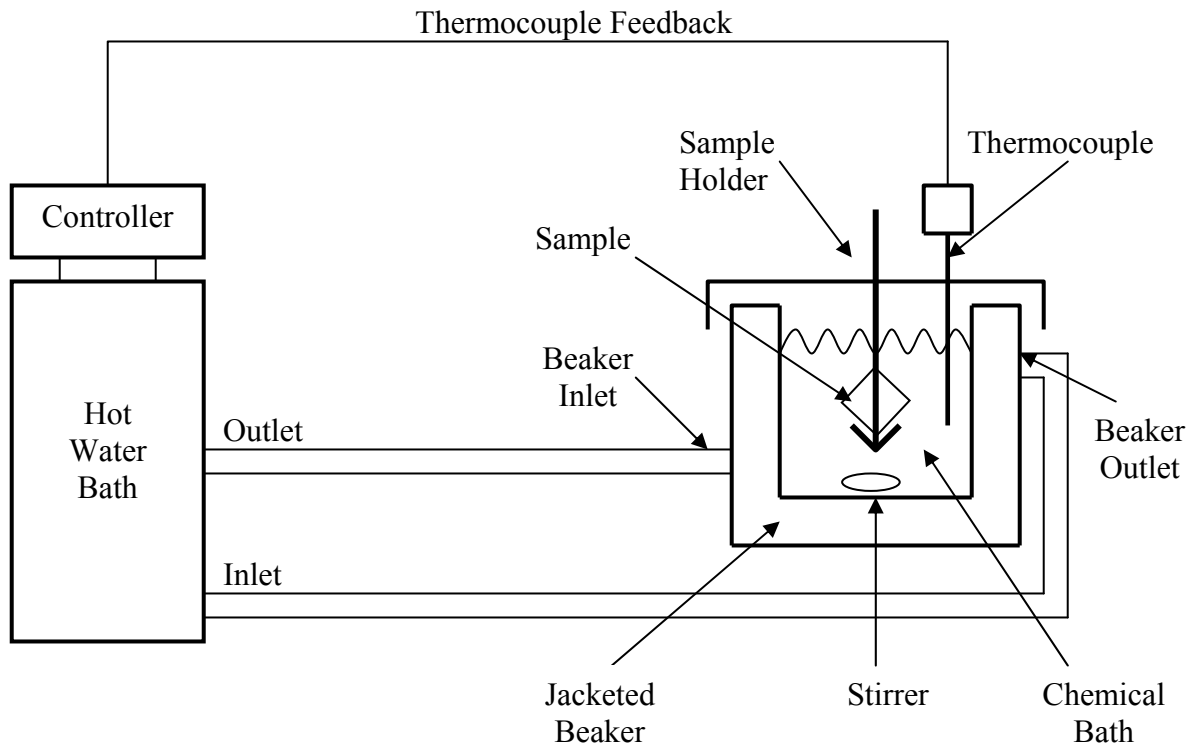


Figure 3-4. Chemical bath deposition apparatus and reaction vessel schematic.



Figure 3-5. Perkin-Elmer Model 4400 Production Sputtering System.

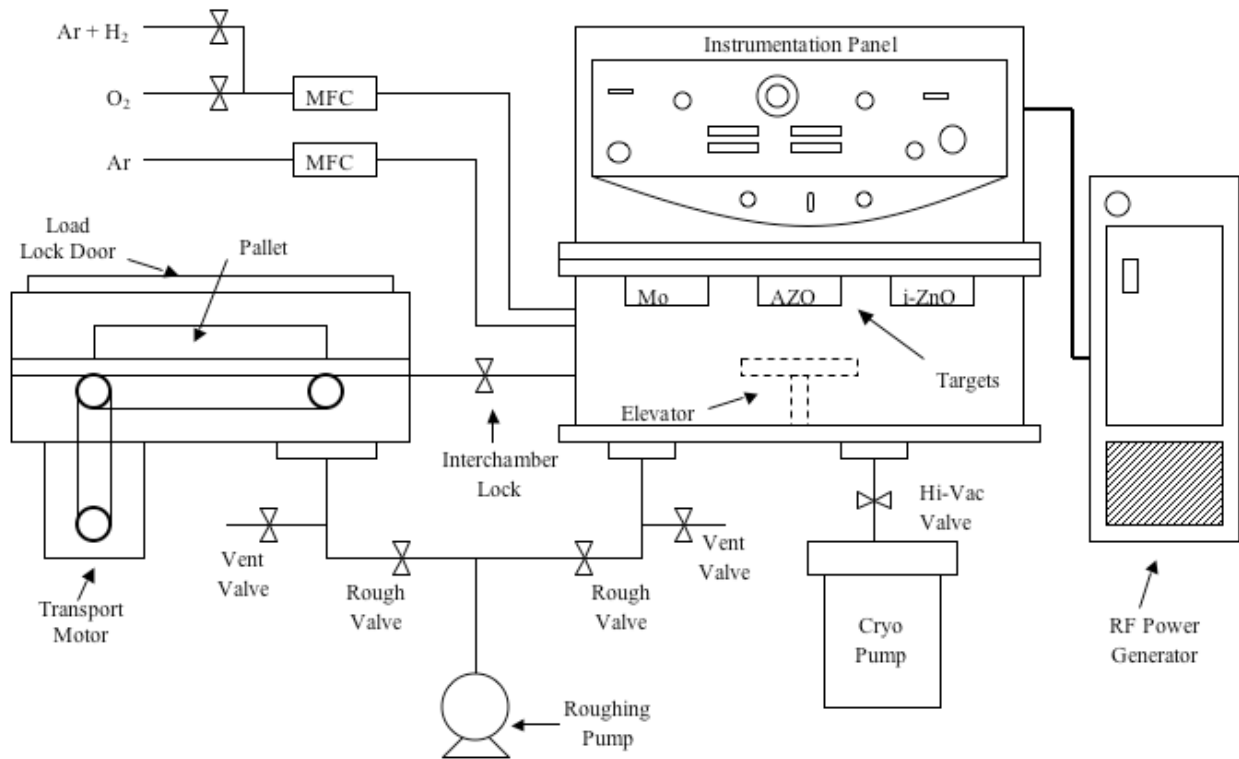


Figure 3-6. Perkin-Elmer Model 4400 Production Sputtering System schematic drawing.

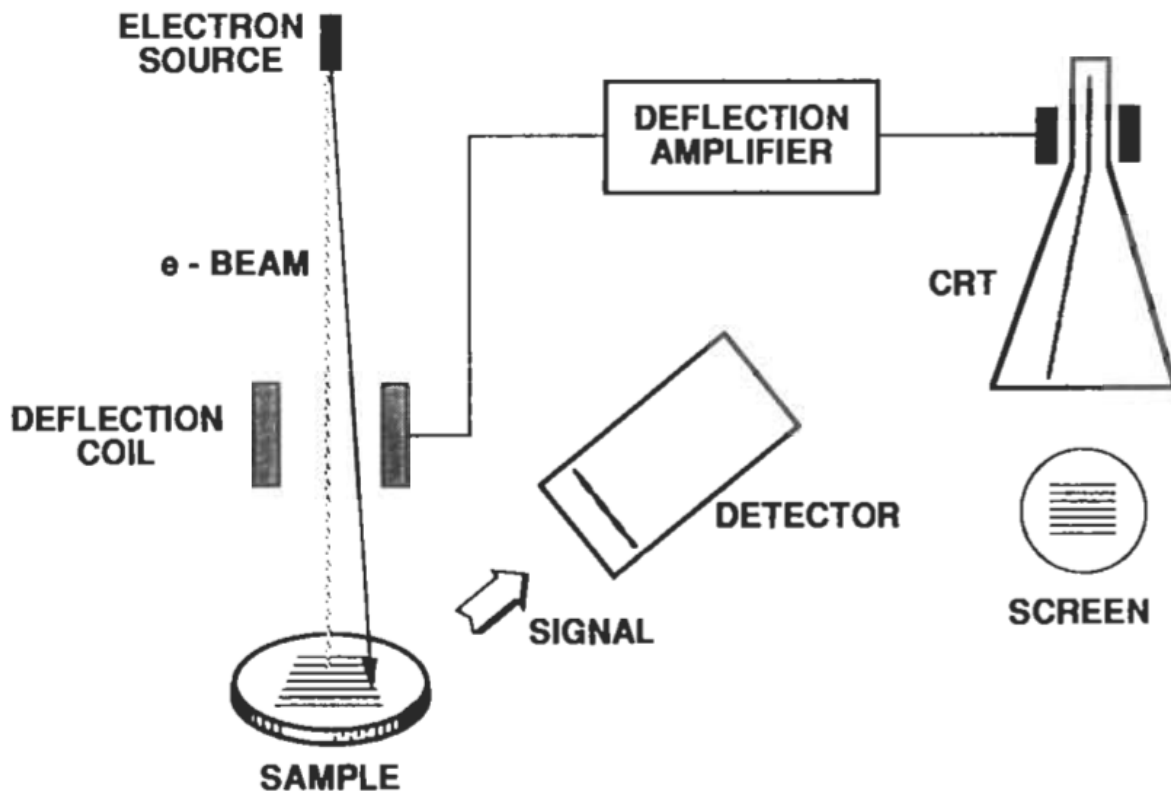


Figure 3-7. Simplified operation of a scanning electron microscope.

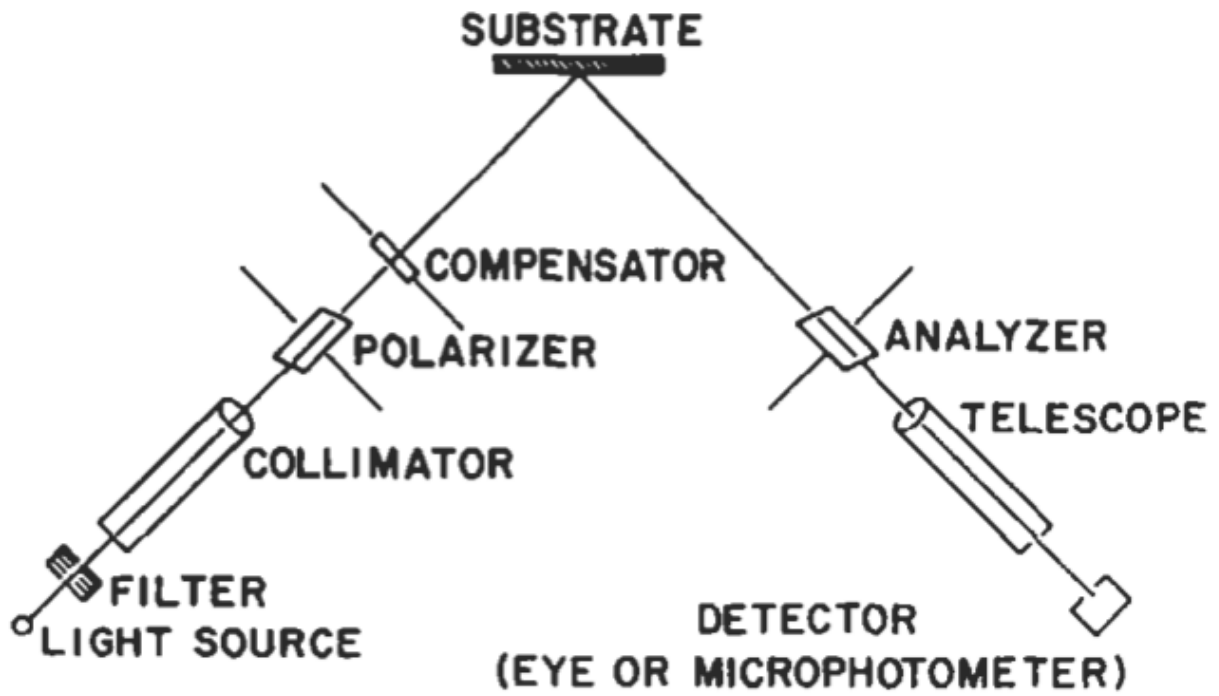


Figure 3-8. Common experimental arrangement for ellipsometry measurements.

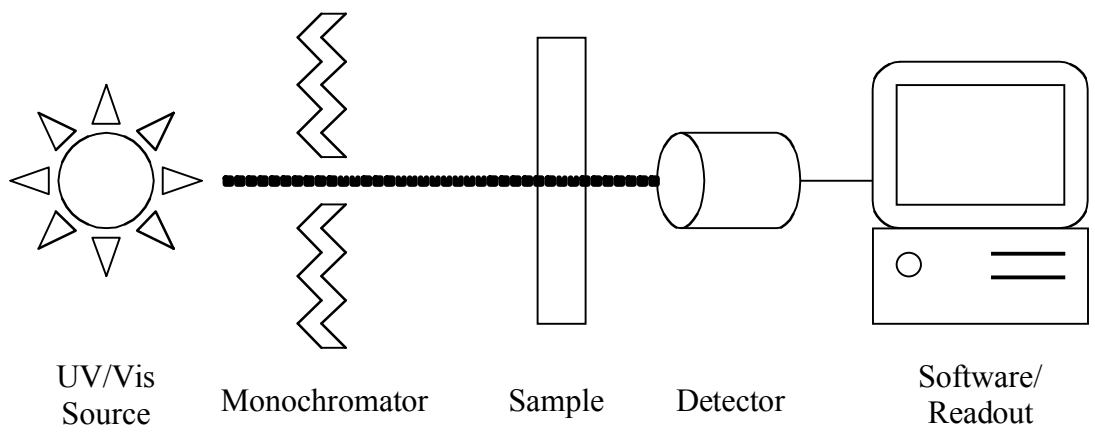


Figure 3-9. Simplified UV/vis spectrophotometer schematic.

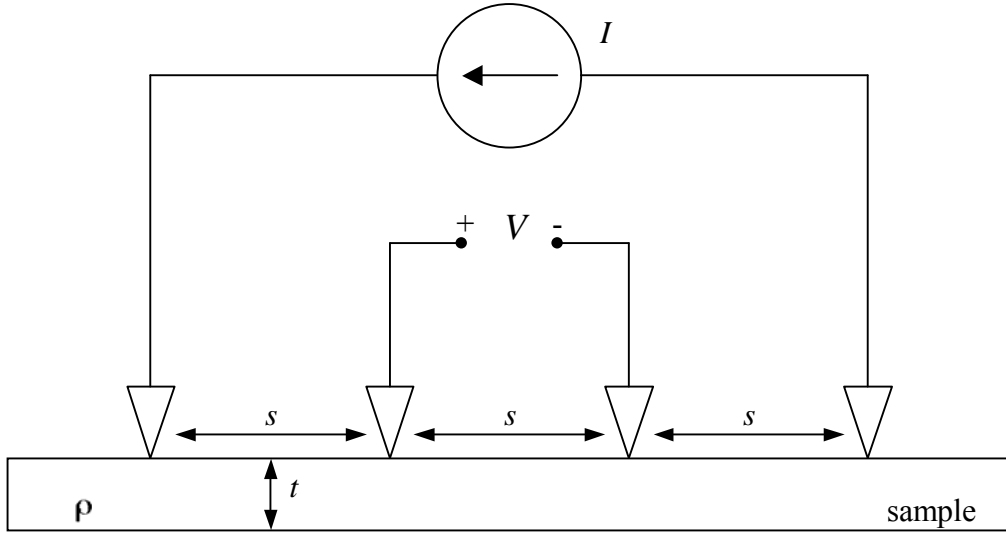


Figure 3-10. Four-point probe configuration schematic.

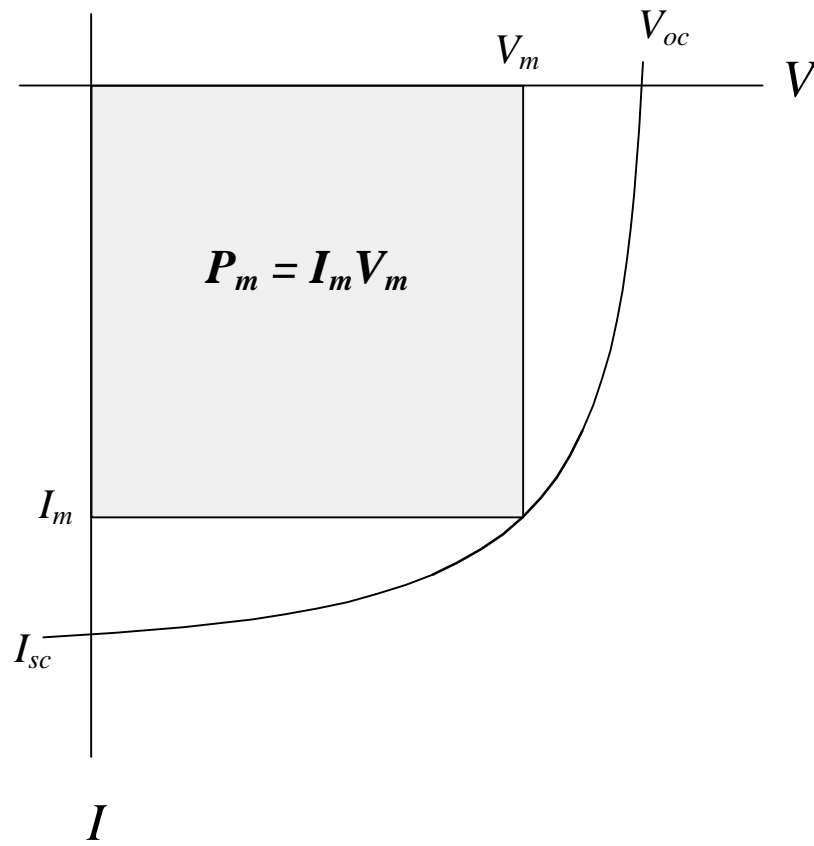


Figure 3-11. Example of a typical  $I$ - $V$  curve.

## CHAPTER 4 ZINC CADMIUM SULFIDE BUFFER LAYER GROWTH

### **Introduction**

The chemical bath deposition technique for thin film growth is gaining attention as it does not require expensive nor sophisticated equipment such as the vacuum systems required by other deposition processes. In fact, chemical bath deposition can be performed with a few beakers, a hot plate, and a magnetic stirrer, along with the proper starting chemicals, which are usually quite common and therefore generally inexpensive. These are important factors when it comes to cost reduction of photovoltaic devices; however there are many other advantages propelling the renewed interest in chemical bath deposition of thin films. For example, a large number of substrates can be processed simultaneously with chemical bath deposition. Also, there are few constraints regarding substrate requirements, and therefore any insoluble surface is most likely suitable for deposition. Low cost, substrate flexibility, and large throughput are some of the factors that make the chemical bath deposition technique such an attractive choice in photovoltaic device fabrication.

Zinc cadmium sulfide ( $\text{Zn}_x\text{Cd}_{1-x}\text{S}$ ) thin films are good candidates for development as a wide-bandgap window layer in photovoltaic devices. Depending on the amount of zinc, the bandgap of ZnCdS can be tailored from 2.4 eV (CdS) to 3.8 eV (ZnS). Many laboratory devices have reached high efficiencies of 16.5% [68], 19.5% [36], 15.0% [36], and 18.6% [62] using designs with CdS/CdTe, CdS/CIGS, CdS/CIS, and ZnS/CIGS structures, respectively, where the second material in each pair denotes the photovoltaic absorber layer. Using CdS as the buffer layer in these devices limits the attainable device efficiencies, as CdS buffer layers have a low bandgap energy, which causes considerable absorption in the short-wavelength region. One method to improving the blue response is to reduce the CdS buffer layer thickness, thereby

achieving increased short-circuit current ( $J_{SC}$ ). However, reducing the CdS thickness can adversely impact device open-circuit voltage ( $V_{OC}$ ) and fill factor ( $FF$ ) performance parameters as a result of the increased potential for pinhole formation in thinner films. Depositing a buffer layer material with a higher bandgap would help alleviate the problems encountered with CdS thin films. The addition of Zn to CdS is an attractive alternative as it yields a more favorable conduction band alignment and provides a lattice parameter that more closely matches that of CIGS absorber material. Therefore, developing an alternative window layer with a higher bandgap based upon ZnCdS is a promising approach.

A number of deposition techniques have been used in creating cadmium sulfide and zinc sulfide thin films, including vacuum chemical vapor deposition [69-71], spray pyrolysis [72], chemical bath deposition [64, 73-75, 38, 76-81], evaporation [82, 83], successive ionic layer adsorption and reaction (SILAR) [84-86], and the dip technique [87, 88]. In addition to its low cost, chemical bath deposition (CBD) has a distinct advantage as it forms homogeneous films adequate for use in solar cell devices. Zinc cadmium sulfide film growth in the CBD technique is based upon the slow release of  $S^{2-}$  and the controlled release of  $Zn^{2+}$  and  $Cd^{2+}$  ions in the solution. Two common sulfiding agents normally used in this process are thiourea  $[(NH_2)_2CS]$  and thioacetamide  $[CH_3CSNH_2]$ .

To date, chemical bath deposition has proven more successful for CdS film deposition than for ZnCdS films. The addition of Zn in the chemical bath introduces problems, including the common problem of oxide formation in the chemical deposition bath. The process is additionally complicated as the solubility products of CdS ( $K_{sp} = 1 \times 10^{-28}$ ) and ZnS ( $K_{sp} = 3 \times 10^{-25}$ ) differ by several orders of magnitude. Several complexing agents have been utilized to study the conditions for co-deposition of Cd and Zn sulfide, such as triethanolamine

(TEA),  $\text{NH}_3$ , and hydrazine ( $\text{N}_2\text{H}_4$ ). The different stability constants for the dominant cadmium and zinc precursors further narrow down the proper chalcogenide operating window and make control of the deposition process particularly difficult [89].

In some cases a second complementary complexing agent is preferred for enhanced Zn incorporation in the film [90]. Another approach is the deposition of CdS/ZnS multilayers for subsequent processing [91]. There is much disagreement concerning the best approach to achieve an optimal deposition of ZnCdS thin films, justifying the need for additional studies concerning ZnCdS deposition. In this study we hope to provide additional insight to the incorporation of zinc in ZnCdS thin films deposited by chemical bath deposition.

### **Chemical Bath Deposition of Zinc Cadmium Sulfide**

In this work, chemical bath deposition of zinc cadmium sulfide thin films is carried out with the use of four source solutions, namely a cadmium source solution, a sulfur source solution, a zinc source solution, and an ammonia source solution. The fractional composition of zinc in the chemical bath is controlled by mixing dose solutions of all four source solutions in specific proportions. The amount of source solution required for buffer layer deposition depends on the desired fractional composition of zinc relative to cadmium, defined by the fractional composition formula

$$x_{p,b,f} = \frac{[Zn]}{[Zn] + [Cd]} \quad (4-1)$$

where  $[Zn]$  and  $[Cd]$  are the respective molar concentrations of zinc and cadmium. The subindex  $p$ ,  $b$ , or  $f$  on the fractional composition,  $x$ , is used to specify the zinc composition in the prepared bath solution, the actual bath solution, and in the deposited film.

The relaxed restrictions on substrates means that chemical bath deposition can be used to deposit thin films on a variety of substrates. Whereas device fabrication requires buffer layer

deposition on Mo-coated soda-lime glass (SLG) substrates covered with some type of CIGS absorber, for development and characterization purposes zinc cadmium sulfide films are deposited on bare SLG substrates.

The chemical bath deposition procedure involves a protocol for cleaning substrates, preparation of cadmium, sulfur, zinc, and ammonia dose solutions, mixing of dose solutions to carry out the layer growth, and termination of growth.

### **Materials**

Four source solutions serve as the basis of this chemical bath deposition technique, which finds its roots in a patent from Boeing. First, a cadmium source solution is prepared by combining 3.84 g cadmium chloride hydrate (Alfa Aesar Item # 10661) and 2.78 g ammonium chloride (Alfa Aesar Item # 10632) with 2000 mL deionized water. Second, a sulfur source solution is prepared by mixing 12.69 g thiourea (Alfa Aesar Item # 36609) with 2000 mL deionized water. Third, a zinc source solution is created by the addition of 10 g zinc chloride hydrate (Alfa Aesar Item # 35782) to 400 mL of deionized water. Ammonium chloride (Alfa Aesar Item # 10632) is then added until the white dissipation dissolves, leaving a clear solution. Fourth, an ammonia source solution is prepared by mixing 50 mL of 28%-38% ammonium hydroxide (Fisher Scientific Item # AC20584-0010) with 350 mL deionized water. Each source solution is thoroughly agitated for at least 60 minutes after preparation, and is also agitated for a minimum of 15 minutes prior to its use.

### **Growth Procedure**

The growth of zinc cadmium sulfide thin films via chemical bath deposition follows a strict procedural sequence. All substrates and equipment must be thoroughly cleaned before deposition. The chemical bath solution is formulated through the extraction of a dose volume of each source solution selected so that the mixing of all four dose solutions results in a bath that

has a target fractional composition of zinc,  $x_p$ . The dose solutions are added to the reaction vessel in a step-wise fashion under stringent control of the chemical bath temperature. Once a desired growth duration is achieved the deposition is terminated and the substrates are thoroughly cleaned of any visibly loose powder by rinsing with deionized water.

For deposition on glass substrates, Corning 1737 is chosen for its superior characteristics over typical soda-lime glass, which boasts anneal and strain points almost 200°C higher. The lower thermal expansion coefficient of the Corning 1737 glass results in less warp and distortion in substrates exposed to thermal gradients during substrate processing.

### **Substrate and equipment cleaning**

Glass substrates must be thoroughly cleaned before their use in deposition. The first preparation step involves thoroughly washing each substrate with deionized water to remove any visible contaminants that may be present on the surface. Once each substrate has been individually rinsed they are placed in a Teflon substrate holder and transported to a hot deionized water bath held at a temperature of 80°C. The substrates remain in this first hot deionized water bath for at least 20 minutes before being removed. Each substrate is individually removed from the holder and mechanically cleaned with an Alconox detergent solution. The substrates are thoroughly rinsed with deionized water to ensure complete removal of the detergent solution. Once all substrates have been mechanically scrubbed and rinsed they are placed back in the substrate holder and delivered to an ultrasonic cleaner for a period of at least 20 minutes. Upon completion of the ultrasonic cleaning, the samples are again placed in an 80°C deionized water bath for at least 20 minutes. The substrates are then removed and placed in a three-step cascade of deionized water and nitrogen for 30 minutes. Lastly, the substrates are removed from the

cascade wash and dried thoroughly with nitrogen gas, and are stored in a clean and dry environment until use.

Device fabrication requires less preparation before each deposition step, as the substrates are originally cleaned before CGS or CIGS absorber deposition. To keep these samples clean, all device substrates are vacuum sealed after each deposition step. Samples are removed as needed for each processing step, and sealed again immediately after processing. Device samples are thoroughly cleaned with nitrogen gas before CBD buffer layer deposition.

Before buffer layer deposition, it is necessary to ensure that all equipment, including the jacketed reaction vessel, graduated cylinders, pipettes, beakers, and stirrers, are thoroughly and repeatedly washed in deionized water.

### **Preparation of dose solutions**

The desired fractional composition of zinc in the CBD bath is obtained by mixing specific amounts of dose solutions. Table 4-1 lists the dose solution volumes that are required to prepare chemical baths with various fractional compositions of zinc,  $x_p$ . For example, a chemical bath with fractional composition of zinc  $x_p = 0.3$  can be prepared using 106.7 ml of cadmium dose solution, 2.09 ml of zinc dose solution, 100 ml of sulfur dose solution, and 0.25 ml of ammonia dose solution. Table 4-2 takes into account 490 mL of deionized water that is initially added to the reaction vessel, and lists final bath volumes and concentrations. Again, for the example of  $x_p = 0.3$ , the final chemical bath solution has a total volume of 709 mL, and has cadmium and zinc concentrations of 1.264 mM and 0.542 mM, respectively.

### **Bath temperature conditioning**

The chemical bath should be kept at the desired target temperature at all times during film growth. This can be achieved either through manual adjustment or automatic feedback from a closed-loop thermocouple system. An external temperature sensor is used to report the chemical

bath temperature to the control unit. The closed-loop system is able to automatically make all adjustments to the hot water circulation in order to maintain the given set point temperature.

### **Buffer layer deposition**

The procedure for chemical bath deposition involves the step-wise addition of dose solutions, and the timely immersion and removal of substrates. First, 490 mL of deionized water is placed in the reaction vessel and the hot water circulator control unit is set to the desired growth temperature. All openings of the reaction vessel are covered with a plastic film that is only temporarily and briefly removed when adding either a substrate or dose solution. Mixing of the chemical bath solution is achieved by the use of a magnetic stirrer.

Once the target growth temperature has been reached, the cadmium dose solution is slowly added to the reaction vessel. Substrates are first cleaned with nitrogen gas, placed in Teflon holders, and the holders are immersed in the reaction vessel.

Next, after the bath temperature returns to within two degrees of the target value, the sulfur dose solution is slowly added to the reaction vessel, followed by the zinc dose solution. In addition, the ammonia dose solution is added to 10 mL deionized water in a separate beaker. Then, when the target growth temperature recovers to within two degrees, the diluted ammonia dose solution is quickly poured into the reaction vessel, starting the reaction. The chemical bath eventually becomes cloudy, with a milky-white color. Depending on the growth temperature and the bath composition, this cloudiness can persist for as long as 40 minutes, yet depending on the bath composition generally transitions to a transparent yellow color after 20 or 25 minutes.

### **Termination of growth**

After the desired deposition time has elapsed, the Teflon holders are removed from the chemical bath solution and immediately rinsed in deionized water. The substrates must be thoroughly rinsed until no loosely-bound powder remains on the surface. If a visual inspection

reveals that powder remains, the substrates are ultrasonically cleaned until powder is no longer evident. The substrate is then thoroughly dried with nitrogen gas and vacuum sealed or stored in a clean, dry environment.

### **Zinc Cadmium Sulfide Buffer Layer Characterization Results**

The effect of zinc concentration on chemical bath deposition of zinc cadmium oxide is presented. The thickness of ZnCdS films is determined via profilometry. The zinc incorporation of deposited film is determined by inductively coupled plasma spectroscopy and x-ray photoelectron spectroscopy. UV/vis spectroscopy is employed to determine the optical characteristics of CBD grown ZnCdS in the range of 300 nm to 800 nm.

#### **Growth Rate**

The growth rate of ZnCdS thin films deposited via CBD is determined by measuring film thickness at different deposition times. After deposition, AZ Electronic Materials 1529 Photoresist is applied to the portions to be measured. The covered films are soft-baked for approximately 10 minutes at 120°C. The exposed ZnCdS film is then etched with a 10% nitric acid solution, until only the film covered by the photoresist is left on the substrate. The substrate is then rinsed with deionized water, the remaining photoresist removed with acetone, and the sample is again thoroughly rinsed in deionized water. Film thickness is then measured using a Veeco Dektak 150 profilometer.

Zinc cadmium sulfide average film thickness is reported in Table 4-3 and shown in Figure 4-1 as a function of deposition time at 85°C for films grown with prepared fractional zinc compositions of  $x_p = 0.1, 0.2, 0.3, 0.4,$  and  $0.5$ . For each prepared zinc composition, four samples are deposited simultaneously. Deposition time is controlled by removing samples at 15, 25, 35, and 45 minutes. Measured ZnCdS average film thickness is reported on the vertical axis, with increasing deposition time on the horizontal axis. Each marker shape represents a specific

prepared fractional zinc composition as denoted in the legend. For example, average thicknesses of 26.7 nm and 55.0 nm were measured for a prepared zinc composition of  $x_p = 0.2$  at deposition times of 25 and 45 minutes, respectively. For all values of prepared zinc composition,  $x_p$ , ZnCdS film thickness is seen to increase with increasing deposition time. Film growth rate appears inversely related to the prepared zinc composition, as film thickness decreases with increasing content of zinc in the prepared bath solution.

### **Film Composition**

The film composition of ZnCdS thin films ( $x_f$ ) deposited via CBD is determined by ICP and XPS. A Perkin-Elmer Plasma 3200 is used for ICP measurements and a Perkin-Elmer PHI 5100 ESCA System is used for XPS measurements. Films are deposited for 45 minutes at 85°C with prepared fractional zinc compositions of  $x_p = 0.1, 0.2, 0.3, 0.4,$  and  $0.5$ . For XPS analysis, samples are cut and measured as received and after seven minutes of sputtering. For ICP, a 10% nitric acid solution is used to dissolve the deposited ZnCdS films. Table 4-4 reports the comparison between the two measurement techniques for films deposited for 45 minutes at 85°C.

The film fractional zinc compositions measured by ICP for films deposited for 45 minutes is shown in Figure 4-2. The fractional zinc composition measured in the film is reported on the vertical axis while the prepared fractional zinc composition is reported on the horizontal axis. The red dashed line corresponds to a 1:1 ratio of zinc composition in the prepared solution and in the as-deposited film. Prepared zinc compositions of  $x_p = 0.1$  and  $x_p = 0.2$  result in less incorporation of zinc into the film, where film zinc compositions of  $x_f = 0.05$  and  $x_f = 0.02$  were measured by ICP. The opposite of this trend is seen with prepared zinc compositions of  $x_p = 0.4$  and  $x_p = 0.5$ , where film zinc compositions ( $x_f$ ) were measured to be  $x_f = 0.65$  and  $x_f = 0.81$ . However, a prepared zinc composition of  $x_p = 0.3$  results in a film fractional zinc composition of

$x_f = 0.32$  which means that Zn and Cd are depositing in the same ratios as found in the chemical bath solution.

To determine the effect of deposition time on film composition, ICP was used to measure films deposited at 85°C for 15, 25, 35, and 45 minutes. Figure 4-3 presents the results of the measured fractional zinc composition ( $x_f$ ) as a function of deposition time for prepared zinc compositions of  $x_p = 0.1, 0.2, 0.3, 0.4,$  and  $0.5$ . The measured fractional zinc composition is graphed on the vertical axis while increasing deposition time is graphed on the horizontal axis. It appears that for values of  $x_p \geq 0.2$  zinc is incorporated into the film faster than cadmium. For example, for  $x_p = 0.3$ , the film zinc composition is  $x_f = 0.79$  after 15 minutes,  $x_f = 0.65$  after 25 minutes,  $x_f = 0.49$  after 35 minutes, and finally  $x_f = 0.32$  after 45 minutes of deposition.

A visual comparison of the measured film zinc fraction ICP and XPS data in Table 4-4 is seen in Figure 4-4. The measured fractional zinc composition if plotted on the y-axis and the five values of prepared fractional zinc composition are plotted on the x-axis. Each measurement technique is assigned a specific shape as denoted in the legend. The two measurement techniques produce similar results at the high and low end of the prepared zinc composition spectrum. However, there is disagreement at a prepared zinc composition of  $x_p = 0.3$  where XPS reports values of  $x_f = 0.62$  as received and  $x_f = 0.46$  after seven minutes of sputtering.

### **Optical Characteristics**

The optical transmission of ZnCdS films is measured using a Perkin-Elmer Lambda 800 UV/Vis spectrophotometer. Films are deposited at 85°C with various deposition times of 15, 25, 35, and 45 minutes with prepared fractional zinc compositions of  $x_p = 0.1, 0.2, 0.3, 0.4,$  and  $0.5$ . In order to accurately measure the transmission of a single ZnCdS film, a 10% nitric acid solution is used to remove the film deposited on the back of all substrates. Figures 4-5 through 4-9 show the optical transmission as a function of wavelength for deposition times of 15, 25, 35,

and 45 minutes. For each figure, transmission is reported on the vertical axis and wavelength is reported on the horizontal axis. Each deposition time is assigned a line type as denoted in the legend, where SLG denotes bare soda lime glass with no ZnCdS deposition. For each prepared fractional zinc composition, the transmission below 500 nm decreases with increasing deposition time. This is expected as film thickness increases with increasing deposition time thereby decreasing optical transmission.

The measured transmission for films deposited for 45 minutes at 85°C as a function of prepared fractional zinc composition ( $x_p$ ) is shown in Figure 4-10. Transmission is reported on the vertical axis and wavelength is reported on the horizontal axis. Each prepared fractional zinc composition is assigned a line type as denoted in the legend. A distinct variation between prepared values of zinc can be seen at wavelengths less than 500 nm as  $x_p = 0.4$  produces a film with increased transmission compared to the film grown with a prepared bath of  $x_p = 0.2$ . To further analyze the difference in transmission between these films, the average transmission for each prepared zinc value is calculated over three wavelength ranges, 300 nm to 800 nm, 300 nm to 550 nm, and 500 nm to 800 nm. Figure 4-11 plots the average transmission in each wavelength range for the ZnCdS films shown in Figure 4-10. Average transmission is plotted on the vertical axis and the prepared fractional zinc composition is plotted on the horizontal axis. The three wavelength range are assigned markers as denoted in the legend. The same data is listed in Table 4-5. Over the entire 300 nm to 800 nm range, the sample deposited with prepared zinc composition  $x_p = 0.4$  reports the highest average transmission value of 82.32%. Comparing the remaining two wavelength ranges, it is evident that the high average transmission value for  $x_p = 0.4$  is a result of its increased transmission at wavelengths less than 550 nm, with a 73.52%

average transmission compared to 64.29% average transmission for the film deposited with a prepared zinc composition of  $x_p = 0.2$ .

### Conclusions

Chemical bath deposition is an extremely attractive process as it provides a low cost method to producing high quality films with high throughput. In particular, chemical bath deposition is an excellent candidate for deposition of ZnCdS thin films for use as buffer layers in photovoltaic devices. The addition of Zn to the traditional CdS buffer layer results in a larger band-gap energy that aids to increase transmission in the short-wavelength region. Zinc cadmium sulfide also yields a more favorable conduction band alignment and provides a lattice parameter that more closely matches CIGS absorber material.

Experimental studies show that thickness of ZnCdS film increases with increasing deposition time up to 45 minutes. Thickness is seen to be a function of the prepared fractional zinc composition, where film thickness decreases with increasing zinc content in the prepared bath. Deposited film zinc content is also seen to be dependant on the prepared zinc composition, where values of  $x_p = 0.1$  and  $0.2$  show less zinc incorporation into the film and values of  $x_p = 0.4$  and  $0.5$  result in fractional zinc composition of  $x_f = 0.65$  and  $0.81$  as reported by ICP, respectively. ICP results also show that a prepared zinc composition of  $x_p = 0.3$  results in a film with a zinc composition of  $x_f = 0.32$ , although slightly contradicted by XPS results. Zinc incorporation into the film is seen to be a function of deposition time, as the zinc-to-cadmium incorporation on the substrate is increased at reduced deposition times. Films deposited with prepared zinc compositions of  $x_p = 0.3$  and  $x_p = 0.4$  show average optical transmissions greater than 80% for wavelengths from 300 nm to 800 nm. In particular, it is critical to maximize transmission at wavelengths less than 550 nm to increase device short-circuit current and both of these films show average transmission of at least 70% in this region.

Table 4-1. Recipe for the preparation of the chemical bath solution for five different zinc compositions.

Prepared zinc composition ( $x_p$ )	Cd Source (mL)	Zn Source (mL)	S Source (mL)	NH <sub>4</sub> OH Source (mL)
0.1	137.10	0.70	100	0.25
0.2	121.90	1.40	100	0.25
0.3	106.70	2.09	100	0.25
0.4	91.40	2.79	100	0.25
0.5	76.20	3.49	100	0.25

Table 4-2. Resulting chemical bath solutions for five different zinc compositions.

Prepared zinc composition ( $x_p$ )	Overall bath volume (mL)	Cadmium concentration (mM)	Zinc concentration (mM)
0.1	738	1.560	0.173
0.2	724	1.415	0.354
0.3	709	1.264	0.542
0.4	694	1.106	0.737
0.5	680	0.941	0.941

Table 4-3. Zinc cadmium sulfide film thicknesses for five values of prepared fractional composition of zinc at 85°C.

Deposition Time (min)	Thickness (nm)				
	$x_p = 0.1$	$x_p = 0.2$	$x_p = 0.3$	$x_p = 0.4$	$x_p = 0.5$
15	22.5	17.5	13.3	12.5	8.3
25	37.5	26.7	20.0	17.5	13.3
35	60.0	37.5	31.7	27.5	16.7
45	80.0	55.0	43.3	37.5	22.5

Table 4-4. Comparison of measured fractional zinc composition in films deposited for 45 minutes with five prepared zinc compositions at 85°C.

Prepared Fractional Zinc Composition ( $x_p$ )	Fractional Composition (%)		
	ICP	XPS (as received)	XPS (7 min sputter)
0.1	0.05	0.00	0.00
0.2	0.02	0.00	0.00
0.3	0.32	0.62	0.46
0.4	0.65	0.69	0.65
0.5	0.81	0.76	0.77

Table 4-5. Average transmission of three wavelength ranges for ZnCdS films deposited for 45 minutes with five prepared zinc compositions at 85°C.

Prepared Fractional Zinc Composition ( $x_p$ )	Wavelength Range		
	300nm - 550nm	550nm - 800nm	300nm - 800nm
0.5	70.03	90.66	80.31
0.4	73.62	91.07	82.32
0.3	70.01	90.76	80.36
0.2	64.29	91.25	77.73
0.1	67.29	92.69	79.95

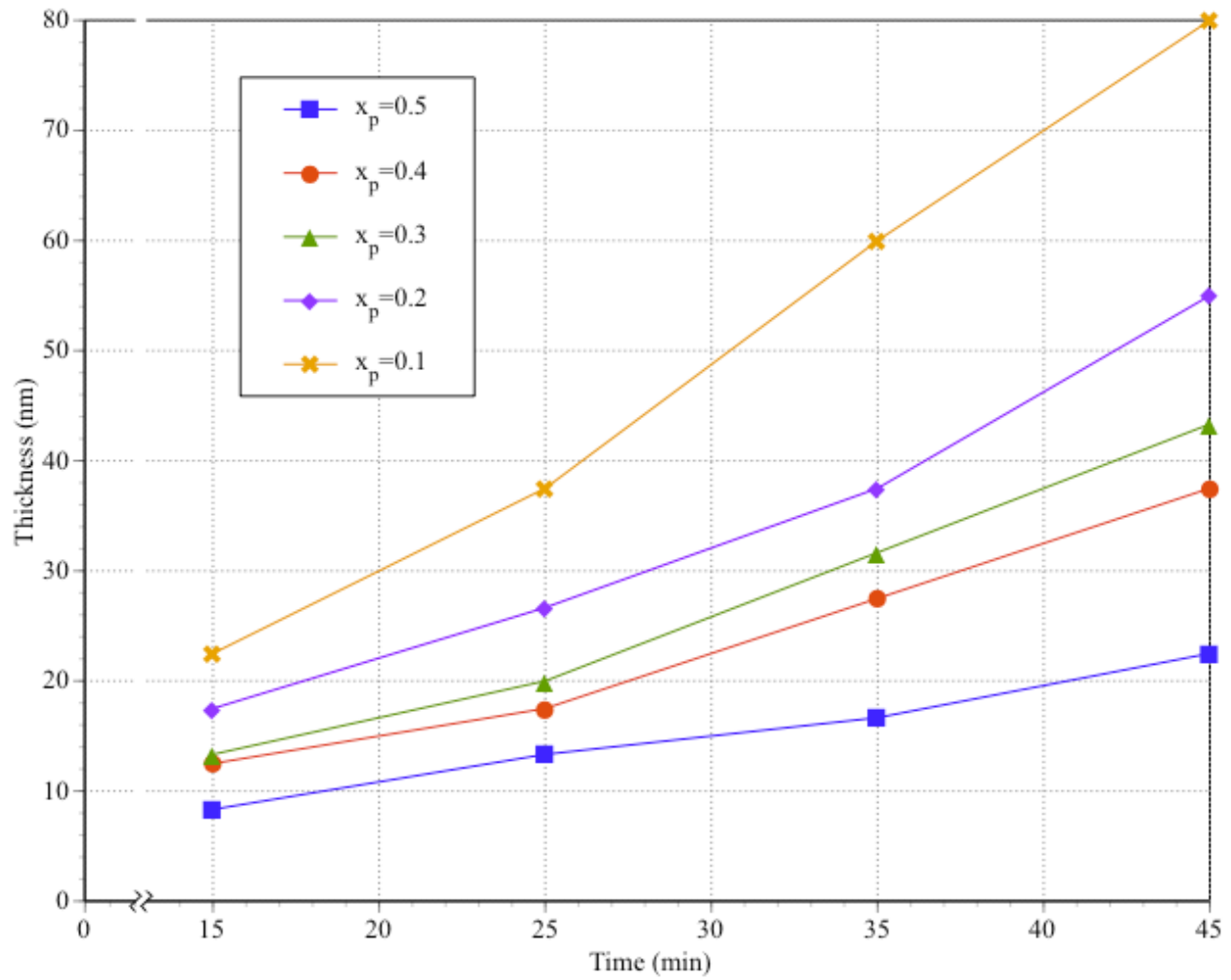


Figure 4-1. Film thickness as a function of deposition time for ZnCdS chemically bath deposited at five prepared fractional zinc compositions at 85°C.

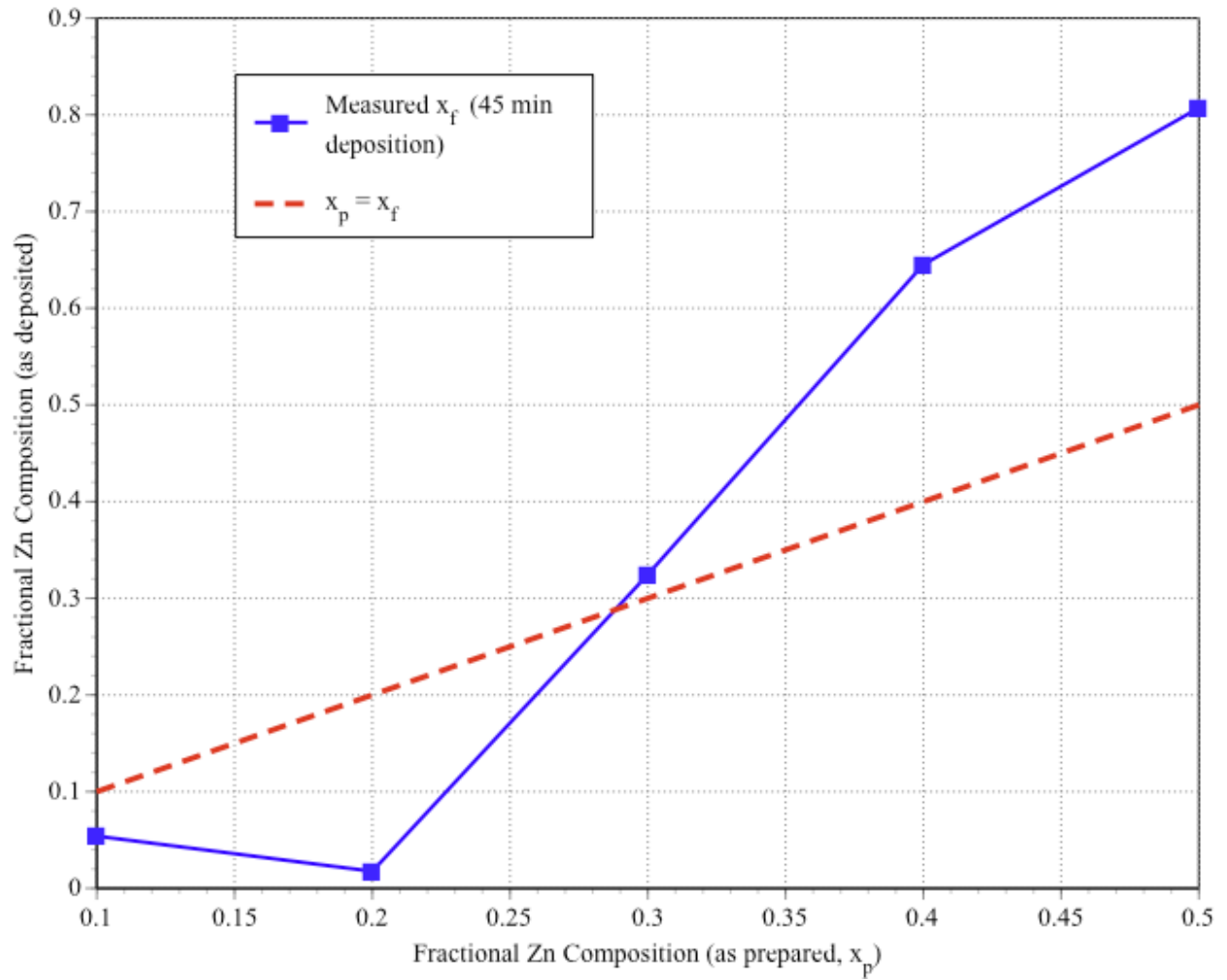


Figure 4-2. Measured fractional zinc composition ( $x_f$ ) of five films chemically bath deposited at 85°C for 45 minutes at five prepared zinc compositions,  $x_p = 0.1, 0.2, 0.3, 0.4,$  and  $0.5$ .

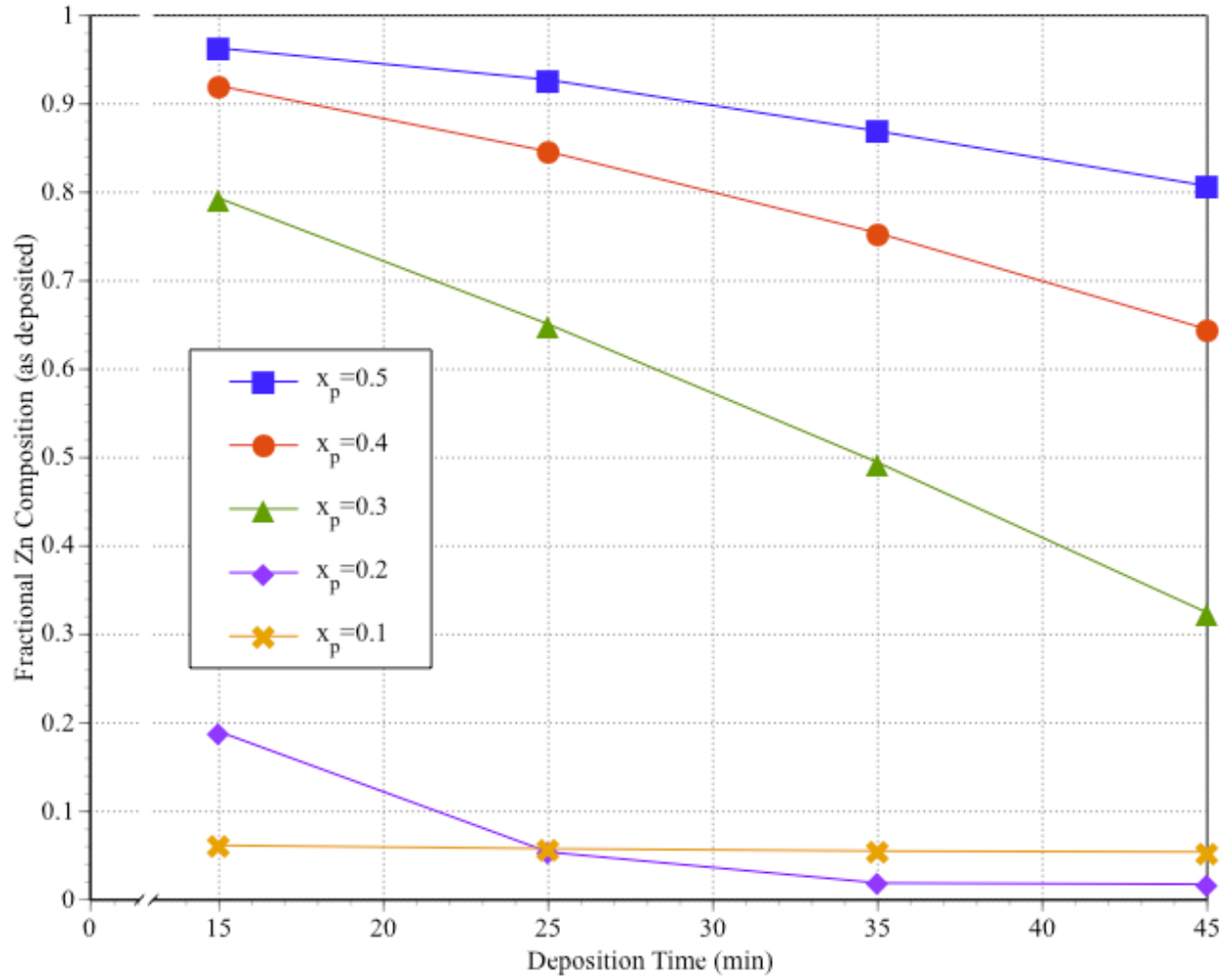


Figure 4-3. As deposited fractional zinc composition,  $x_f$ , as a function of deposition time for five prepared zinc compositions,  $x_p = 0.1, 0.2, 0.3, 0.4,$  and  $0.5$ , at  $85^\circ\text{C}$ .

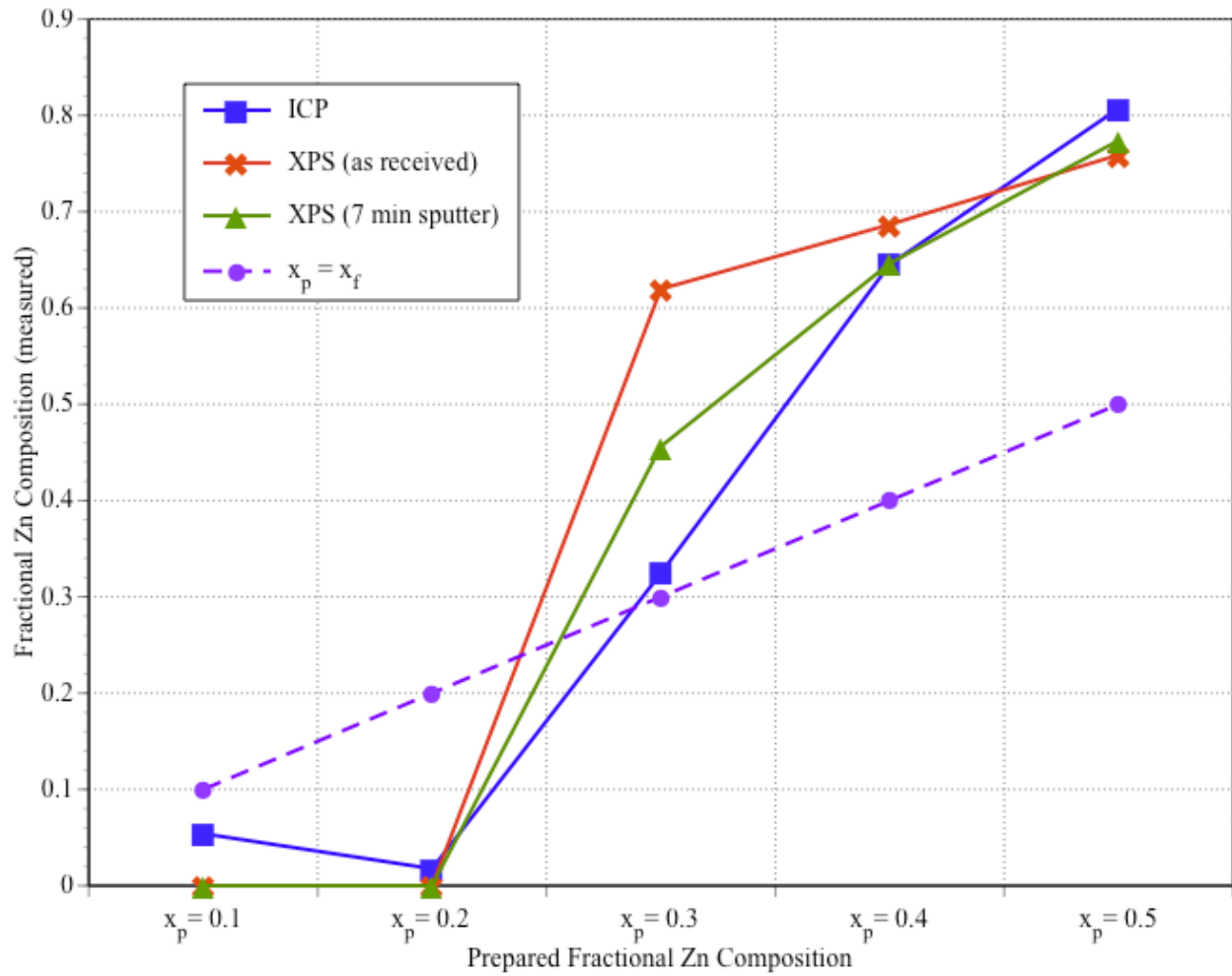


Figure 4-4. Comparison of measured zinc composition of films deposited at 85°C for 45 minutes with prepared fractional zinc compositions of  $x_p = 0.1, 0.2, 0.3, 0.4,$  and  $0.5$ .

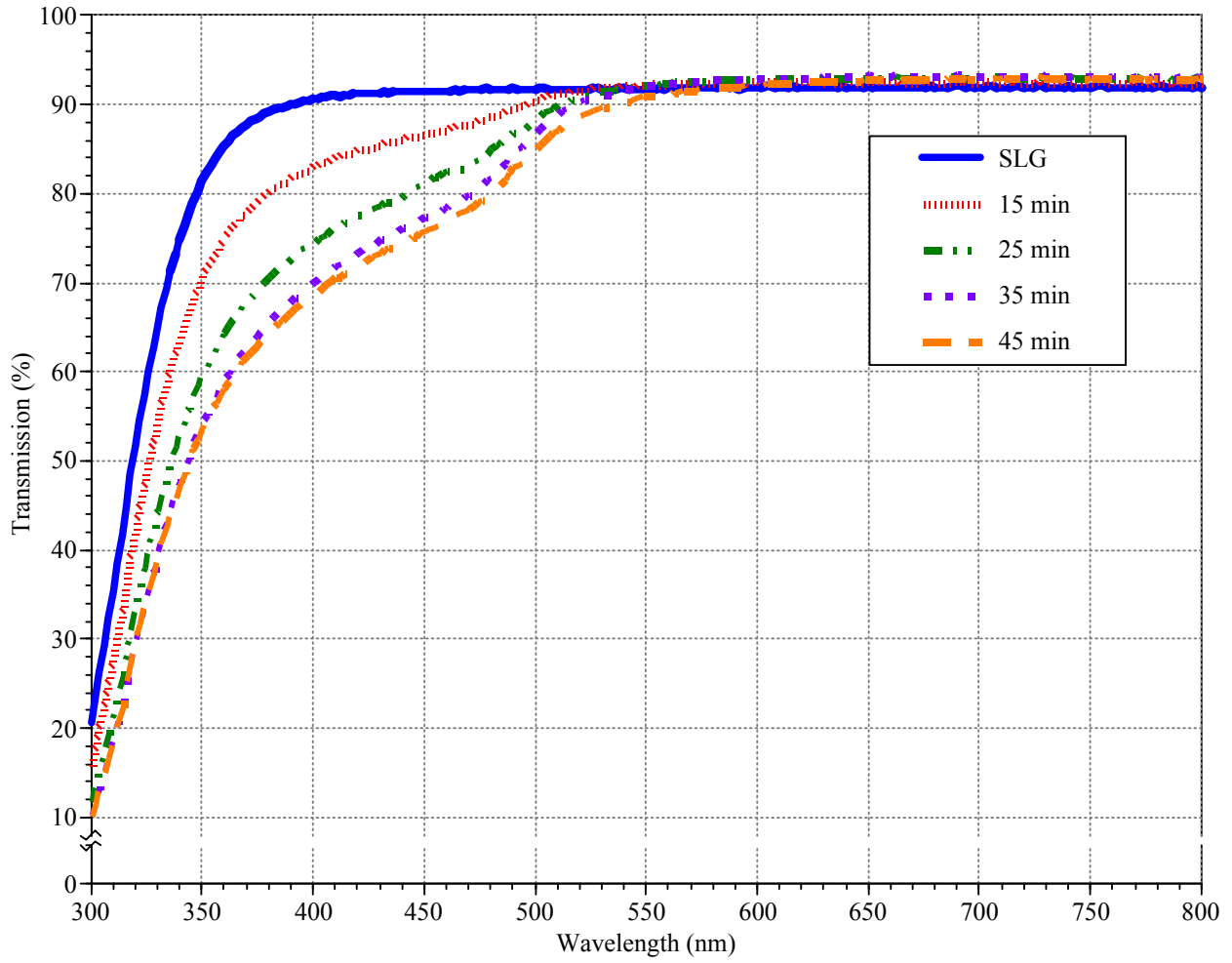


Figure 4-5. Optical transmission as a function of wavelength for films deposited at 85°C with a prepared fractional zinc composition of  $x_p = 0.1$ , at deposition times of 15, 25, 35, and 45 minutes.

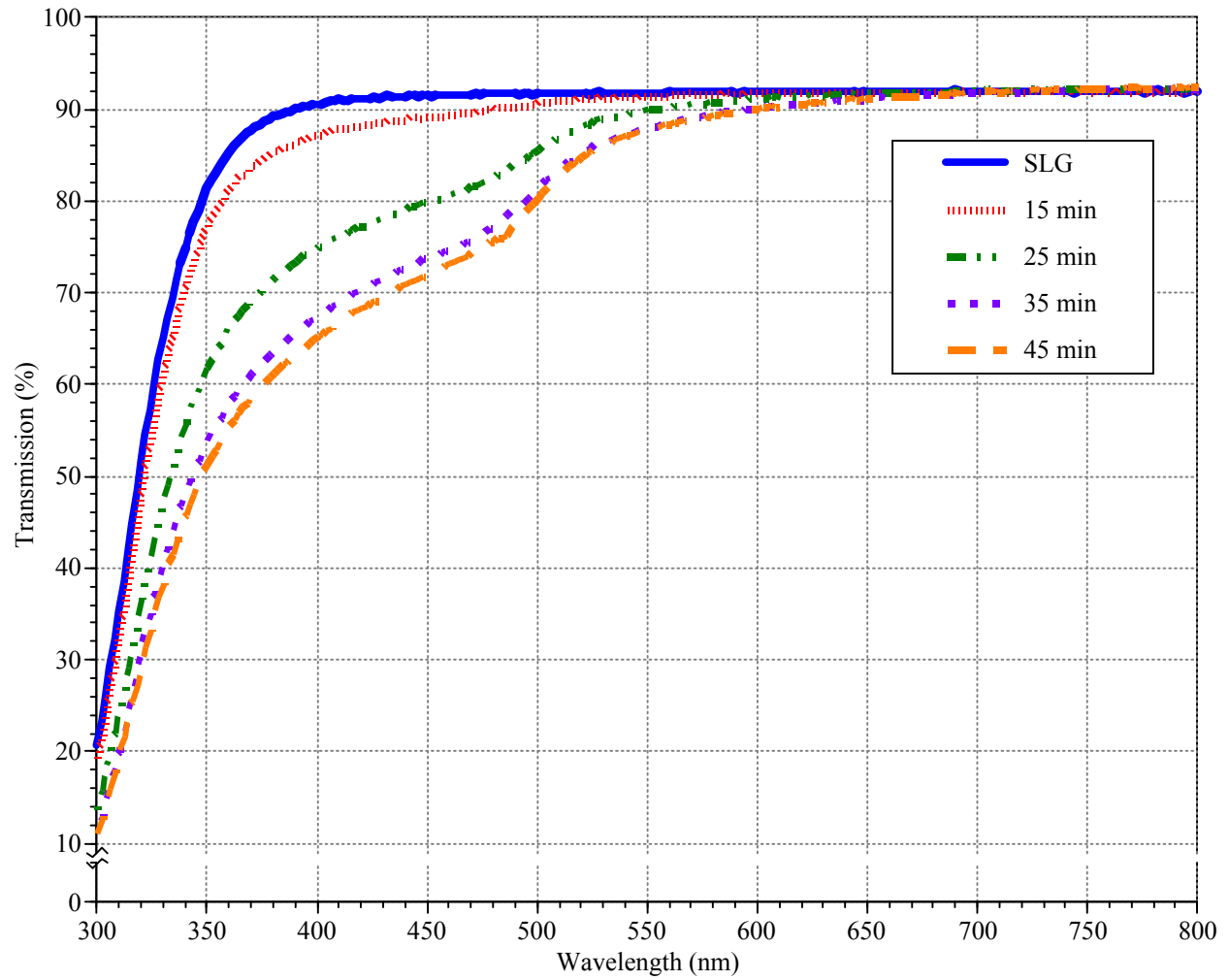


Figure 4-6. Optical transmission as a function of wavelength for films deposited at 85°C with a prepared fractional zinc composition of  $x_p = 0.2$ , at deposition times of 15, 25, 35, and 45 minutes.

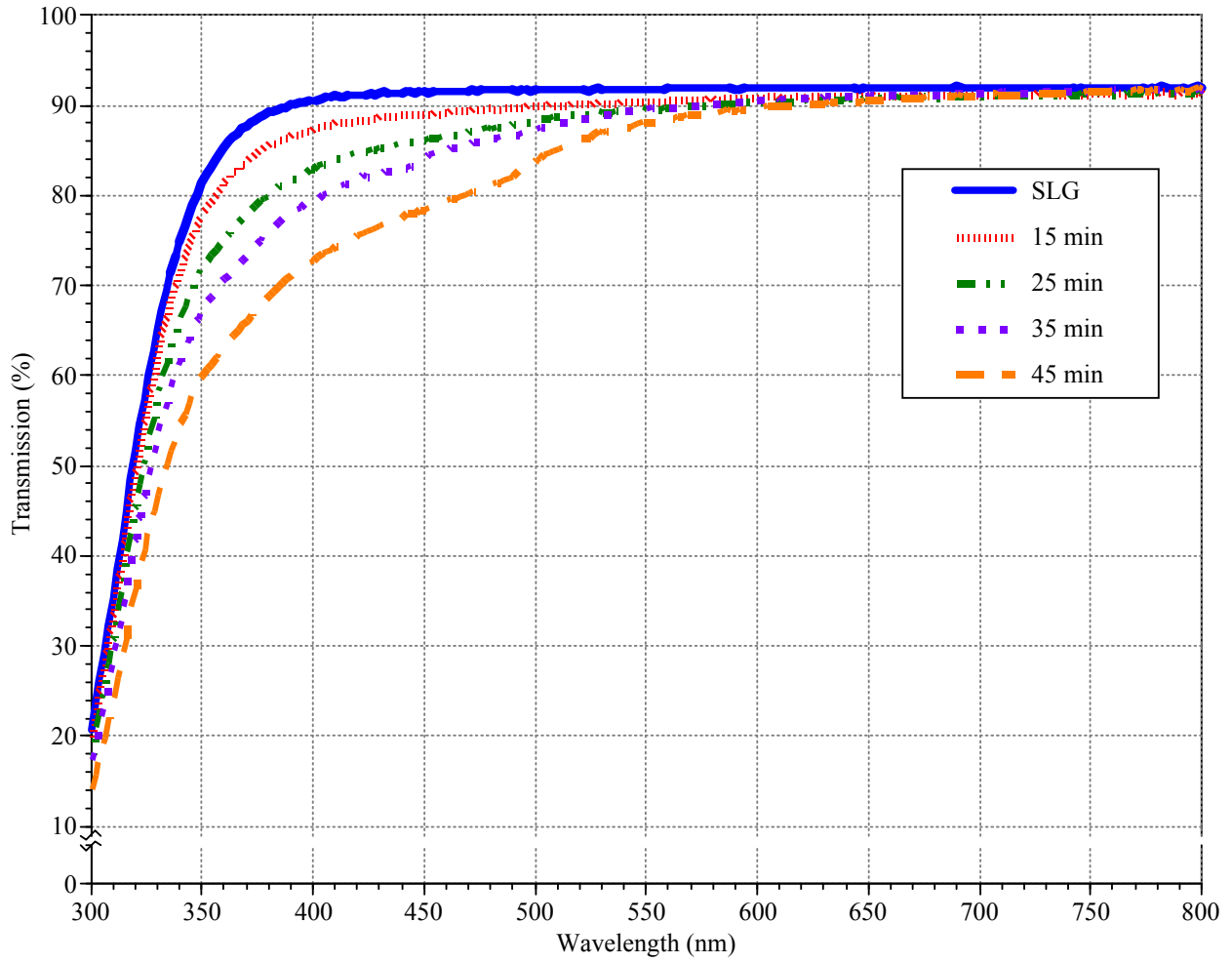


Figure 4-7. Optical transmission as a function of wavelength for films deposited at 85°C with a prepared fractional zinc composition of  $x_p = 0.3$ , at deposition times of 15, 25, 35, and 45 minutes.

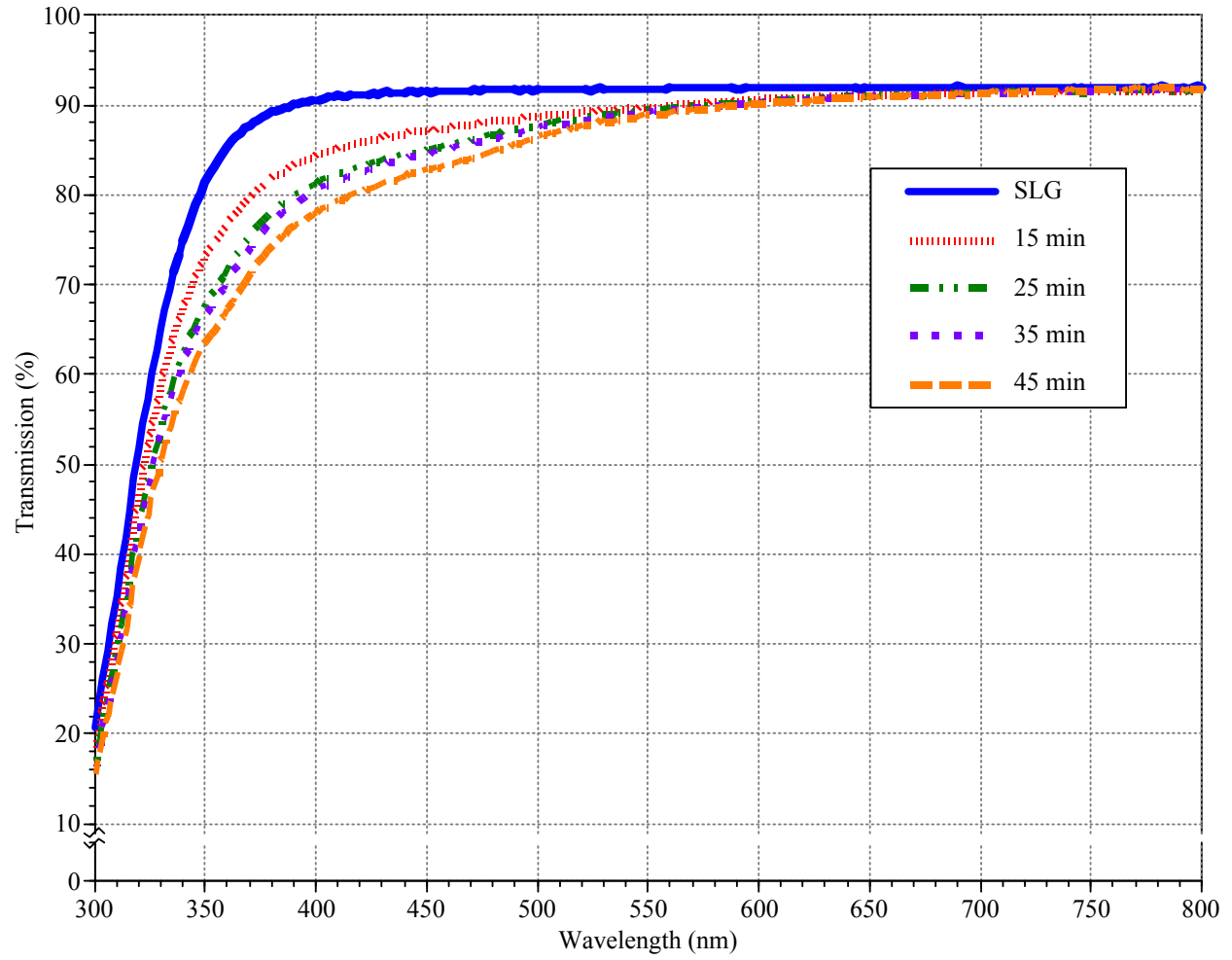


Figure 4-8. Optical transmission as a function of wavelength for films deposited at 85°C with a prepared fractional zinc composition of  $x_p = 0.4$ , at deposition times of 15, 25, 35, and 45 minutes.

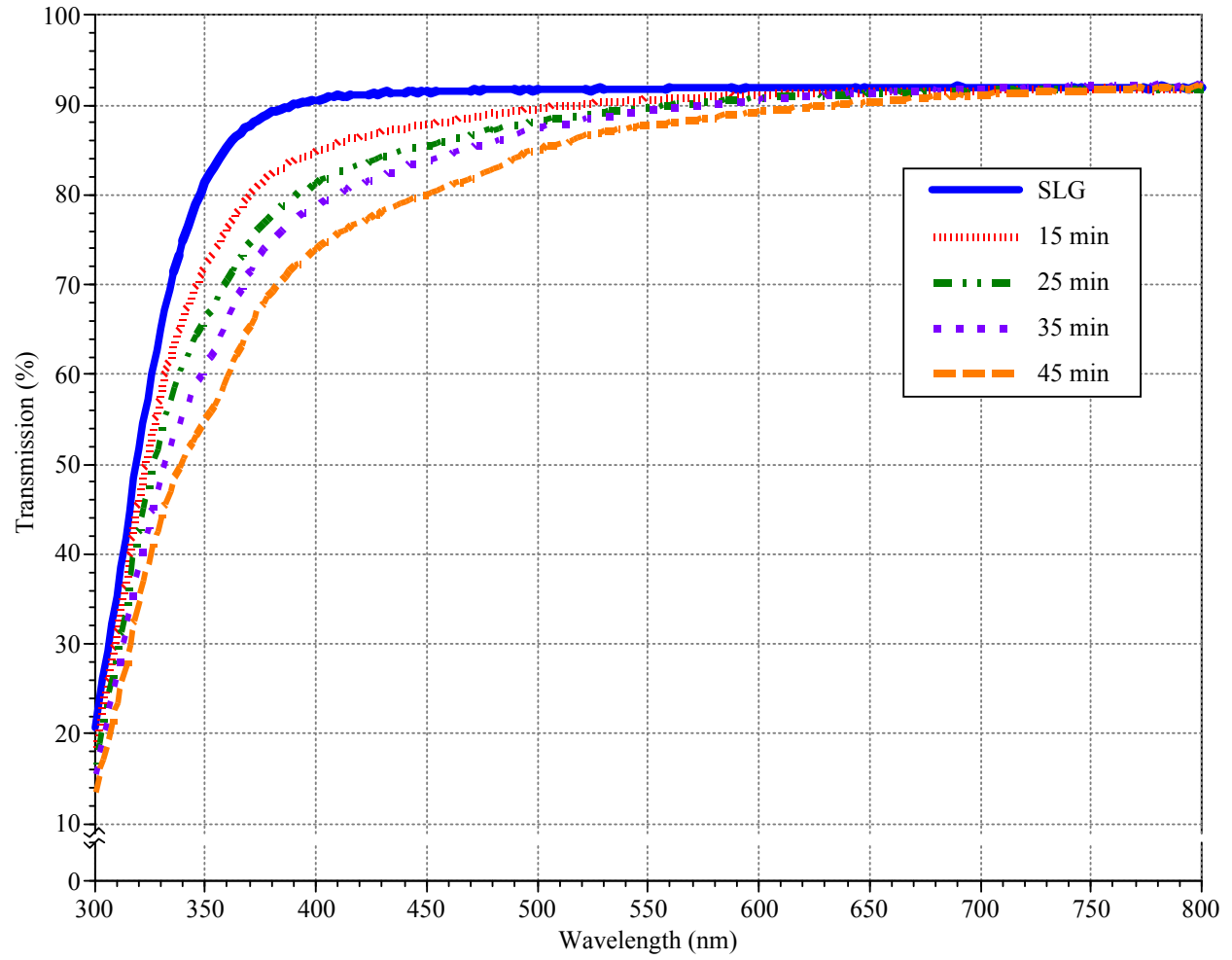


Figure 4-9. Optical transmission as a function of wavelength for films deposited at 85°C with a prepared fractional zinc composition of  $x_p = 0.5$ , at deposition times of 15, 25, 35, and 45 minutes.

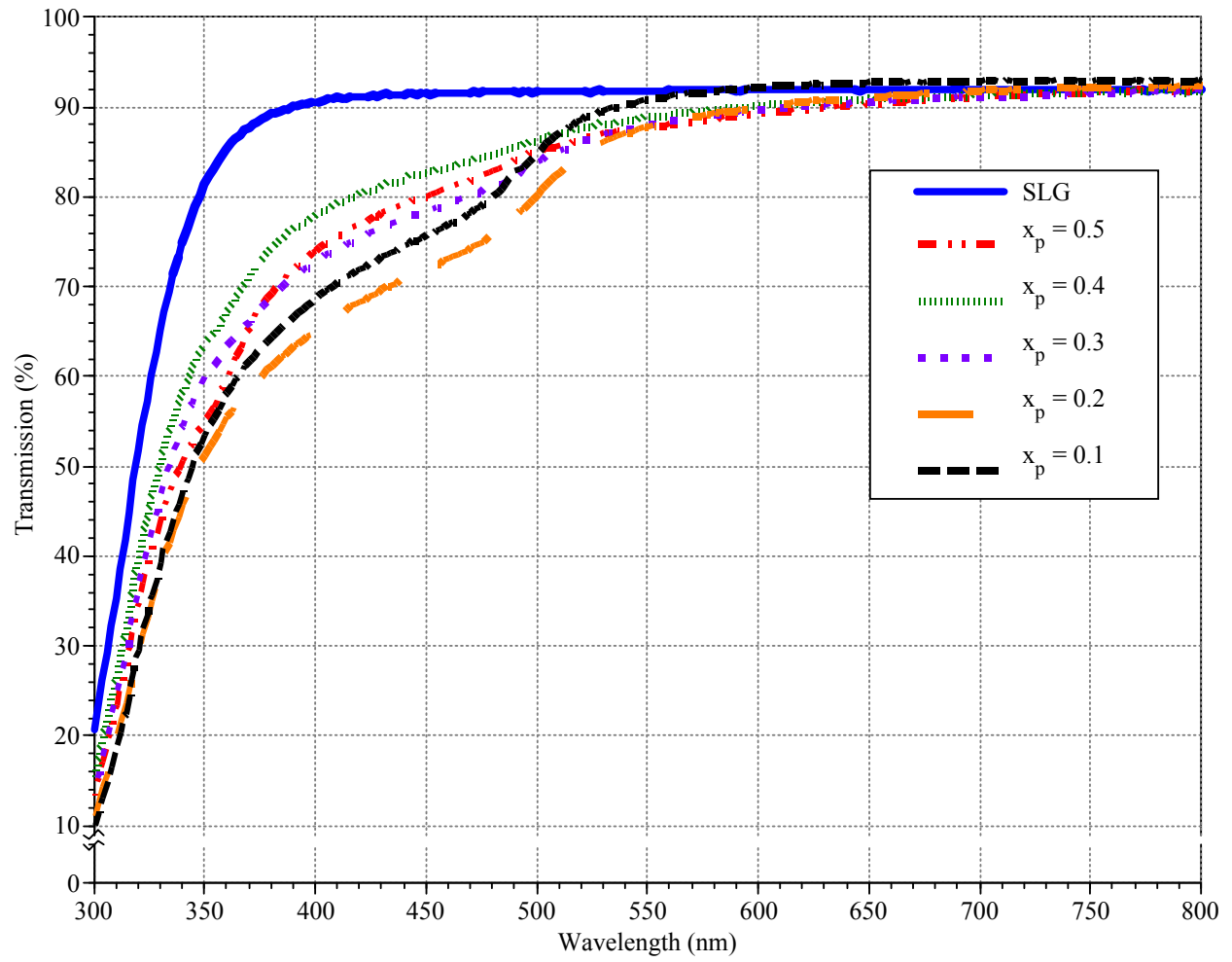


Figure 4-10. Optical transmission as a function of wavelength for films deposited at 85°C for 45 minutes with five prepared fractional compositions,  $x_p = 0.1, 0.2, 0.3, 0.4,$  and  $0.5$ .

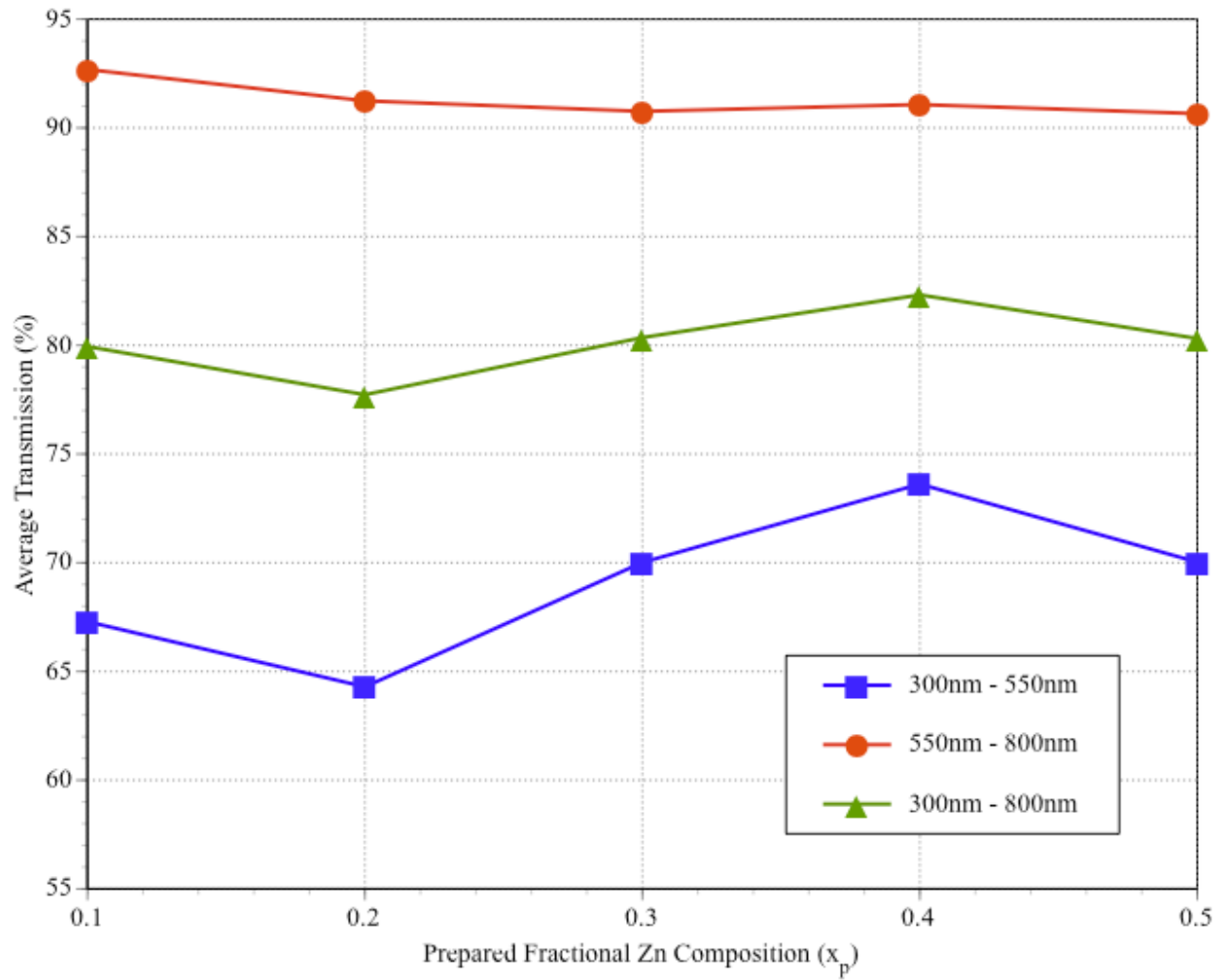


Figure 4-11. Average transmission of three wavelength ranges for ZnCdS films deposited at 85°C for 45 minutes with five prepared zinc compositions,  $x_p = 0.1, 0.2, 0.3, 0.4,$  and 0.5.

## CHAPTER 5 CHARACTERIZATION OF SPUTTER DEPOSITED ZINC OXIDE

### **Introduction**

Zinc oxide is a wide band-gap (3.3 eV) semiconductor with many technological applications such as gas sensors, phosphors, piezoelectric transducers, and transparent conducting electrodes in optoelectronic devices [92-94]. Zinc is inexpensive, non-toxic, and zinc oxide has several advantages over other TCO materials including high transmittance in the short-wavelength region and is abundant in natural resource. Several deposition techniques such as pulsed laser deposition [95], sputtering [96-100], spray pyrolysis [101, 102], and chemical vapor deposition [103-105] have been used to deposit intrinsic zinc oxide thin films. Among these, sputtering is the most widely used as it has outstanding advantages such as simple apparatus, high deposition rates, low deposition temperature, large area deposition, good adhesion, and easy control of doping concentration. Unfortunately, it is very difficult to deposit intrinsic ZnO films that exhibit sufficiently high conductivity for use in optoelectronic devices.

Aluminum-doped zinc oxide (AZO) is a popular alternative [99, 106, 107] to intrinsic zinc oxide as it exhibits high transmittance, low resistivity, can be easily deposited, and its band-gap energy can be altered by changing the amount of aluminum dopant. The addition of hydrogen during sputtering is seen to significantly reduce the resistivity of AZO films [108]. It is believed that hydrogen acts as a shallow donor in ZnO thin films to achieve high performance, greatly improving the Al doping efficiency thereby enhancing the conductivity of the AZO thin films [109, 110]. For sputter deposited AZO, aluminum and hydrogen content, substrate temperature, working gas pressure, RF power, and the working distance are all parameters that can affect the structural, optical, and electrical properties of doped zinc oxide.

There is no single guaranteed recipe or deposition technique that yields Al:ZnO films with superior optoelectronic properties. Therefore, it is necessary to further investigate which knobs can be turned to produce the most optimal deposition conditions for the sputtering system at the University of Florida. The objective of this work is to determine the film characteristics of Al and H doping of ZnO sputter deposited films and intends to improve upon the quality of AZO and HAZO by investigating a number of factors that influence film thickness, sheet resistance, optical transmission, and structural characteristics. In addition, it is desired to deposit zinc oxide at higher base pressures in hopes of achieving the potential for increased industrial throughput while maintaining or improving film properties.

### **Experimental**

This work consists of sputter deposition of Al:ZnO (AZO) and H-Al:ZnO (HAZO) thin films on glass substrates. Samples are deposited via rf magnetron sputtering using argon and hydrogen-doped argon working gas. Four-point probe and uv/vis spectroscopy are used to measure film resistivity and optical transmission. Film thickness is measured using profilometry and powder x-ray diffraction is used to analyze the structural characteristics of AZO and HAZO films. A figure of merit calculation is calculated for each film to determine which process conditions achieve optimal film characteristics.

### **Equipment**

A Perkin-Elmer Model 4400 Production Sputtering system is used to sputter deposit zinc oxide thin films on Corning 1737 glass substrates with a base pressure of  $2.6 \times 10^{-6}$  Torr. Aluminum-doped zinc oxide is deposited using a zinc oxide target that is doped with  $\text{Al}_2\text{O}_3$  in an ultra-high purity Ar working gas environment. The content of  $\text{Al}_2\text{O}_3$  in the target is 2% in weight and measures eight inches in diameter. Hydrogen-aluminum-doped zinc oxide is

deposited using the Al<sub>2</sub>O<sub>3</sub> doped target along with an ultra-high purity Ar and H<sub>2</sub> (0.1%) sputtering gas mixture.

An Alessi four-point probe system is used to measure the resistivity of the sputter deposited films. The system features 0.05" spaced tungsten-carbide probe tips, which are 0.002" in diameter. Currents of 1  $\mu$ A to 100 mA are supplied by a Crytronics Model 120 current source. The voltage resulting across the inner probes is measured by a Keithley Model 181 Nanovoltmeter which is capable of 10 nV sensitivity. Optical transmission of the films is measured from 400 nm to 800 nm using a Perkin-Elmer Lambda 800 spectrophotometer. The system uses twin beams, tungsten and deuterium, to collect transmittance spectra and a reference sample to provide background correction of measured spectra.

The structural characteristics of the films are analyzed with a Philips APD 3720 powder diffractometer operating at 40KV and 20mA, which uses Cu  $\alpha$  radiation ( $\lambda = 0.154056$  nm). Survey spectra scans are run with a 0.03° step size and a step time of 0.5 second per step. High resolution spectra scans are produced by reducing the step size to 0.01° and increasing the scan rate to 1.0 second per step. The thickness of the films is obtained using a Veeco Dektak 150 Surface Profiler, which has a vertical measurement range of 512  $\mu$ m and can perform precise step measurements of thin films down to 100 Å.

## **Materials**

Zinc oxide thin films are sputter deposited on Corning 1737 glass substrates, which must be thoroughly cleaned before use. Glass substrates are washed with deionized water to remove visible contaminants and subjected to a series of hot deionized water baths. Substrates are mechanically scrubbed with an Alconox detergent solution, placed in a hot deionized water bath,

then ultrasonic cleaned, placed in a three-step cascade of deionized water, and finally dried with nitrogen gas. The glass substrate cleaning procedure is further detailed in Chapter 3.

Aluminum-doped and hydrogen-aluminum-doped films are sputtered from an 8-inch zinc oxide target doped with  $\text{Al}_2\text{O}_3$  (2wt%). Al-doped ZnO is deposited in an UHP Ar working gas environment while a mixture of UHP Ar and  $\text{H}_2$  (0.1%) serves as the working gas for H-Al-doped ZnO. Acetone is used to remove Sharpie ink when creating trenches for subsequent thickness measurements.

### **Zinc Oxide Characterization Results**

The effect of sputter deposition parameters such as sample positioning under the target and working gas flowrate is presented. The thickness of AZO and HAZO is determined via profilometry. Four-point probe measurements are used for electrical characterization of sputter deposited films in the form of sheet resistance and used in combination with film thickness to calculate resistivity. UV/Vis spectroscopy is used to determine the optical characteristics of annealed ZnO in the range of 400 nm to 800 nm. Structural characterization of AZO and HAZO thin films is performed via x-ray diffraction (XRD). A figure of merit calculation is used to select the growth parameters that produce films with superior optoelectronic properties.

#### **Film Thickness**

The thickness of Al:ZnO and H-Al:ZnO sputter deposited films is determined using a Veeco Dektak 150 profilometer. Average thickness is calculated by taking the mean of three measurements along the etched trench. Unless otherwise stated, the target is conditioned with a pre-sputter before opening the shutter to start deposition on the SLG substrates. The effect of flowrate and positioning under the target is analyzed for each working gas. The base pressure of the sputter deposition chamber is kept constant for all thickness experiments, on the order of

$2.6 \times 10^{-6}$  Torr. Films are sputtered from the  $\text{Al}_2\text{O}_3$ -doped zinc oxide target both for AZO and HAZO.

### **Aluminum doped**

A contour plot of aluminum-doped zinc oxide (AZO) film thickness is shown in Figure 5-1. The film is deposited for 10 minutes with 10 minutes pre-sputter of the target before opening the shutter to begin the deposition. The vertical axis represents the y-coordinate location under the sputter target and the horizontal axis represents the x-coordinate location. The color assignments denoted in the legend represent thickness equal to or less than their assigned thickness value. The RF power is kept at 0.4 kW during deposition with the argon working gas flowrate maintained at 40 sccm. The measured film thickness on the 6" x 6" sample is seen to reach a minimum of around 160 nm (2,3) and a maximum close to 300 nm (-2,-3). Film thickness is also seen to decrease toward the lower right hand area of the sample (2,-3). These lower areas of film thickness correspond to areas that are positioned closer to the edge of the target. In order to consistently compare films between experiments, four sample locations measuring 1" x 2" are defined as seen in Figure 5-2. These four sample positions are kept constant for all experiments by placing a grid on the substrate platen to ensure samples are accurately positioned for each deposition.

The average thickness of AZO deposited at four working gas flowrates is shown in Figure 5-3, and is calculated by averaging three measurements along the trench. The vertical axis plots the average thickness while the horizontal axis categorizes the deposited AZO by sample location under the target. Each working gas flowrate is assigned a marker style as denoted in the legend. For example, with an argon working gas flowrate of 40.0 sccm the average measured thickness at sample position 3 is 236.7 nm. The RF power is kept constant at 0.4 kW for all conditions, with a base pressure of approximately  $2.6 \times 10^{-6}$  Torr. The flowrate of argon

working gas is adjusted from 30.0 sccm to 60.0 sccm in 10.0 sccm increments. The average AZO measured thickness at each flowrate is roughly a function of working gas flowrate, which is directly related to working gas pressure. At position 4, 60.0 sccm Ar gives an average thickness of approximately 247 nm compared to 238 nm deposited at 30.0 sccm. This represents a 3.8% variation that is fairly consistent at all sample positions. Although the variation percentage is similar, the amount of material deposited at sample position 1 is increased compared to all other sample positions. An argon flowrate of 60.0 sccm resulted in a measured thickness of approximately 273 nm while only 259 nm were deposited at 30.0 sccm.

### **Hydrogen and aluminum doped**

A contour plot of hydrogen and aluminum-doped zinc oxide (HAZO) film thickness is shown in Figure 5-4. The vertical axis represents the y-coordinate location under the sputter target and the horizontal axis represents the x-coordinate location. The color assignments denoted in the legend represent thickness equal to or less than their assigned thickness value. The films are deposited for 10 minutes with 10 minutes pre-sputter of the target before opening the shutter to begin the deposition. The RF power is kept at 0.4 kW during deposition with the hydrogen-doped argon working gas flowrate maintained at 40 sccm. The measured film thickness on the 6" x 6" sample is seen to reach a minimum of approximately 160 nm (2,3) and a maximum close to 298 nm (-2,-3). Film thickness is also seen to decrease toward the lower right hand area of the sample (2,-3), where thickness decreases towards 175 nm. These lower areas of film thickness correspond to areas that are positioned closer to the edge of the target and therefore see less sputtered material.

The average thickness of HAZO deposited at four working gas flowrates is pictured in Figure 5-5. The average thickness is plotted on the vertical axis while the sample location under the target is categorized on the horizontal axis. Each working gas flowrate is assigned a marker

style as denoted in the legend. For example, with a hydrogen-doped argon working gas flowrate of 30.0 sccm the average measured thickness at sample position 2 is 228.3 nm. The RF power is kept constant at 0.4 kW for all conditions, with a base pressure of approximately  $2.6 \times 10^{-6}$  Torr. For sputtered HAZO films, a hydrogen-doped argon flowrate of 20.0 sccm seems to provide alternating results between sample positions, with thickness of 225 nm, 261.7 nm, 205 nm, and 245 nm reported for sample positions 1 through 4, respectively. The thickness at all other flowrates is much more consistent, with 40.0 sccm hydrogen-doped argon consistently providing the most deposition and 50.0 sccm the least at all four sample positions.

### **Comparison of AZO and HAZO**

A comparison of AZO and HAZO average film thickness at each of the four sample positions under the target is shown in Figure 5-6. The average thickness is graphed on the vertical axis and the horizontal axis categorizes the deposited films by sample location under the target. Each working gas is assigned a line type and each working gas flowrate is assigned a marker style as denoted in the legend. For example, hydrogen-doped argon working gas is assigned a dashed line, and 30.0 sccm flowrate of working gas is assigned a square marker, with a 228.3 nm average HAZO thickness at sample position 2. The RF power is kept constant at 0.4 kW for all conditions, with a base pressure of approximately  $2.6 \times 10^{-6}$  Torr. In general, the average film thickness is highest at sample position 1 for both types of working gas. For hydrogen-doped argon working gas the maximum deposition occurs at 40.0 sccm, with thickness at 50.0 sccm decreasing below that of 30.0 sccm. This is not seen for the standard argon working gas used to deposit AZO films. The addition of the hydrogen changes the plasma characteristics and drops the sputter deposition rate at some point between 40.0 sccm and 50.0 sccm.

## **Electrical Characteristics**

The electrical characteristics of Al:ZnO and H-Al:ZnO sputter deposited films is determined using an Alessi four-point probe coupled with a Keithley Model 181 Nanovoltmeter. Measurements are taken at eight equally spaced locations across the sample surface. The minimum and maximum sheet resistance values are reported rather than the average, which can be heavily influenced by outliers. Unless otherwise stated, the target is conditioned with a pre-sputter before opening the shutter to start deposition on the SLG substrates. The effect of flowrate and positioning under the target is analyzed for AZO and HAZO sputter deposited films. The base pressure of the sputter deposition chamber is kept constant for all experiments, on the order of  $2.6 \times 10^{-6}$  Torr. Films are sputtered from the Al<sub>2</sub>O<sub>3</sub>-doped zinc oxide target both for AZO and HAZO.

### **Aluminum doped**

A contour plot of aluminum-doped zinc oxide (AZO) sheet resistance is shown in Figure 5-7. The film is deposited for 10 minutes with 10 minutes pre-sputter of the target before opening the shutter to begin the deposition. The vertical axis represents the y-coordinate location under the sputter target and the horizontal axis represents the x-coordinate location. The color assignments denoted in the legend represent sheet resistance equal to or less than their assigned sheet resistance value. The RF power is kept at 0.4 kW during deposition with the argon working gas flowrate maintained at 40.0 sccm. The measured film sheet resistance on the 6" x 6" sample is seen to maintain a very low value less than 1000  $\Omega$ /sq in the central location of the sample, with a large area, between (-2,-1.5) and (0, -1.5), reporting sheet resistance values less than 300  $\Omega$ /sq. A x-coordinate values of 2 to 2.5 a large dramatic increase in sheet resistance is seen, with values reaching 13,000  $\Omega$ /sq at (2.5, 2). As seen with film thickness,

these areas are positioned closer to the edge of the sputter target and therefore receive less deposition.

The minimum sheet resistance of AZO deposited at four working gas flowrates is shown in Figure 5-8. The vertical axis plots the minimum sheet resistance while the horizontal axis categorizes the deposited AZO by sample location under the target, as specified in Figure 5-2. Each working gas flowrate is assigned a marker style as denoted in the legend. For example, with an argon working gas flowrate of 30.0 sccm the minimum sheet resistance at sample position 2 is 140  $\Omega$ /sq. The RF power is kept constant at 0.4 kW for all conditions, with a base pressure of approximately  $2.6 \times 10^{-6}$  Torr. The flowrate of argon working gas is adjusted from 30.0 sccm to 60.0 sccm in 10.0 sccm increments. It can be seen that the minimum sheet resistance is a function of working gas flowrate. The minimum argon flowrate results in the highest sheet resistance values at all sample positions, reaching 341  $\Omega$ /sq at sample position 4. As the argon flowrate increases, the minimum sheet resistance decreases, with an argon flowrate of 60.0 sccm achieving the lowest sheet resistance values at all positions, with position 2 providing the lowest of all sheet resistance, 98.2  $\Omega$ /sq.

Figure 5-9 shows the maximum sheet resistance of AZO deposited at four working gas flowrates. The maximum sheet resistance is plotted on the vertical axis and the sample location under the target is categorized on the horizontal axis. Each working gas flowrate is assigned a marker style as denoted in the legend. For example, a maximum sheet resistance of 2240  $\Omega$ /sq is measured for 30.0 sccm argon flowrate at sample position 1. The maximum sheet resistance follows the same trend as the minimum sheet resistance, where increasing working gas flowrate results in decreased sheet resistance. Sample positions 1 and 4 exhibit maximum sheet resistance values that are 500% and 800%, respectively, of those measured at sample positions 2 and 3.

Overall, a working gas flowrate of 60.0 sccm seems to provide the optimal sheet resistance conditions with an average maximum value of 269.3  $\Omega/\text{sq}$  and a minimum value of 106.1  $\Omega/\text{sq}$  over sample positions 1 through 3.

### **Hydrogen and aluminum doped**

A contour plot of hydrogen and aluminum-doped zinc oxide (HAZO) sheet resistance is shown in Figure 5-10. The film is deposited for 10 minutes with 10 minutes pre-sputter of the target before opening the shutter to begin film deposition. The vertical axis represents the y-coordinate location under the sputter target and the horizontal axis represents the x-coordinate location. The color assignments denoted in the legend represent sheet resistance equal to or less than their assigned sheet resistance value. The RF power is kept at 0.4 kW during deposition with the hydrogen-doped argon working gas flowrate maintained at 40.0 sccm. The measured sheet resistance on the 6" x 6" substrate is very similar to AZO, as a large majority of the sample exhibits relatively uniform and low sheet resistance. The sheet resistance achieves a minimum value at the (-2, -2) location, and maximums at (2, -2) and (2, 2), which is similar to AZO. However, HAZO sheet resistance stays low at the (2, 0) location, which is not seen in the case of AZO.

The minimum sheet resistance of HAZO deposited at four working gas flowrates is shown in Figure 5-11. The vertical axis plots the minimum sheet resistance while the horizontal axis categorizes the deposited AZO by sample location under the target, as specified in Figure 5-2. Each working gas flowrate is assigned a marker style as denoted in the legend. For example, with a hydrogen-doped argon working gas flowrate of 30.0 sccm the minimum sheet resistance at sample position 1 is 110  $\Omega/\text{sq}$ . The RF power is kept constant at 0.4 kW for all conditions, with a base pressure of approximately  $2.6 \times 10^{-6}$  Torr. The flowrate of hydrogen-doped argon working gas is adjusted from 20.0 sccm to 50.0 sccm in 10.0 sccm increments. As is the case

with AZO, it appears that the minimum sheet resistance of HAZO films is a function of the working gas flowrate. The sheet resistance decreases with increasing working gas flowrate from 20.0 sccm and reaches a minimum at 40.0 sccm, with max and min values of 136  $\Omega$ /sq and 95.1  $\Omega$ /sq at sample position 2, respectively. A slight increase in sheet resistance is then seen upon increasing the hydrogen-doped argon working gas flowrate from 40.0 sccm to 50.0 sccm. For sample position 2, the minimum sheet resistance increase from 95.1  $\Omega$ /sq to 101  $\Omega$ /sq when increasing from 40.0 sccm to 50.0 sccm. Figure 5-12 portrays the maximum sheet resistance of HAZO deposited at four working gas flowrates. The maximum sheet resistance is plotted on the vertical axis and the sample location under the target is categorized on the horizontal axis. Each working gas flowrate is assigned a marker style as denoted in the legend. For example, a maximum sheet resistance of 1440  $\Omega$ /sq is measured for 30.0 sccm hydrogen-doped argon flowrate at sample position 4. The maximum sheet resistance of HAZO films follows a similar trend where increasing working gas flowrate results in diminished sheet resistance. The only exception to this is 20.0 sccm which reports values almost identical to 30.0 sccm at all sample position except position 4, where a much reduced sheet resistance of 793  $\Omega$ /sq is measured compared to 1440  $\Omega$ /sq at 20.0 sccm hydrogen-doped argon flowrate. The maximum sheet resistance at sample positions 2 and 3 is on average three to four times smaller than the sheet resistance at positions 1 and 4. These positions exhibit a very tight spread for the entire range of working gas flowrate, varying from 137  $\Omega$ /sq to 227  $\Omega$ /sq and 217  $\Omega$ /sq to 367  $\Omega$ /sq at sample positions 2 and 3, respectively. Sample positions 1 and 4 report ranges of 691  $\Omega$ /sq and 647  $\Omega$ /sq, respectively. Overall, working gas flowrates of 40.0 sccm and 50.0 sccm hydrogen-doped argon appears to provide to provide optimal sheet resistance with an minimum sheet

resistance in the range of 95.1  $\Omega/\text{sq}$  to 101  $\Omega/\text{sq}$  and maximum values of 183  $\Omega/\text{sq}$  and 136  $\Omega/\text{sq}$  at sample position 2.

### **Comparison of AZO and HAZO**

A comparison of minimum sheet resistance for AZO and HAZO sputter deposited films is shown in Figure 5-13. The minimum sheet resistance is graphed on the vertical axis and the horizontal axis categorizes the deposited films by sample location under the target. Each working gas is assigned a line type and each working gas flowrate is assigned a marker style as denoted in the legend. For example, a hydrogen-doped argon working gas is assigned a dashed line, and 30.0 sccm flowrate of working gas is assigned a square marker, with a 103  $\Omega/\text{sq}$  minimum sheet resistance measured at sample position 2. The RF power is kept constant at 0.4 kW for all conditions, with a base pressure of approximately  $2.6 \times 10^{-6}$  Torr. The overall distribution of minimum sheet resistance is much tighter across sample positions for HAZO films than those films deposited with argon working gas. In particular, the minimum sheet resistance at 30.0 sccm Ar is markedly higher than other argon working gas flowrates. A similar comparison of maximum sheet resistance for AZO and HAZO films can be seen in Figure 5-14. The maximum sheet resistance is plotted on the vertical axis and the horizontal axis categorizes the deposited films by sample location under the target. Each working gas is assigned a line type and each working gas flowrate is assigned a marker style as denoted in the legend. For example, an argon working gas is assigned a solid line, and 40.0 sccm of working gas is assigned a triangle marker, with a 1600  $\Omega/\text{sq}$  maximum sheet resistance measured at sample position 1. A decrease in the maximum sheet resistance is seen with an increase in the working gas flowrate. Also, the addition of hydrogen to the working gas is shown to decrease the sheet resistance at each flowrate and sample position. As seen before, sample positions 2 and 3 appear to produce the

highest quality films as the sheet resistance variation between working gas flowrates is kept to a minimum.

Film resistivity is calculated with the sheet resistance data using the average measured thickness reported earlier this chapter. Figure 5-15 shows the minimum resistivity of sputter deposited AZO and HAZO films. The minimum resistivity is graphed on the vertical axis and the horizontal axis categorizes the deposited films by sample location. Each working gas is assigned a line type and each working gas flowrate is assigned a marker style as denoted in the legend. For example, a hydrogen-doped argon working gas is assigned a dashed line, and 50.0 sccm flowrate of working gas is assigned a circle marker, with a  $2.47 \times 10^{-3} \Omega \cdot \text{cm}$  minimum resistivity measured at sample position 1. In general, sample position 2 achieves good resistivity a number of flowrate and working gas conditions. A minimum resistance of  $2.28 \times 10^{-3} \Omega \cdot \text{cm}$  is achieved at sample position 2 with a 50.0 sccm flowrate of hydrogen-doped argon working gas.

### **Optical Characteristics**

The optical transmission of AZO and HAZO thin films is studied using UV/Vis spectroscopy in the 300 nm to 900 nm range. The transmittance spectra are measured without the use of an integrating sphere. A bare glass substrate with no deposited ZnO is measured in order to factor out transmission loss from the substrate itself. The average transmission between 400 nm and 800 nm of AZO and HAZO films before and after thermal treatment is presented.

The effects of working gas flowrate and sample position under the target on the average transmission of AZO and HAZO films are shown in Figure 5-16. The average transmission is graphed on the vertical axis, and the horizontal axis categorizes the films by sample position under the target. Each working gas flowrate is assigned a marker color and shape, as denoted in the legend. Filled-in markers correspond to argon working gas while empty markers correspond to hydrogen-doped argon working gas. For example, the average transmittance of HAZO

deposited at 40.0 sccm in sample position 1 is 82.3%. For HAZO, the highest transmission is observed at 50.0 sccm hydrogen-doped argon except for sample position 2 where 20.0 sccm results in 86.4% transmission. At all other sample positions 20.0 sccm only produces the second highest transmission. The variation in transmission is much smaller for AZO films., where transmission is observed to increase with working gas flowrate. The highest transmittance is measured at sample position 2 for both AZO and HAZO is 86.4% and 83.7%, respectively.

### Figure of Merit

High transmission and low electrical resistivity are two parameters that are extremely important to transparent conductors. In order to evaluate the quality of an optoelectronic film, a figure of merit performance parameter is calculated which is based off the ratio of film resistivity to the visible transmission. The figure of merit is defined as

$$\text{FOM} = -\frac{1}{\rho \ln(T)} \quad (5-1)$$

where  $\rho$  is the film resistivity and  $T$  is the average transmission in the 400 nm to 800 nm range [111-113]. A larger figure of merit (FOM) value indicates superior optoelectronic film properties.

The effect of working gas flowrate and sample position under the target on the figure of merit of AZO and HAZO is shown in Figure 5-17. The vertical axis plots the figure of merit and the horizontal axis categorizes the films by sample position. Each working gas flowrate is assigned a marker color and shape, as denoted in the legend. Filled-in markers correspond to argon working gas while empty markers correspond to hydrogen-doped argon working gas. For example, the FOM of AZO deposited at 30.0 sccm in sample position 3 is  $1234 \Omega^{-1}\text{cm}^{-1}$ . The figure of merit is seen to be the highest for the films deposited at sample position 2. This is mostly a result of the superior resistivity exhibited by the films deposited in that sample location.

Sample positions 1 and 3 produce similar results with sample position 4 exhibiting the worst FOM values. The figure of merit increases with increasing hydrogen-doped argon working gas flowrate. This same trend is seen for AZO films, with 60.0 sccm of argon working gas produced the highest figure of merit at each sample position, and 30.0 sccm the lowest. Deposition at 50.0 sccm and 60.0 sccm at sample position 2 produces HAZO and AZO, respectively, with superior optoelectronic properties compared to lower flowrates or sample locations under the target.

### **Conclusions**

The sputter deposition of aluminum-doped and hydrogen-aluminum-doped zinc oxide is carried out via rf magnetron sputtering. The possibility of deposition at a higher than usual base pressure is studied in hopes of achieving the potential for increased industrial throughput while maintaining or improving on film properties. Both AZO and HAZO films are sputtered at 0.4 kW and a base pressure of  $2.6 \times 10^{-6}$  Torr. The effect of gas working, which effects the working pressure, is also studied. The average AZO film thickness is seen to range from 235.0 nm to 273.3 nm and 225.0 nm to 265.0 nm for HAZO, depending on the positioning under the target. Sheet resistance is also affected by sample positioning and working gas flowrate. The minimum AZO resistivity of  $2.37 \times 10^{-3} \Omega \cdot \text{cm}$  is achieved at 60.0 sccm argon, while the minimum HAZO resistivity of  $2.28 \times 10^{-3} \Omega \cdot \text{cm}$  is achieved at 50.0 sccm hydrogen-doped argon. Transmission of AZO and HAZO films vary between 81.0% and 86.4% depending on working gas flowrate and sample positioning. The figure of merit calculation is used for determining the optoelectronic superiority of the deposited films. The best AZO and HAZO films deposited exhibit FOM values of  $2376 \Omega^{-1} \text{cm}^{-1}$  and  $2672 \Omega^{-1} \text{cm}^{-1}$ , respectively.

Table 5-1. Average thickness of AZO films at flowrates of 30.0, 40.0, 50.0, and 60.0 sccm.

	Position 1 Thickness (nm)	Position 2 Thickness (nm)	Position 3 Thickness (nm)	Position 4 Thickness (nm)
30.0 sccm Ar	258.33	235.00	240.00	238.33
40.0 sccm Ar	258.33	240.00	236.67	241.67
50.0 sccm Ar	261.67	236.67	236.67	241.67
60.0 sccm Ar	273.33	241.67	236.67	246.67

Table 5-2. Average thickness of HAZO films at flowrates of 20.0, 30.0, 40.0, and 50.0 sccm.

	Position 1 Thickness (nm)	Position 2 Thickness (nm)	Position 3 Thickness (nm)	Position 4 Thickness (nm)
20.0 sccm Ar+H <sub>2</sub>	225.00	261.67	205.00	245.00
30.0 sccm Ar+H <sub>2</sub>	258.33	228.33	230.00	235.00
40.0 sccm Ar+H <sub>2</sub>	265.00	246.67	238.33	248.33
50.0 sccm Ar+H <sub>2</sub>	248.33	225.00	220.00	230.00

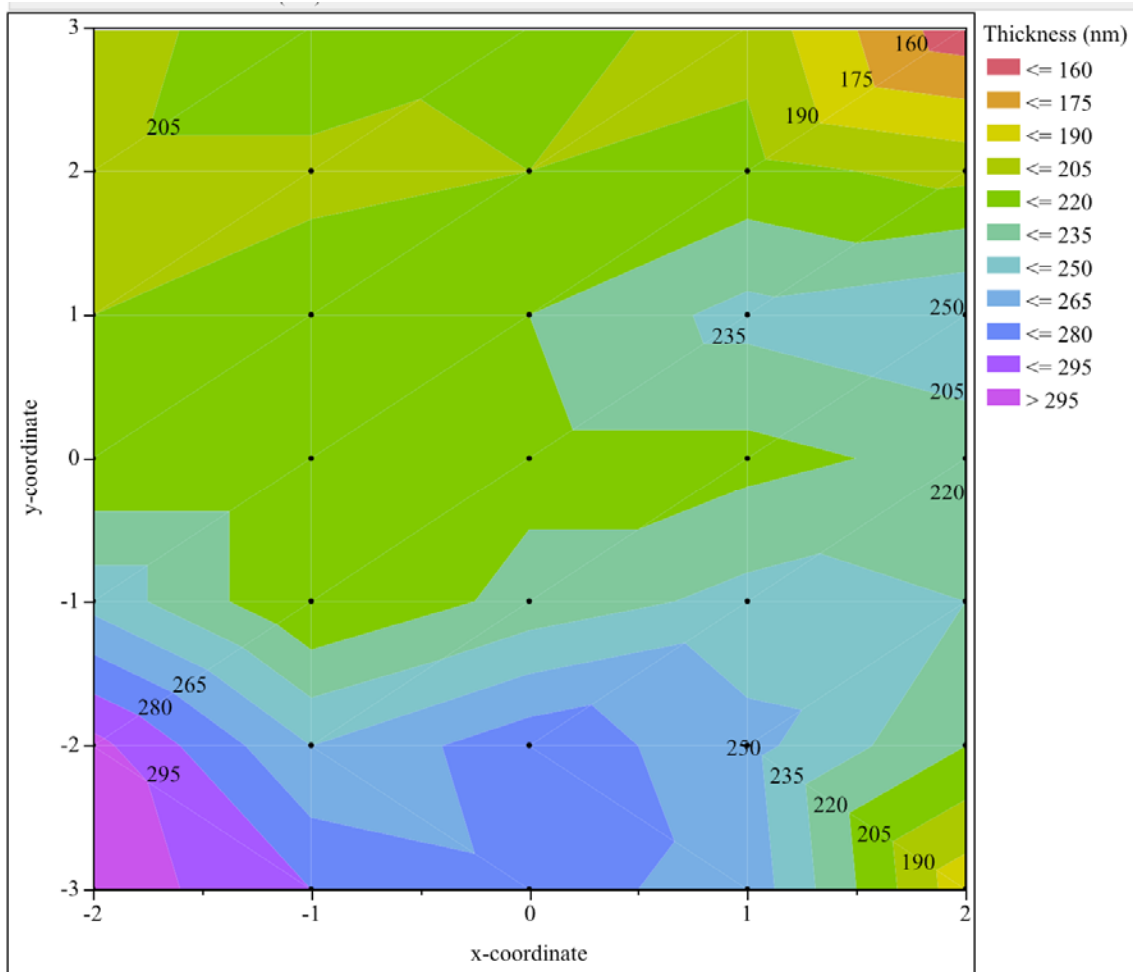


Figure 5-1. Thickness contour plot of AZO film deposited at 0.4 kW with 40 sccm argon working gas flowrate.

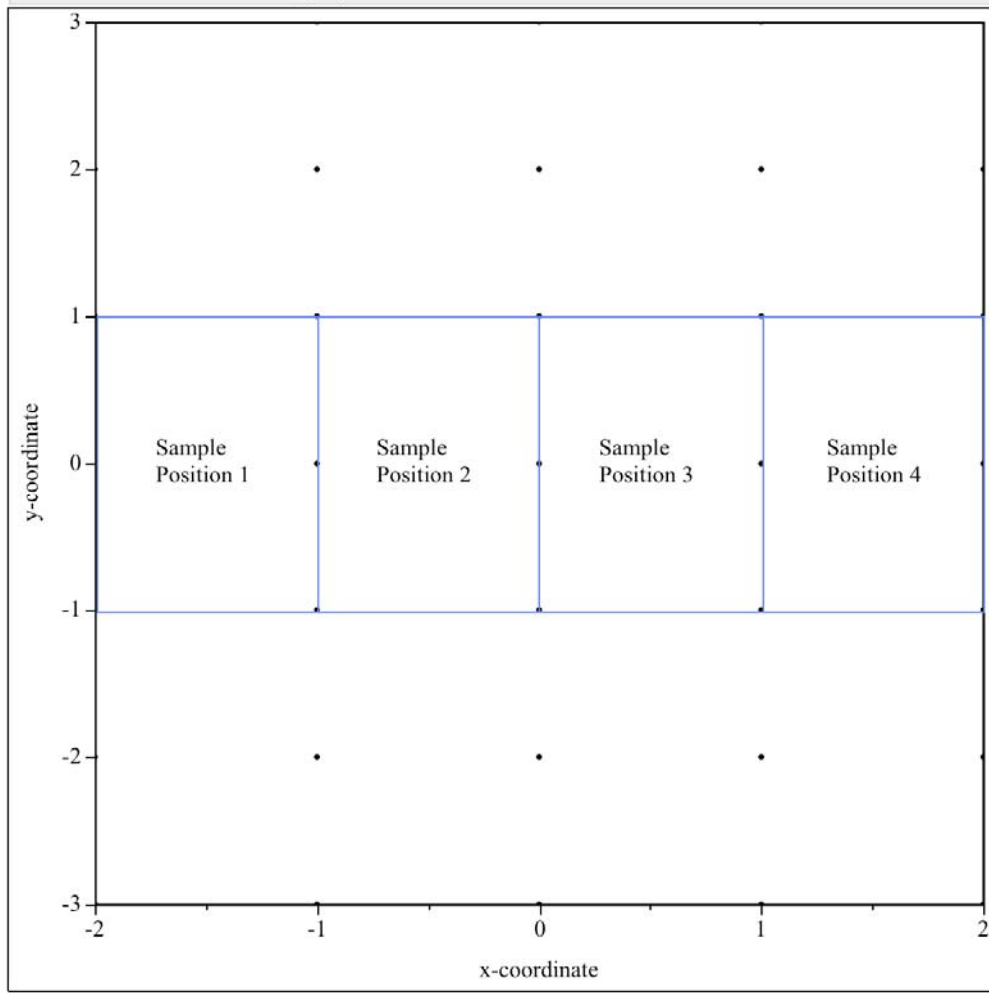


Figure 5-2. Four defined sample positions under the  $\text{Al}_2\text{O}_3$ -doped zinc oxide target.

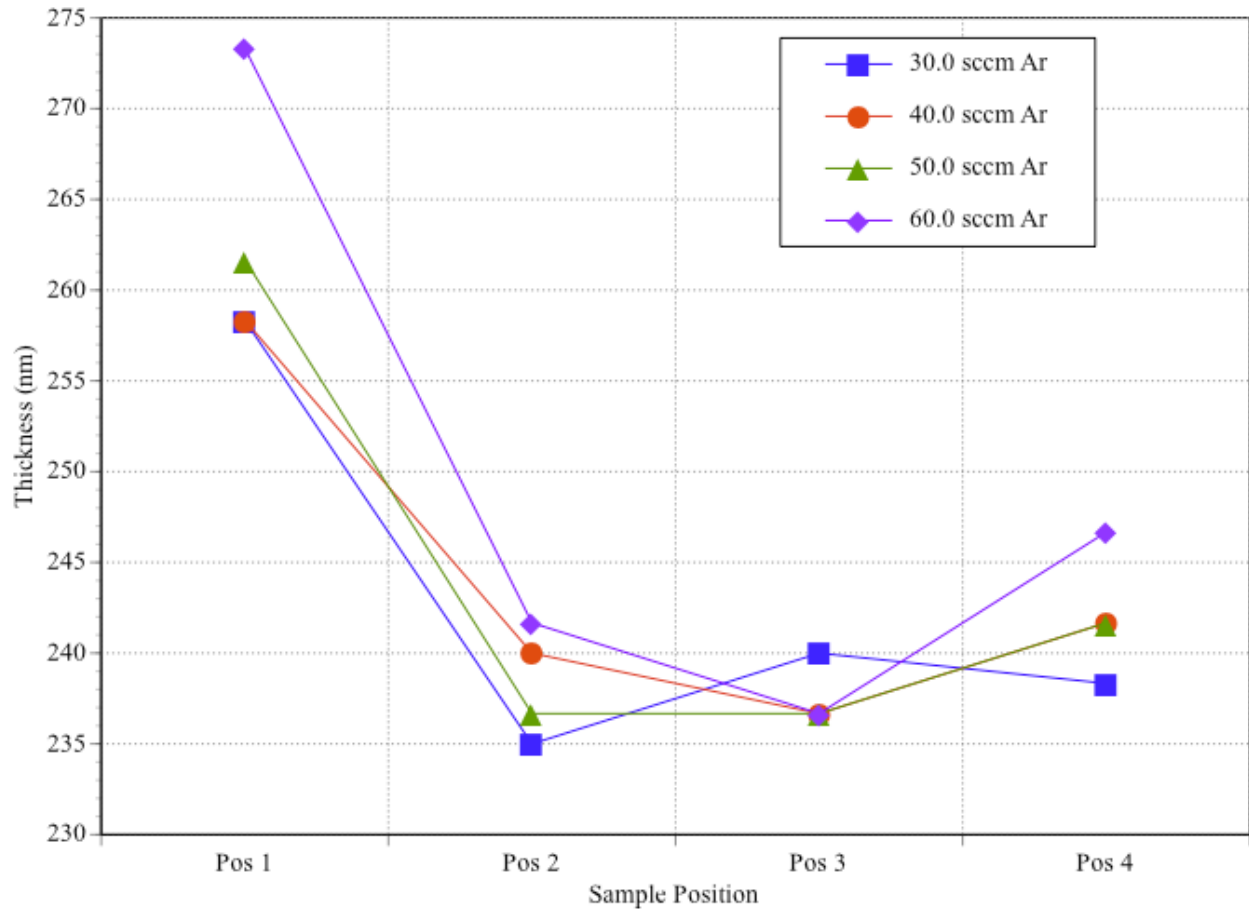


Figure 5-3. Average AZO film thickness deposited at 0.4 kW with working gas flowrates of 30.0, 40.0, 50.0, and 60.0 sccm argon.

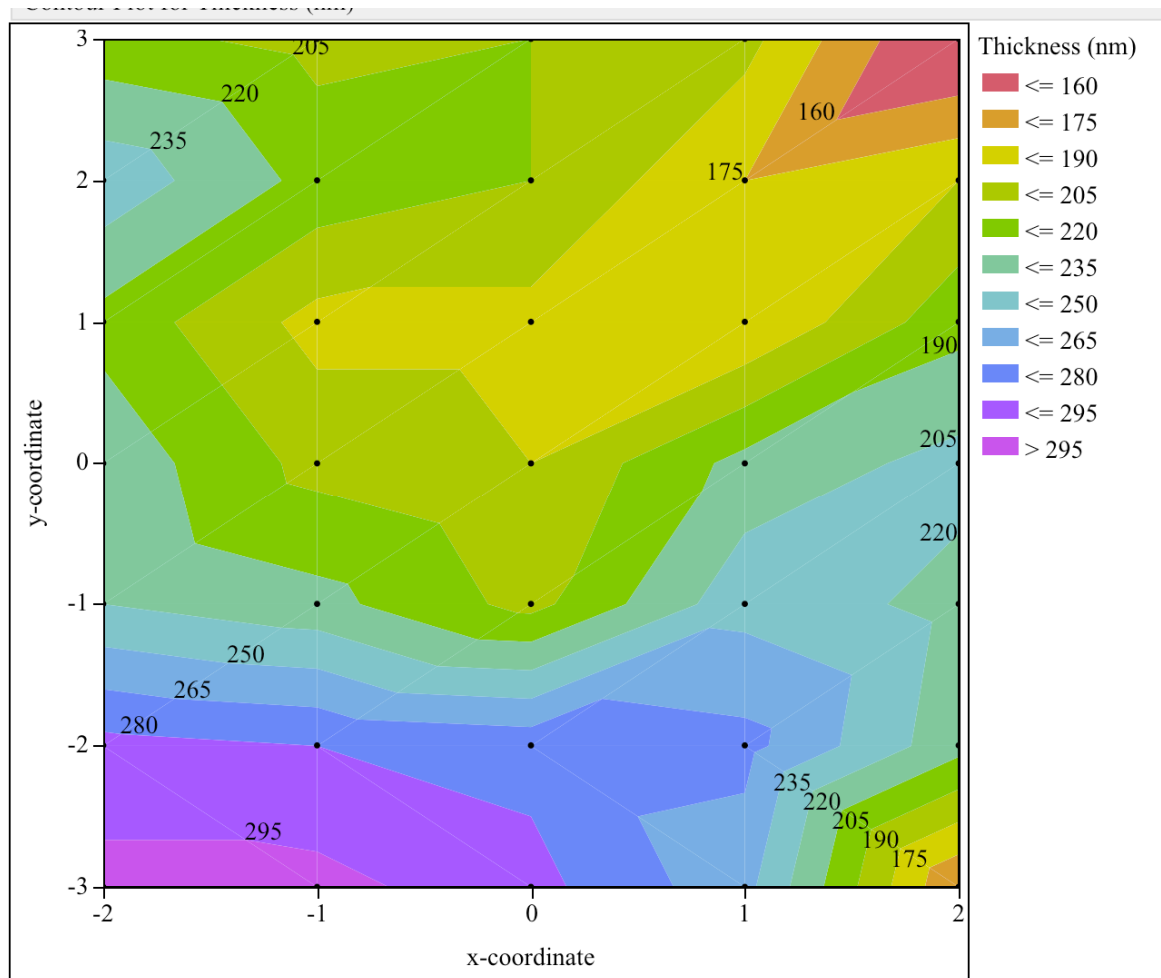


Figure 5-4. Thickness contour plot of HAZO film deposited at 0.4 kW with 40 sccm hydrogen-doped argon working gas flowrate.

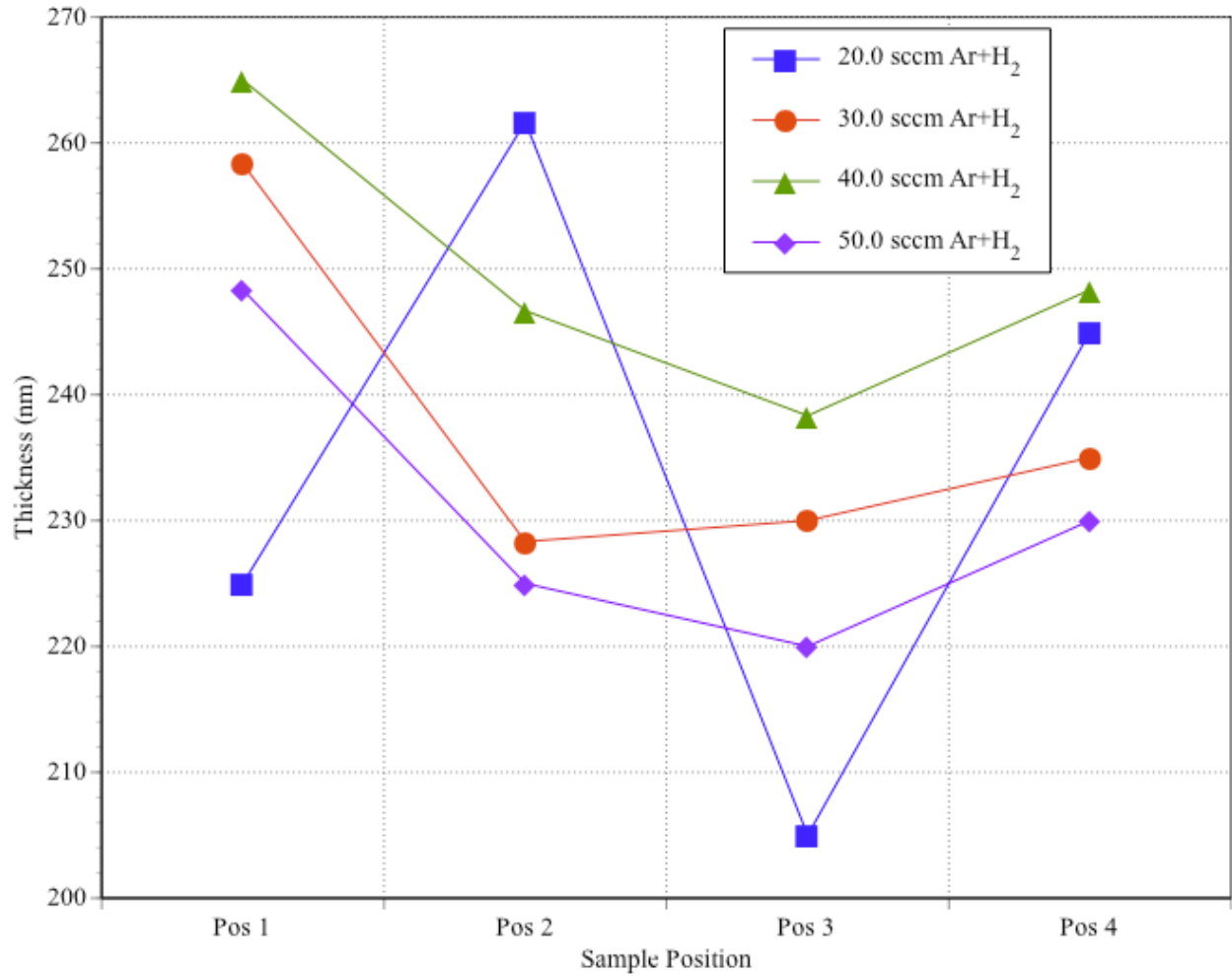


Figure 5-5. Average HAZO film thickness deposited at 0.4 kW with working gas flowrates of 20.0, 30.0, 40.0, and 50.0 sccm hydrogen-doped argon.

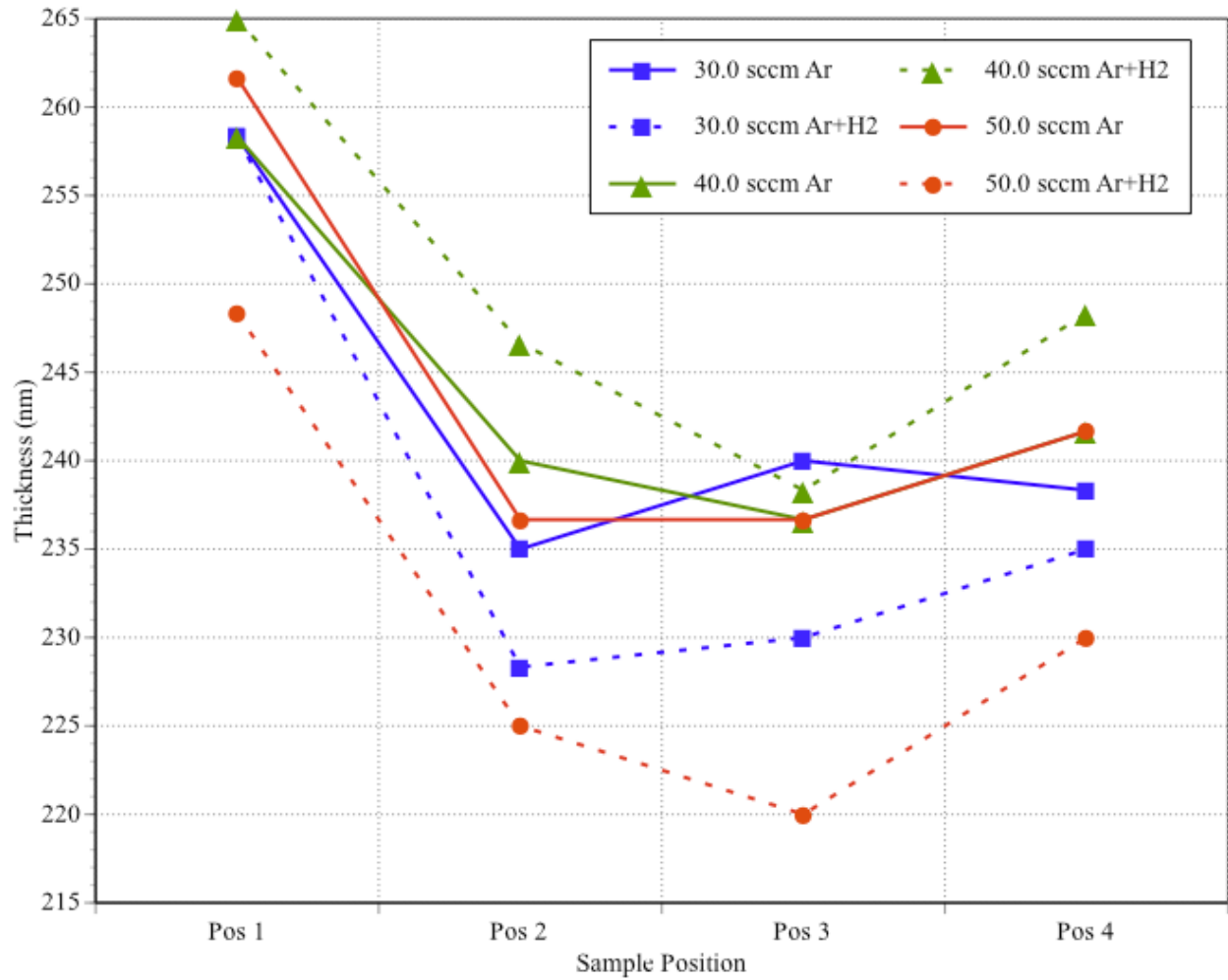


Figure 5-6. Comparison of AZO and HAZO average film thickness as a function of sample position and working gas composition and flowrate.

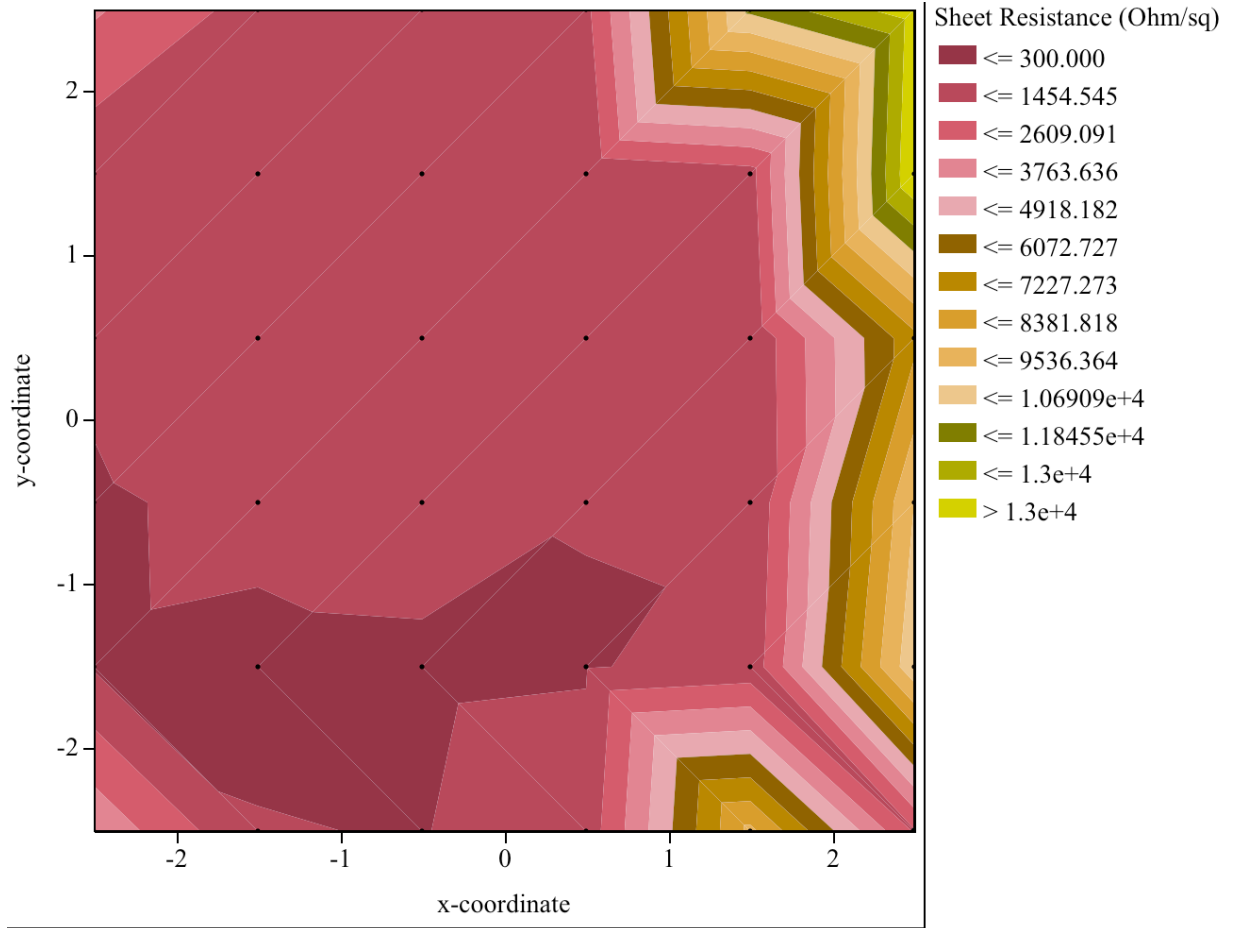


Figure 5-7. Sheet resistance contour plot of AZO film deposited at 0.4 kW with 40 sccm argon working gas flowrate.

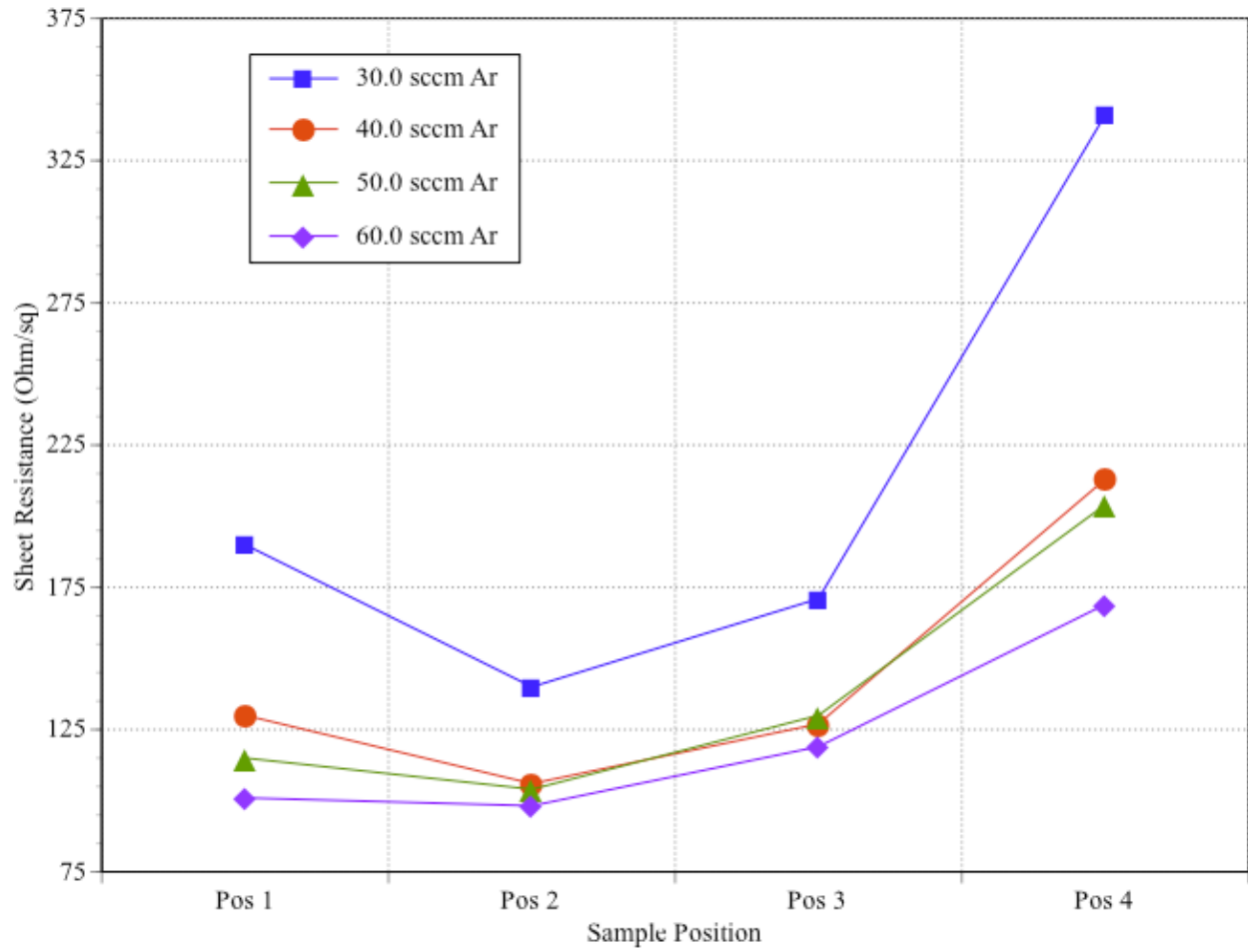


Figure 5-8. Minimum AZO sheet resistance deposited at 0.4 kW with working gas flowrates of 30.0, 40.0, 50.0, and 60.0 sccm argon.

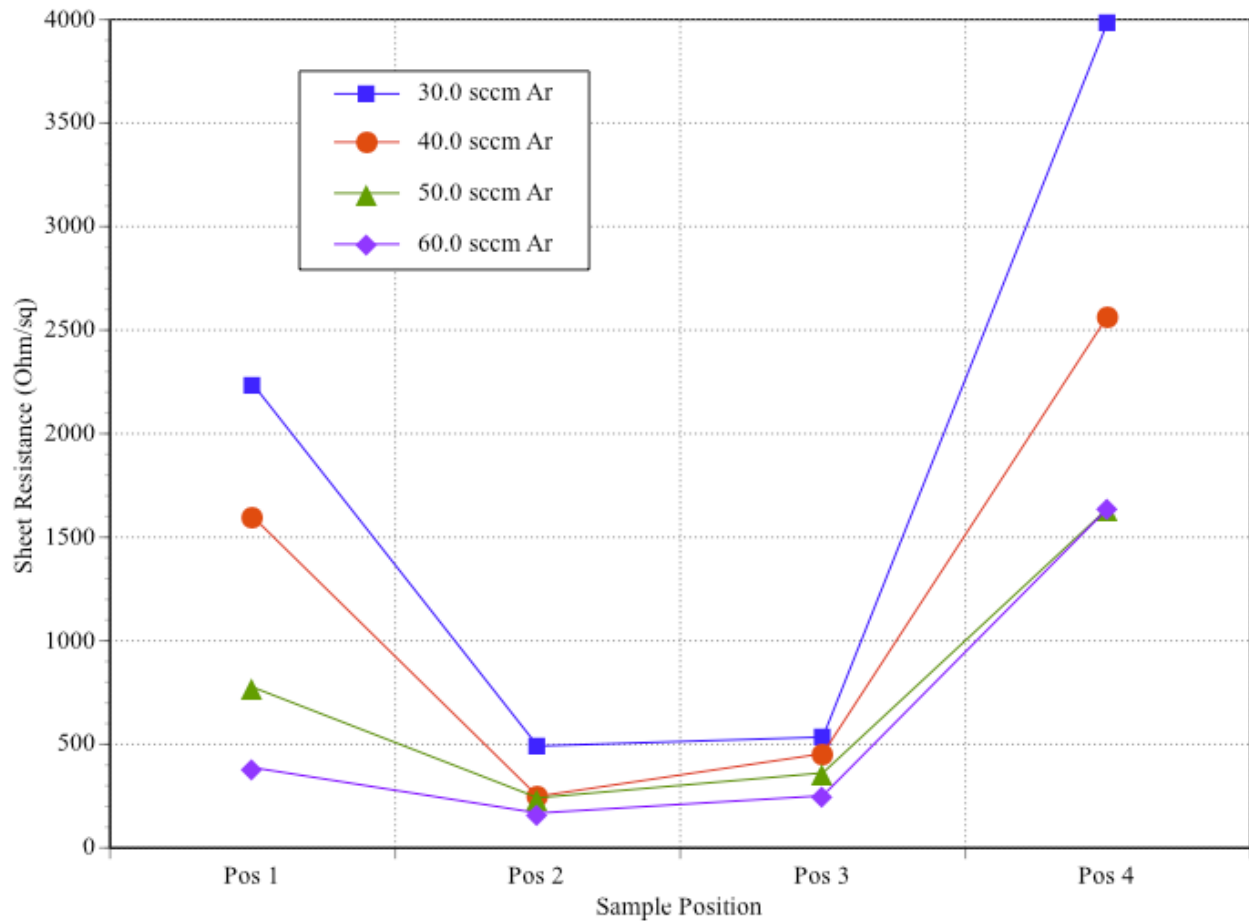


Figure 5-9. Maximum AZO sheet resistance deposited at 0.4 kW with working gas flowrates of 30.0, 40.0, 50.0, and 60.0 sccm argon.

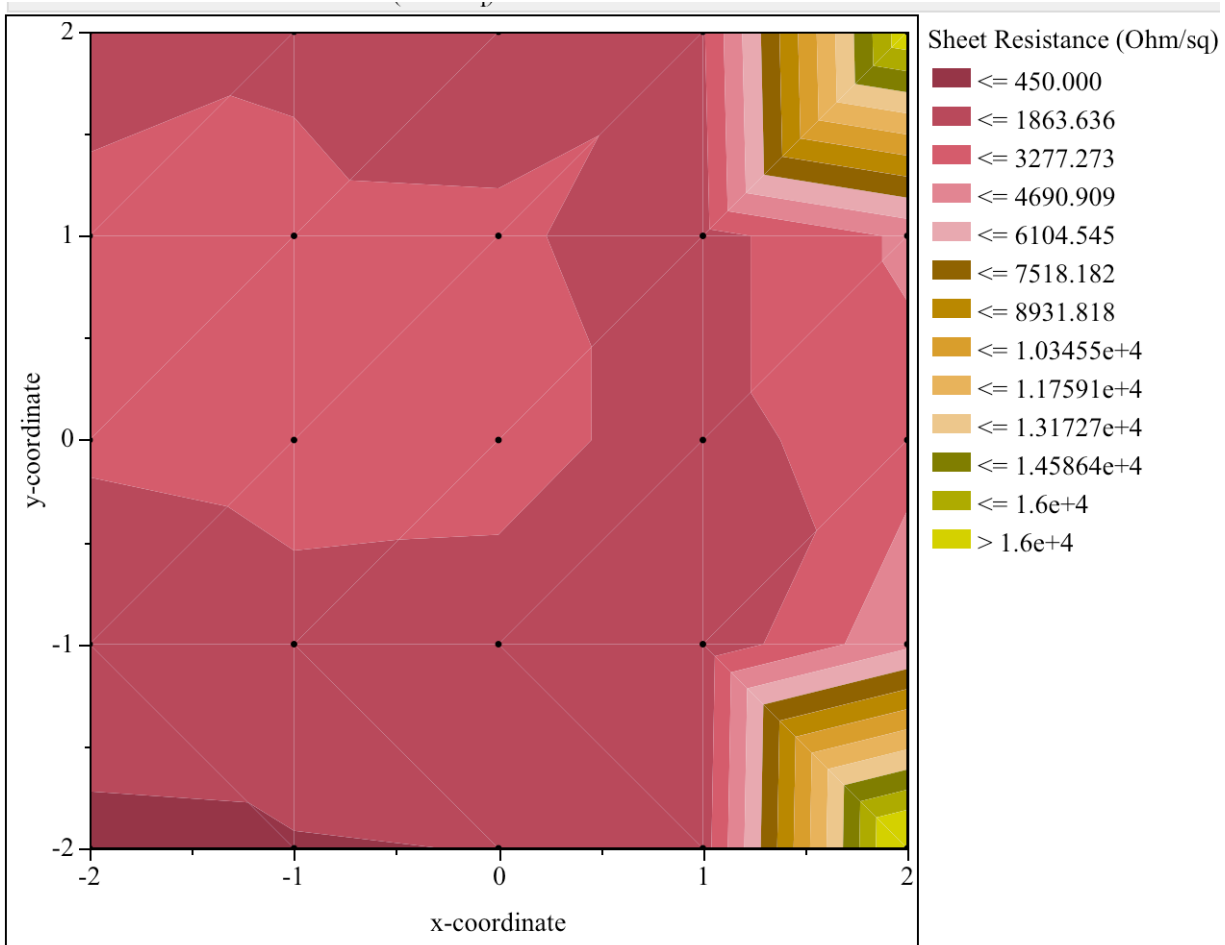


Figure 5-10. Sheet resistance contour plot of HAZO film deposited at 0.4 kW with 40.0 sccm hydrogen-doped argon working gas flowrate.

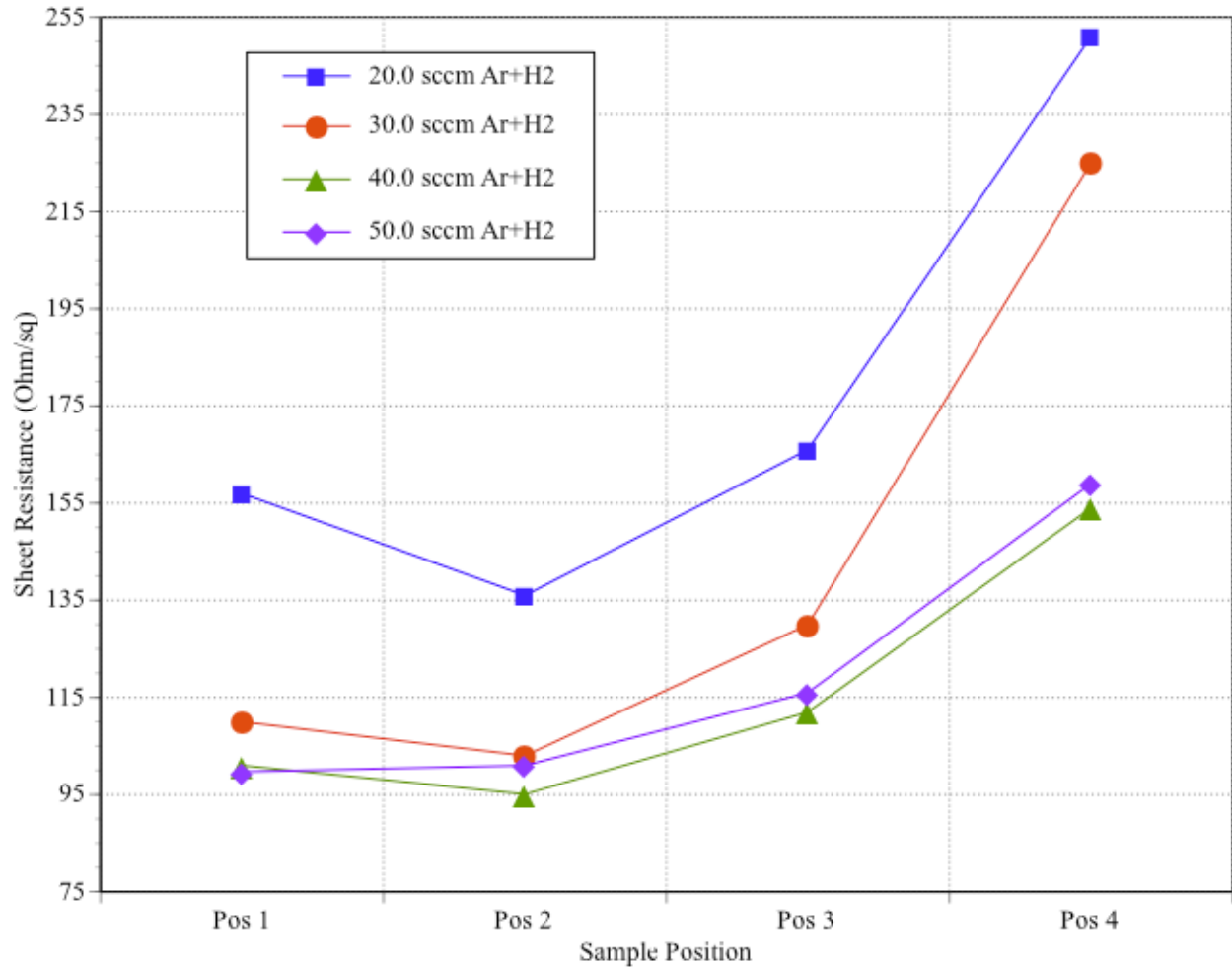


Figure 5-11. Minimum HAZO sheet resistance deposited at 0.4 kW with working gas flowrates of 20.0, 30.0, 40.0, and 50.0 sccm hydrogen-doped argon.

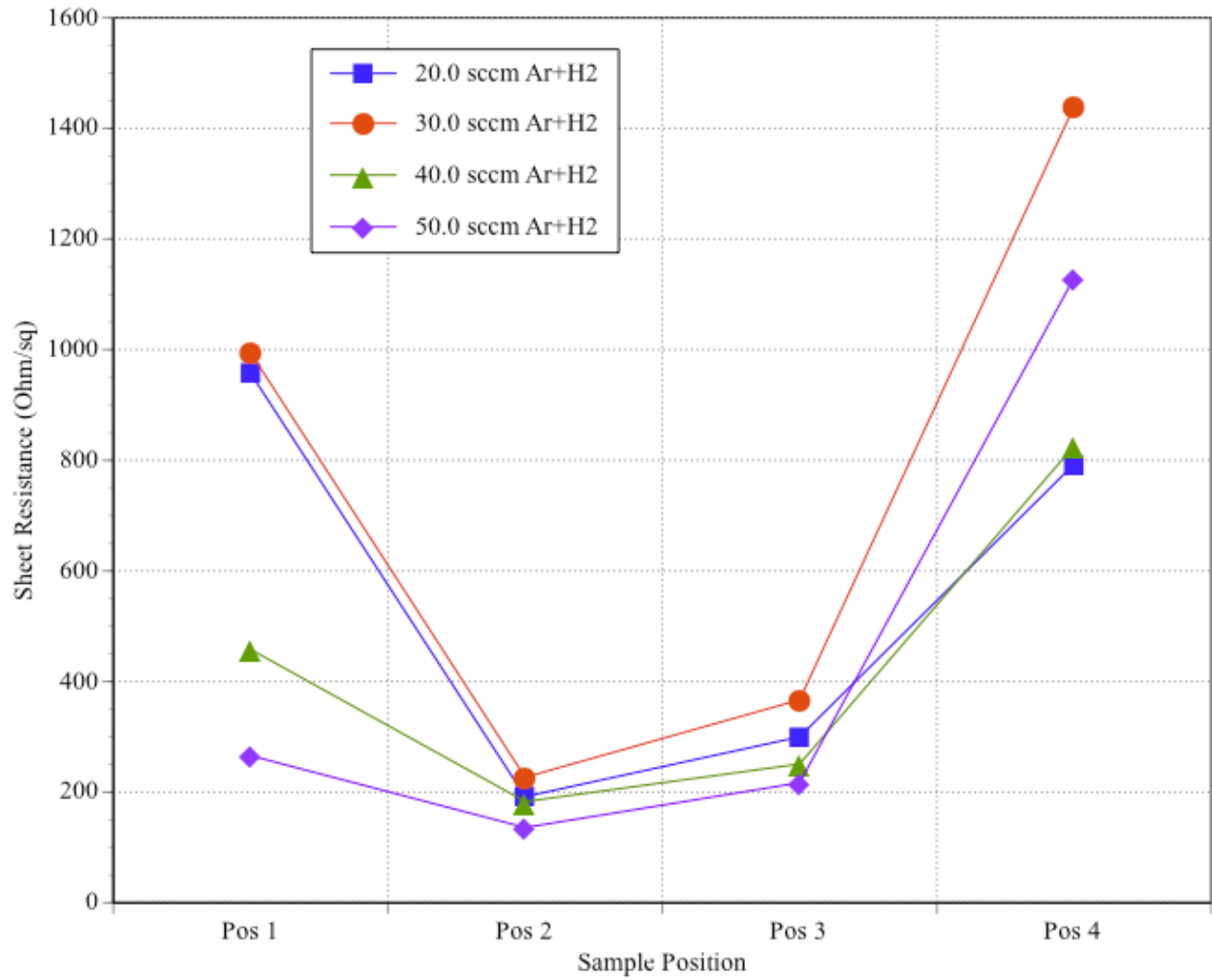


Figure 5-12. Maximum HAZO sheet resistance deposited at 0.4 kW with working gas flowrates of 20.0, 30.0, 40.0, and 50.0 sccm hydrogen-doped argon.

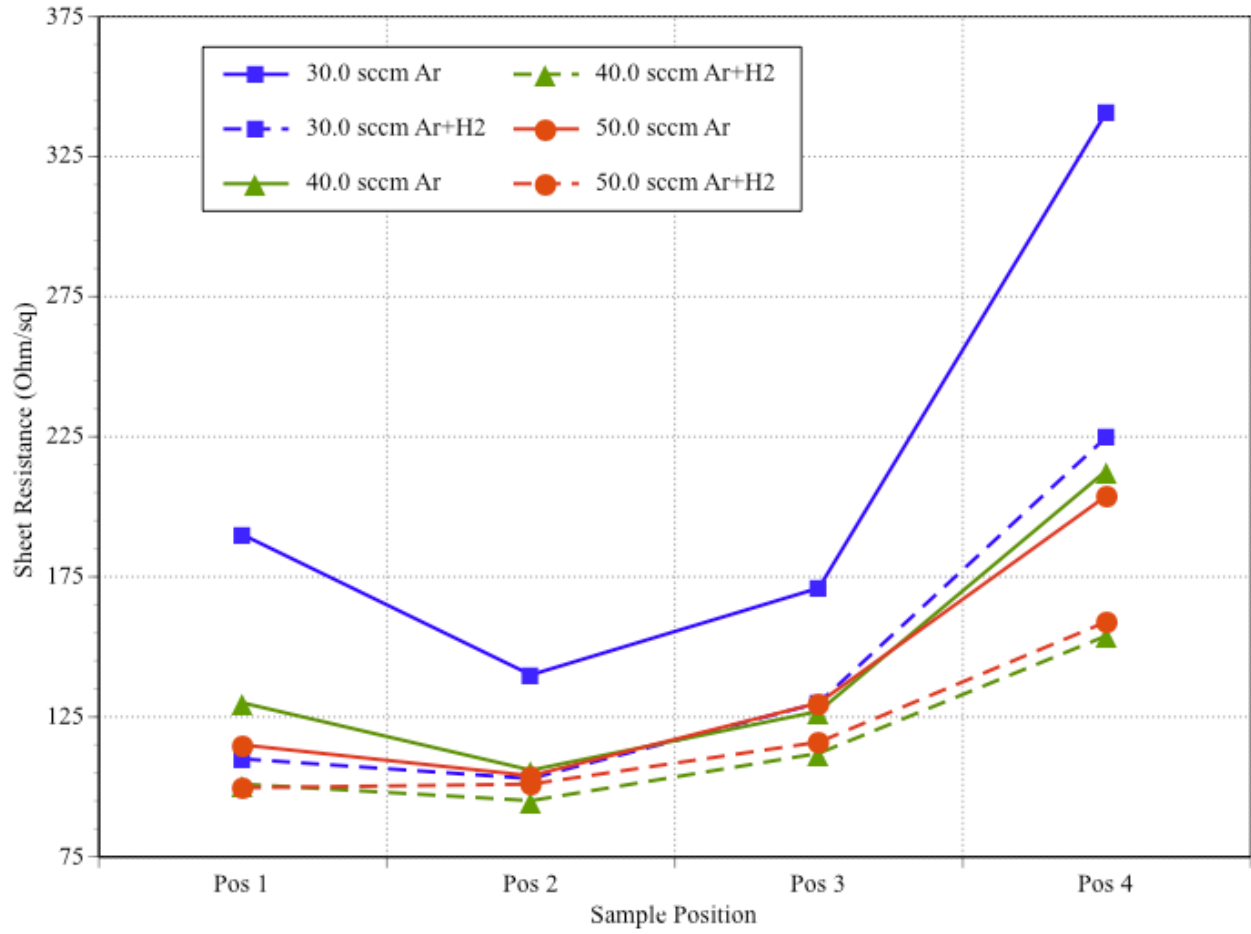


Figure 5-13. Minimum sheet resistance of AZO and HAZO films deposited at 0.4 kW with working gas flowrates of 30.0, 40.0, and 50.0 sccm.

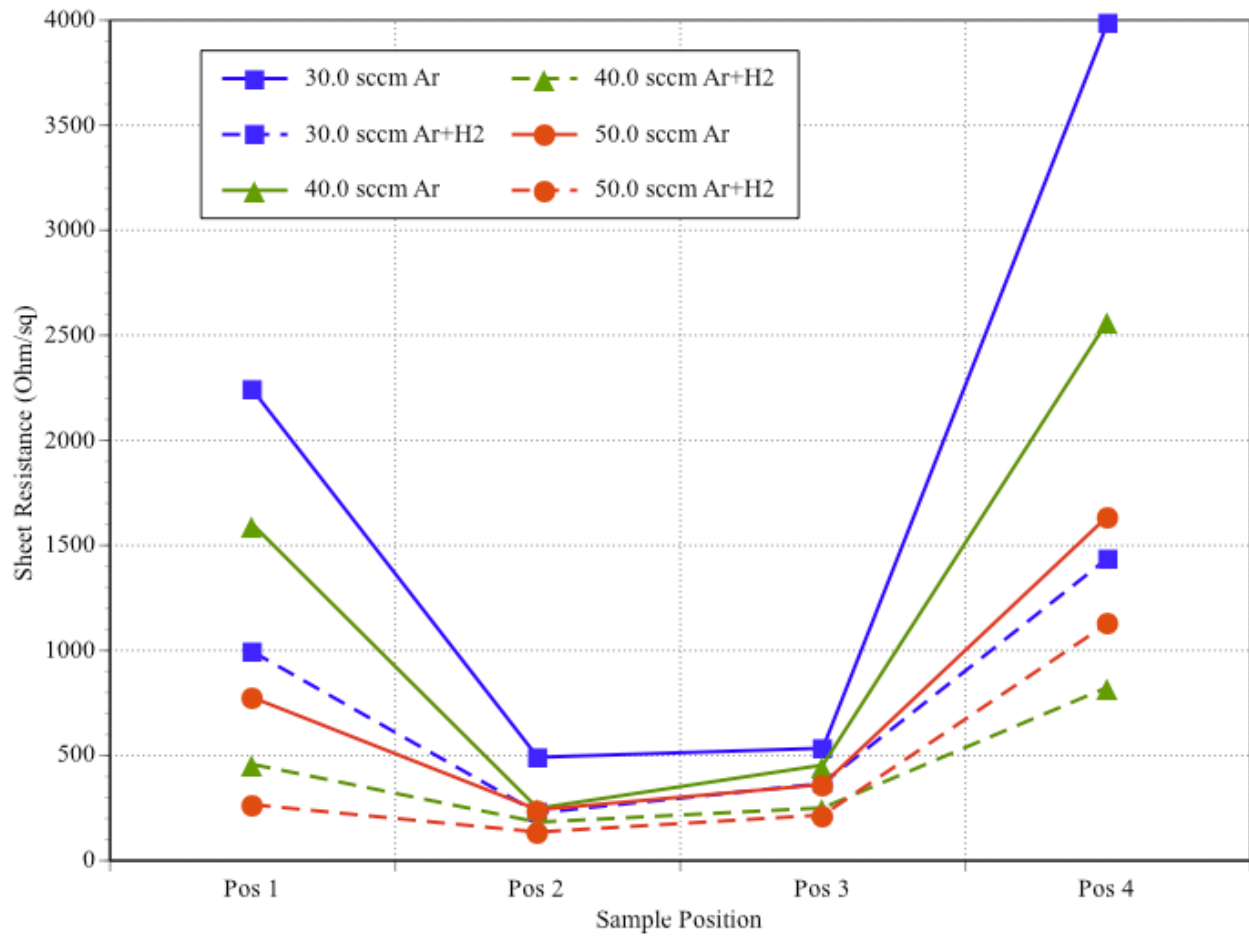


Figure 5-14. Maximum sheet resistance of AZO and HAZO films deposited at 0.4 kW with working gas flowrates of 30.0, 40.0, and 50.0 sccm.

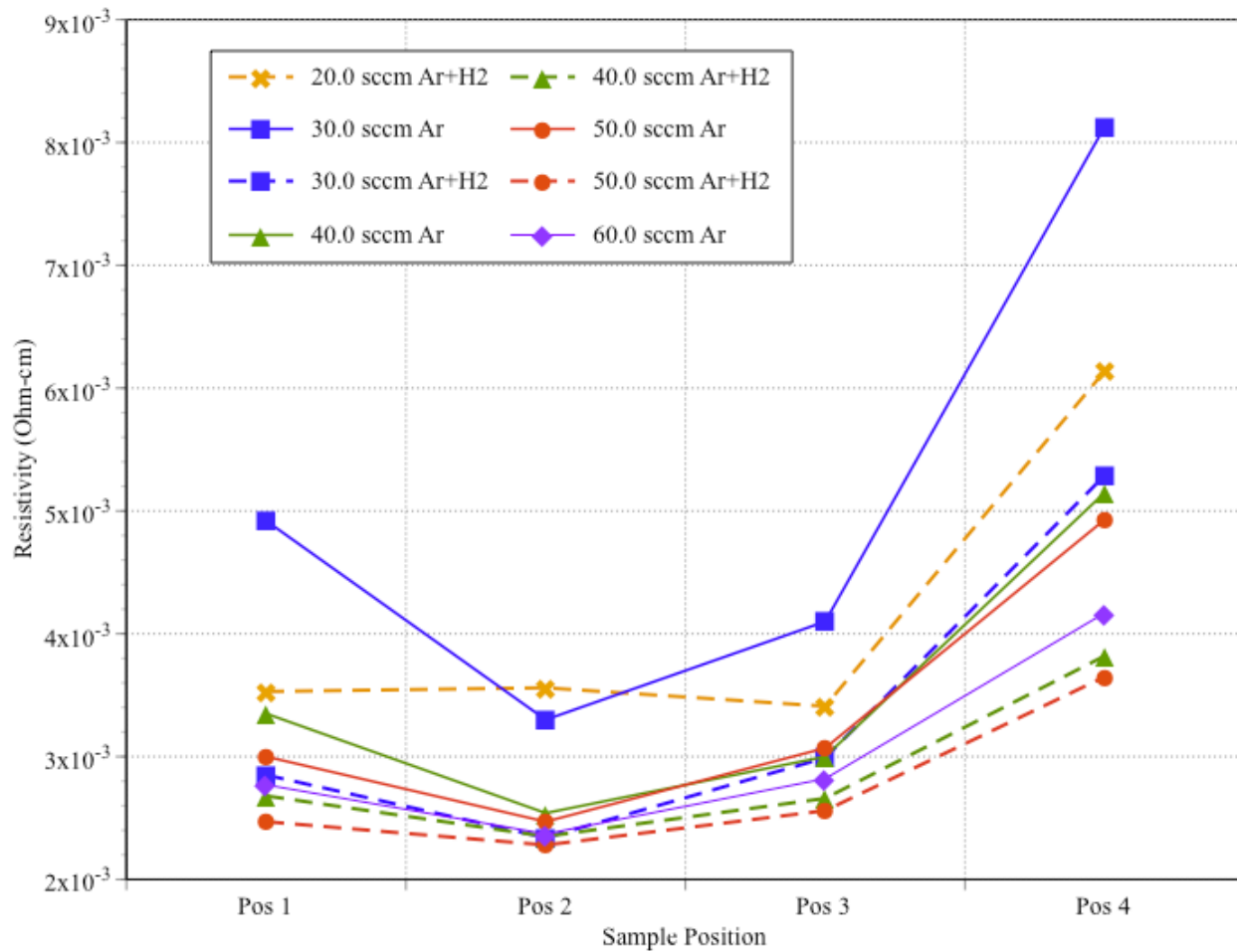


Figure 5-15. Minimum resistivity of AZO and HAZO films deposited at 0.4 kW.

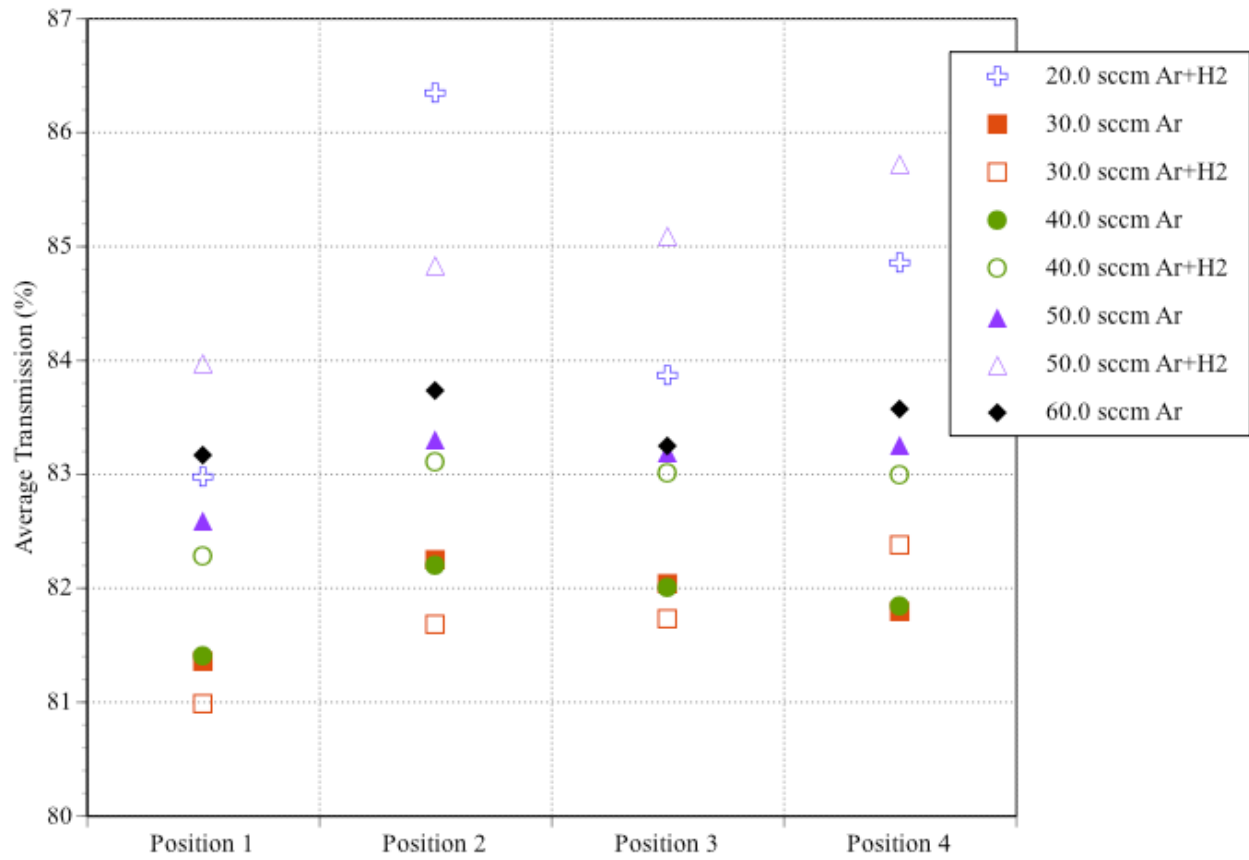


Figure 5-16. Average transmission of AZO and HAZO films deposited at 0.4 kW.

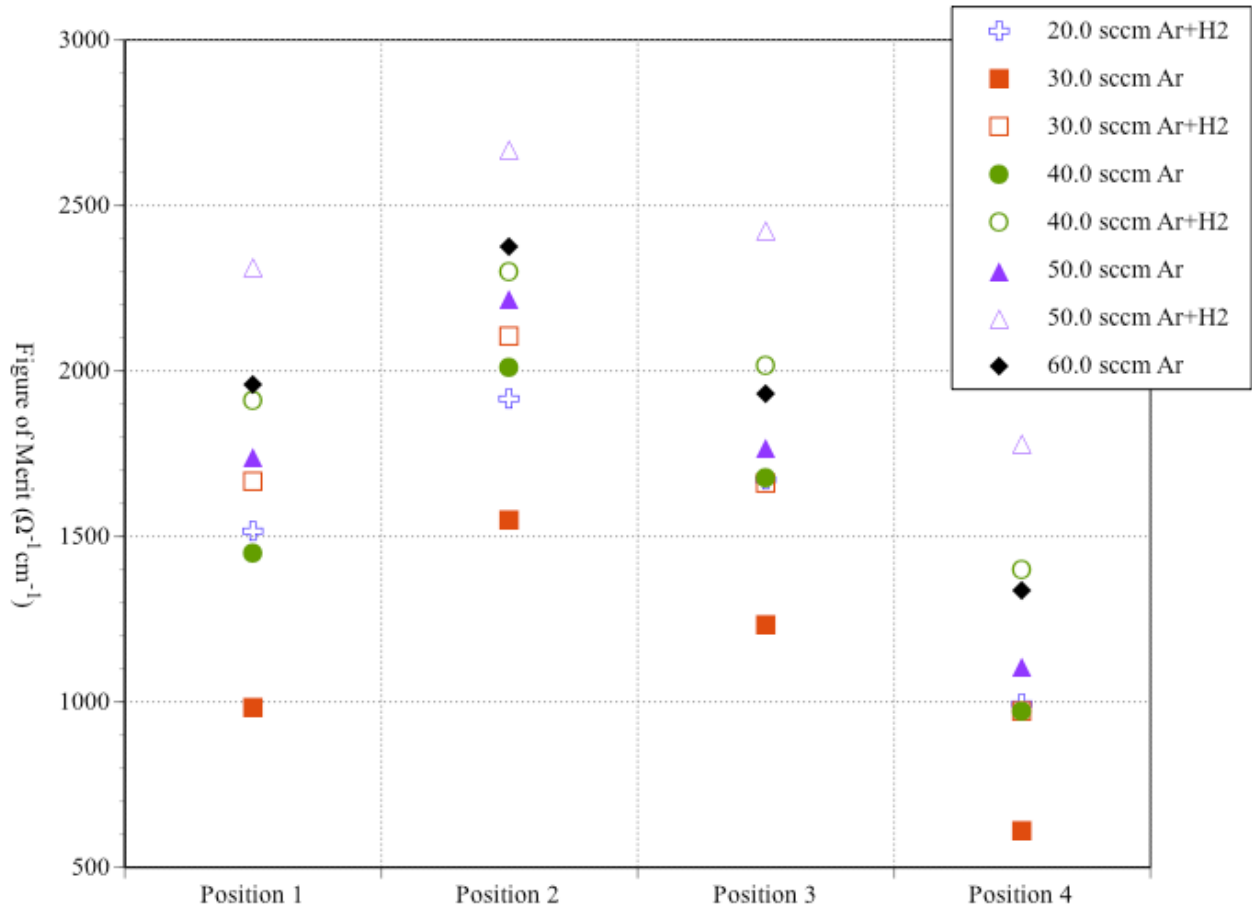


Figure 5-17. Figure of merit for AZO and HAZO films deposited at 0.4 kW.

## CHAPTER 6 THERMAL TREATMENT OF ZINC OXIDE

### **Introduction**

The application of thermal treatments has long been a method to increase the quality of thin films. Thermal treatments in reducing ambients have been shown to lower the resistivity of Al-doped ZnO thin films by an order of magnitude to the  $10^{-3}$  to  $10^{-4}$   $\Omega\cdot\text{cm}$  range [114-117]. Hydrogen treatments tend to see dramatic improvement in film resistivity and carrier concentration due to desorption of negatively charged oxygen species from grain boundaries, which form potential barriers by acting as trapping sites [103, 118].

Al-doped zinc oxide (AZO) has gained significant attention as an abundant, low cost, and non-toxic alternative to indium tin oxide (ITO). AZO thin films, with band gap energy of 3.3 eV, exhibit low resistivities ( $10^{-4}$   $\Omega\cdot\text{cm}$ ) and high optical transmittance (>90%) in the visible light spectrum [119, 120]. As a result, AZO finds use in many advanced applications such as flat panel display electrodes [121], solar cells [66, 122, 123], optical waveguides [124], surface acoustic devices [125], and gas sensors [126].

Transparent conductive oxides are generally desired for their high transparency and excellent electrical conductivity, and are most often deposited via chemical vapor deposition [127, 128], spray pyrolysis [129], reactive sputtering [130, 131], ion beam sputtering [132], or the sol-gel method [114, 133]. Sn-doped  $\text{In}_2\text{O}_3$  (ITO),  $\text{SnO}_2$ , and ZnO are examples of transparent conductive oxides that have been widely studied [134]. Zinc oxide TCOs are most often doped, with dopants such as Ga [135], Si [136], and Al [137]. The properties of these Al-doped ZnO thin films can be altered by post-deposition annealing at elevated temperatures under various ambient atmospheric compositions [111, 114-117, 138-144].

The objective of this work is to determine the effect of thermal treatment on the properties on Al:ZnO (AZO) and H-Al:ZnO (HAZO) thin films. Sputter deposited AZO and HAZO films are annealed at 450°C for 60 minutes. The effect of thermal treatment is examined as a function of three ambient gases, ultra-high purity argon, ultra-high purity nitrogen, and forming gas (96% nitrogen, 4% hydrogen). The change in structural, electrical, and optical characteristics of the Al:ZnO and H-Al:ZnO thin films as a function of the three ambient gases is investigated.

Anneal temperatures of 300°C to 600°C under varying ambient gases have been found to significantly improve electrical properties of AZO films. These elevated temperatures are often incompatible with the thermal budgets of most applications such as photovoltaics and display devices. Regardless, the application of these thermal treatments provides insight into increasing the quality of as-deposited ZnO.

### **Experimental**

This work consists of rapid thermal annealing of Al:ZnO (AZO) and H-Al:ZnO (HAZO) thin films that have been sputter deposited on glass substrates. Samples are subjected to thermal treatment at 450°C for 60 minutes under three ambient gases, ultra-high purity argon, nitrogen, and forming gas (96% N<sub>2</sub>, 4% H<sub>2</sub>). The effect of thermal treatment on film characteristics before and after thermal treatment is investigated. Four-point probe and uv/vis spectroscopy are used to measure film resistivity and optical transmission. Film thickness is measured using profilometry. Powder x-ray diffraction and atomic force microscopy are used to analyze the structural characteristics and surface roughness of the thermally treated AZO and HAZO films. Atomic force microscopy is used to probe surface roughness of as-deposited and annealed films. Depth profiling of the thermally annealed films is provided by secondary ion mass spectrometry.

## Equipment

A Perkin-Elmer Model 4400 Production Sputtering system is used to sputter deposit zinc oxide thin films on Corning 1737 glass substrates with a base pressure of  $2.6 \times 10^{-6}$  Torr. Aluminum-doped zinc oxide is deposited using a zinc oxide target that is doped with  $\text{Al}_2\text{O}_3$  in an ultra-high purity Ar working gas environment. The content of  $\text{Al}_2\text{O}_3$  in the target is 2% in weight and measures eight inches in diameter. Hydrogen-aluminum-doped zinc oxide is deposited using the  $\text{Al}_2\text{O}_3$  doped target along with an ultra-high purity Ar and  $\text{H}_2$  (0.1%) sputtering gas mixture.

A schematic of the rapid thermal processing apparatus is pictured in Figure 6-1. It features a quartz tube chamber and sample holder that is able to accommodate samples up to 1" x 3". Three gas cylinders can be connected to the gas inlet and the flow of gases are controlled by the regulator on each cylinder. A halogen lamp array is located above and below the quartz chamber. The power to these lamp arrays is controlled by the temperature controller, which measures the sample temperature via a thermocouple and adjusts the lamp power to achieve the desired set point. The controller settings can be adjusted to provide accurate control of the sample temperature during ramp, hold, and cool down phases.

An Alessi four-point probe system is used to measure the resistivity of the sputter deposited films before and after thermal treatment. The system features 0.05" spaced tungsten-carbide probe tips, which are 0.002" in diameter. Currents of 1  $\mu\text{A}$  to 100 mA are supplied by a Crytronics Model 120 current source. The voltage resulting across the inner probes is measured by a Keithley Model 181 Nanovoltmeter which is capable of 10 nV sensitivity. Optical transmission of the films is measured from 300 nm to 900 nm using a Perkin-Elmer Lambda 800 spectrophotometer. The system uses twin beams, tungsten and deuterium, to collect

transmittance spectra and a reference sample to provide background correction of measured spectra.

The structural characteristics of the films are analyzed with a Philips APD 3720 powder diffractometer operating at 40KV and 20mA, which uses Cu  $\alpha$  radiation ( $\lambda = 0.154056$  nm). Survey spectra scans are run with a  $0.03^\circ$  step size and a step time of 0.5 second per step. High resolution spectra scans are produced by reducing the step size to  $0.01^\circ$  and increasing the scan rate to 1.0 second per step. The thickness of the films is obtained using a Veeco Dektak 150 Surface Profiler, which has a vertical measurement range of 512  $\mu\text{m}$  and can perform precise step measurements of thin films down to 100  $\text{\AA}$ .

The surface morphology of the films are analyzed with a Digital Instruments Dimension 3100 atomic force microscope. The AFM allows for large samples up to six inches, a large scan size of up to 100  $\mu\text{m}$ , with a sub-angstrom vertical resolution. A JEOL JSM-6335F field emission scanning electron microscope is used to produce visual images of the deposited films. The FE-SEM is capable of accelerating voltages of 0.5 to 30 KV. Both secondary and backscatter electron imaging modes are available and can produce digital images up to 2048 x 2048 pixels.

## **Materials**

Zinc oxide thin films are sputter deposited on Corning 1737 glass substrates, which must be thoroughly cleaned before use. Glass substrates are washed with deionized water to remove visible contaminants and subjected to a series of hot deionized water baths. Substrates are mechanically scrubbed with an Alconox detergent solution before being placed in hot deionized water bath, then ultrasonic cleaned, placed in a three-step cascade of deionized water, and finally dried with nitrogen gas. The glass substrate cleaning procedure is further detailed in Chapter 3.

Aluminum-doped and hydrogen-aluminum-doped films are sputtered from an 8-inch zinc oxide target doped with Al<sub>2</sub>O<sub>3</sub> (2wt%). Al-doped ZnO is deposited in an UHP Ar working gas environment while a mixture of UHP Ar and H<sub>2</sub> (0.1%) serves as the working gas for H-Al-doped ZnO. Acetone is used to remove Sharpie ink when creating trenches for subsequent thickness measurements.

### **Annealing Results**

The effect of ambient gas on annealing of transparent conductive zinc oxide is presented. Structural characterization of the annealed zinc oxide thin films is performed via x-ray diffraction (XRD). Four-point probe measurement is used for electrical characterization of annealed ZnO thin films. Sample resistivity is determined using film thicknesses measured via profilometry. UV/Vis spectroscopy is used to determine the optical characteristics of annealed ZnO in the range of 400 nm to 800 nm. A figure of merit calculation is used to select the growth parameters that produce films with superior optoelectronic properties.

### **Electrical Characterization**

Four-point probe is used to investigate the effect of thermal treatment parameters on AZO and HAZO electrical characteristics. The sheet resistance of thin films can be obtained as

$$R_s = 4.53 \left( \frac{V}{I} \right) \quad (6-1)$$

where  $I$  and  $V$  are the current and voltage, respectively, and 4.53 is the geometric factor as discussed in Chapter 3. The thickness of the film can be used to calculate film resistivity

$$\rho = R_s t = 4.53 \left( \frac{V}{I} \right) t \quad (6-2)$$

where resistivity is given as the product of sheet resistance and film thickness. Films are annealed for 60 minutes at 450°C in forming gas, argon, and nitrogen ambients, with ramp and

cool down times of 10 minutes and 15 minutes, respectively. The thickness and sheet resistance are measured before and after annealing to determine the change in film resistance as a result of the ambient gas used during the thermal treatment process. Both AZO and HAZO films are deposited at 0.4 kW with a base pressure of  $2.6 \times 10^{-6}$  Torr. A working gas flowrate of 40.0 sccm is used to deposit both AZO and HAZO films used in this study. Samples are deposited for 10 minutes with 10 minutes pre-sputter of the target before opening the shutter to expose the substrate to the sputtered material. A complete list of electrical characterization results for AZO and HAZO is found in Table 6-2 and 6-3, respectively.

### **Aluminum doped**

The effect of thermal treatment with three ambient gases on AZO minimum and maximum resistivity is shown in Figure 6-2. The minimum film resistivity is plotted using the left-hand vertical axis and the maximum resistivity using the right-hand vertical axis. The horizontal axis categorizes the ambient gas used during annealing. Pre-anneal measurements are plotted with a dashed line, while post-anneal measurements are plotted with a solid line. The minimum and maximum values are assigned a marker style as denoted in the legend. For example, the film annealed in argon has a maximum film resistivity of  $4.03 \times 10^{-3} \Omega \cdot \text{cm}$  after thermal treatment.

In terms of maximum film resistivity, both forming gas and nitrogen ambients show a large decrease in resistance of 82.5% and 94.4%, respectively. Forming gas and nitrogen ambients also had a large impact on minimum resistivity, which decreases by 63.1% and 57.0% for the two gases. The use of argon ambient also results in a decrease in resistance for both minimum and maximum values, however the change was not as significant compared to forming gas and nitrogen. The forming gas ambient yielded the best results from a minimum and maximum standpoint,  $9.4 \times 10^{-4} \Omega \cdot \text{cm}$  and  $1.04 \times 10^{-3} \Omega \cdot \text{cm}$ , respectively. It is important to note that Figure 6-2 shows that an as-deposited film with poor electrical characteristics can be

significantly improved by thermal treatments, as can be seen in the case of the film annealed in nitrogen.

### **Hydrogen and aluminum doped**

Figure 6-3 shows the effect of forming gas, argon, and nitrogen ambients on the minimum and maximum resistivity of HAZO sputter deposited films. The left-hand vertical axis is used to measure minimum resistivity and the right-hand vertical axis is used to measure maximum resistivity. A dashed line is used for pre-anneal measurements, while a solid line reflects measurements that are acquired after annealing. The minimum and maximum values are assigned a marker style as denoted in the legend. For example, the HAZO film annealed in nitrogen has a maximum film resistivity of  $4.81 \times 10^{-3} \Omega \cdot \text{cm}$  after thermal treatment. Table 6-3 gives the film resistance data for all ambient gases, including the thickness and sheet resistance measurements used in the resistivity calculation.

It is evident that thermal treatment of HAZO in argon ambient is extremely detrimental to the film's electrical characteristics. Annealing in the argon ambient increased the HAZO minimum film resistivity 175.4% from  $2.66 \times 10^{-3} \Omega \cdot \text{cm}$  to  $7.33 \times 10^{-3} \Omega \cdot \text{cm}$  and the maximum resistivity increased 469.3%, from  $5.974 \times 10^{-3} \Omega \cdot \text{cm}$  up to  $3.40 \times 10^{-2} \Omega \cdot \text{cm}$ . Similar to AZO, the forming gas and nitrogen ambients decreased both minimum and maximum film resistivity. Annealing in forming gas produced a high quality HAZO film with a minimum resistivity of  $1.15 \times 10^{-3} \Omega \cdot \text{cm}$ , and a maximum of  $1.33 \times 10^{-3} \Omega \cdot \text{cm}$ .

### **Optical Characterization**

The optical transmission of annealed ZnO thin films is studied using UV/Vis spectroscopy in the 300 nm to 900 nm range. The transmittance spectra are measured without the use of an integrating sphere. A bare glass substrate with no deposited ZnO is measured in order to factor out transmission loss from the substrate itself. The average transmission between 400 nm and

800 nm of AZO and HAZO films before and after thermal treatment is presented. A complete list of optical characterization results for AZO and HAZO is found in Table 6-2 and 6-3, respectively.

### **Aluminum doped**

The effect of thermal treatment on the average transmission of AZO films is shown in Figure 6-4. The average transmission is graphed on the vertical axis, and the horizontal axis categorizes the ambient gas used during thermal treatment. A circle marker is assigned to pre-anneal values and a square marker to post-anneal values, as denoted in the legend. The average transmission is seen to increase 6.0%, 5.0%, and 5.6% for the AZO film annealed in forming gas, argon, and nitrogen, respectively. Most likely the transmission increase is most heavily influenced by the thermal budget of the annealing process rather than the gas ambient.

### **Hydrogen and aluminum doped**

Figure 6-5 presents the pre-anneal and post-anneal average transmission for HAZO films treated in forming gas, argon, and nitrogen ambients. The vertical axis plots the average transmission, and the horizontal axis categorizes the ambient gas used during thermal treatment. A circle marker is assigned to pre-anneal values and a square marker to post-anneal values, as denoted in the legend. As with AZO, the average transmission of HAZO films is seen to increase in all three ambient gases. However, the argon ambient only increases the HAZO transmission by 1.9%, whereas the other ambients each increase the transmission by 5.0%. Given the post-anneal resistivity results of HAZO films, it's possible that argon provides some counter-productive mechanism that is outweighed by the increase in transmission provided by the thermal budget.

## Figure of Merit

High transmission and low electrical resistivity are two parameters that are extremely important to transparent conductors. In order to evaluate the quality of an optoelectronic film, a figure of merit performance parameter is calculated which is based off the ratio of film resistivity to the visible transmission. The figure of merit is defined as

$$\text{FOM} = -\frac{1}{\rho \ln(T)} \quad (6-3)$$

where  $\rho$  is the film resistivity and  $T$  is the average transmission in the 400 nm to 800 nm range [111-113]. A larger figure of merit (FOM) value indicates superior optoelectronic film properties. The effect of annealing ambient on AZO and HAZO is determined by use of the figure of merit calculation. A complete list of the FOM results for AZO and HAZO is found in Table 6-2 and 6-3, respectively.

## Aluminum doped

The effect of ambient on the figure of merit of thermally treated AZO is shown in Figure 6-6. The vertical axis plots the figure of merit and the horizontal axis categorizes the ambient gas used during thermal treatment. A square marker is assigned to pre-anneal values and a circle marker to post-anneal values, as denoted in the legend. The FOM is seen to increase as a result of thermal treatment for all ambient conditions. Forming gas and nitrogen ambients see the largest improvements with 286% and 220% increases, respectively. From these results it is determined that annealing AZO in forming gas provides the best optoelectronic film properties. The FOM of AZO annealed in forming gas increased from  $2012 \Omega^{-1}\text{cm}^{-1}$  to  $7763 \Omega^{-1}\text{cm}^{-1}$ . This large increase in figure of merit is mostly due to its low resistivity as all three ambients produce fairly equivalent average transmission post-anneal.

## Hydrogen and aluminum doped

Figure 6-7 presents the change in figure of merit for HAZO films annealed in forming gas, argon, and nitrogen ambients. The figure of merit is plotted on the vertical axis and the horizontal axis categorizes the ambient gas used during thermal treatment. A square marker is assigned to pre-anneal values and a circle marker to post-anneal values, as denoted in the legend. The film annealed in argon ambient shows a 60% decrease in FOM, which is a result of the large increase in film resistivity as a result of the thermal treatment. The nitrogen ambient results in a 61% increase in FOM, a result of both improved transmission and decreased resistivity. Again, as with AZO, the film annealed in forming gas shows the largest increase in FOM. The figure of merit increases 176% from  $2303 \Omega^{-2}\text{cm}^{-1}$  to  $6366 \Omega^{-1}\text{cm}^{-1}$  for the HAZO film annealed in forming gas. It is observed that the benefits of hydrogen incorporation must hit some limit, as the forming gas annealed AZO produces a larger FOM than the HAZO annealed under identical conditions, especially given that the HAZO film is considered the superior film according to its pre-anneal FOM value.

## Structural Characteristics

An SEM micrograph depicting the structure of HAZO annealed in argon ambient is shown in Figure 6-8. The image shows a vertical view of the substrate. In areas where the thick gold coating has broken free it can be observed that the HAZO film develops in a columnar grain structure. Often it can be seen that the surface morphology appears textured or cratered. This is a consequence of the nucleation of oriented c-axis grains that grow vertically and impinge laterally. This is the result of competition between the arrival rate of new Al:ZnO species on the surface and redistribution over the surface by diffusion [143]. This non-equilibrium growth results in the surface texturing of the film, which has the potential for enhanced light trapping in photovoltaic devices [145].

## **Surface Roughness**

The change in the surface morphology of the AZO and HAZO sputter deposited films after thermal treatment in forming gas, argon, and nitrogen ambients is investigated using atomic force microscopy (AFM). A Digital Instruments Dimension 3100 atomic force microscope is used to provide digital images and calculate arithmetic roughness ( $R_a$ ) and the root mean square (rms) roughness ( $R_q$ ) of the measured films.

## **Aluminum doped**

The atomic force micrographs of as-deposited and annealed AZO films are shown in Figure 6-9. Each AFM micrograph corresponds to a specific anneal condition as denoted in the figure caption, while the arithmetic and rms roughness values for each condition are listed in Table 6-4. The as-deposited AZO film exhibits and rms roughness of 2.94 nm. Annealing in argon and nitrogen ambients results in increased rms roughness values of 4.53 nm and 4.21 nm, respectively. Generally, although increased surface roughness can lead eventually lead to reduced light trapping, the transmission of AZO annealed in argon and nitrogen increases. However, the rms roughness of AZO annealed in forming gas decreases to 2.80 nm. Although the grain size has decreased, this film shows a large increase in conductivity and the highest FOM of any film as seen in Figure 6-6.

## **Hydrogen and aluminum doped**

Figure 6-10 shows the AFM micrographs of as-deposited and annealed HAZO. Each AFM micrograph corresponds to a specific anneal condition as denoted in the figure caption, while the arithmetic and rms roughness values for each condition are listed in Table 6-4. An rms roughness ( $R_q$ ) of 2.19 nm is reported for as-deposited HAZO. The results for HAZO contrast with the AZO results. Surface roughness decreases when annealed in argon nitrogen ambients,

with measured rms roughness of 1.79 nm and 1.91 nm, respectively. Annealing in forming gas increases the rms roughness to 2.62 nm.

### **Conclusions**

Transparent conductive oxides such as aluminum-doped zinc oxide are desired for use in photovoltaic devices as a result of their high transparency and excellent electrical conductivity. These AZO films have gained significant interest as a low cost, abundant, and non-toxic alternative to the benchmark indium tin oxide films used in many optoelectronic applications. Thermal treatments such as rapid thermal annealing have been identified as possible methods to increase the quality of AZO and HAZO thin films.

Experimental studies show that the resistivity of sputter deposited AZO and HAZO is significantly reduced upon rapid thermal annealing in forming gas, argon, and nitrogen ambients. Annealing HAZO in a forming gas atmosphere results in a resistivity of  $9.4 \times 10^{-4} \Omega \cdot \text{cm}$ . Thermal treatments also result in optical transmission increases up to 6.0% for AZO annealed in forming gas. A figure of merit calculation correlates the resistivity and transmission of these films and provides a quantitative value to each film's ability to provide superior optoelectronic characteristics. In all but one case the annealing of AZO and HAZO results in an increase of 61% to 286% in the figure of merit depending on the ambient used. A cross-sectional scanning electron micrograph shows that annealed HAZO exhibits a very columnar grain structure as expected. A look at surface roughness with AFM shows that argon and nitrogen ambients tend to increase the roughness of AZO films while decreasing the roughness of HAZO films.

Table 6-1. International Centre for Diffraction Data fingerprint for ZnO.

Plane (hkl)	d Spacing (Å)	$2\theta$ (°)	Normalized Intensity
(101)	2.47592	36.253	100
(100)	2.81430	31.770	57
(002)	2.60332	34.422	44
(110)	1.62472	56.603	32
(103)	1.47712	62.864	29
(004)	1.30174	72.562	2

Table 6-2. Thermal treatment results for AZO films.

	Forming Gas		Argon		Nitrogen	
	Before	After	Before	After	Before	After
Average Thickness (nm)	240.0	238.3	236.7	238.3	241.7	248.3
Average Thickness $\Delta$	-0.7%		0.7%		2.8%	
Low Resistivity ( $\Omega\cdot\text{cm}$ )	2.54	0.94	3.00	1.91	5.15	2.21
Low Resistivity $\Delta$	-63.1%		-36.5%		-57.0%	
High Resistivity ( $\Omega\cdot\text{cm}$ )	5.98	1.04	10.76	4.03	62.11	3.49
High Resistivity $\Delta$	-82.5%		-62.5%		-94.4%	
Average Transmission (%)	82.21	87.14	82.02	86.15	81.85	86.44
Average Transmission $\Delta$	6.0%		5.0%		5.6%	
Figure of Merit ( $\Omega^{-1}\text{cm}^{-1}$ )	2012	7763	1681	3516	970	3101
Figure of Merit $\Delta$	286%		109%		220%	

Table 6-3. Thermal treatment results for HAZO films.

	Forming Gas		Argon		Nitrogen	
	Before	After	Before	After	Before	After
Average Thickness (nm)	246.7	238.3	238.3	241.7	248.3	245.0
Average Thickness $\Delta$	-3.4%		1.4%		-1.3%	
Low Resistivity ( $\Omega\cdot\text{cm}$ )	2.35	1.15	2.66	7.33	3.82	3.22
Low Resistivity $\Delta$	-50.9%		175.4%		-15.9%	
High Resistivity ( $\Omega\cdot\text{cm}$ )	4.51	1.33	5.974	34.01	20.51	4.81
High Resistivity $\Delta$	-70.5%		469.3%		-76.6%	
Average Transmission (%)	83.11	87.25	83.02	84.59	83.00	87.15
Average Transmission $\Delta$	5.0%		1.9%		5.0%	
Figure of Merit ( $\Omega^{-1}\text{cm}^{-1}$ )	2303	6366	2018	815	1403	2258
Figure of Merit $\Delta$	176%		-60%		61%	

Table 6-4. Surface roughness of annealed AZO and HAZO measured by AFM.

	As-deposited	Forming Gas	Annealed Argon	Nitrogen
AZO				
R <sub>q</sub> (nm)	2.94	2.80	4.53	4.21
R <sub>a</sub> (nm)	2.31	2.24	3.64	3.44
HAZO				
R <sub>q</sub> (nm)	2.19	2.62	1.79	1.91
R <sub>a</sub> (nm)	1.75	2.00	1.46	1.48

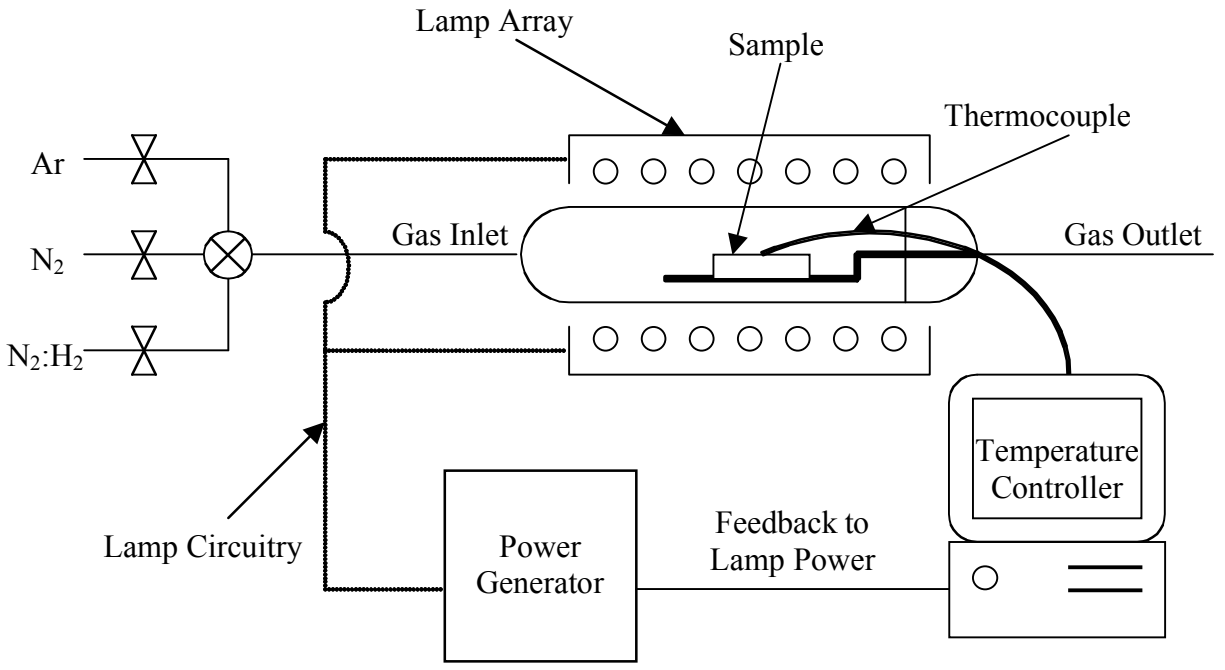


Figure 6-1. Rapid thermal processing schematic.

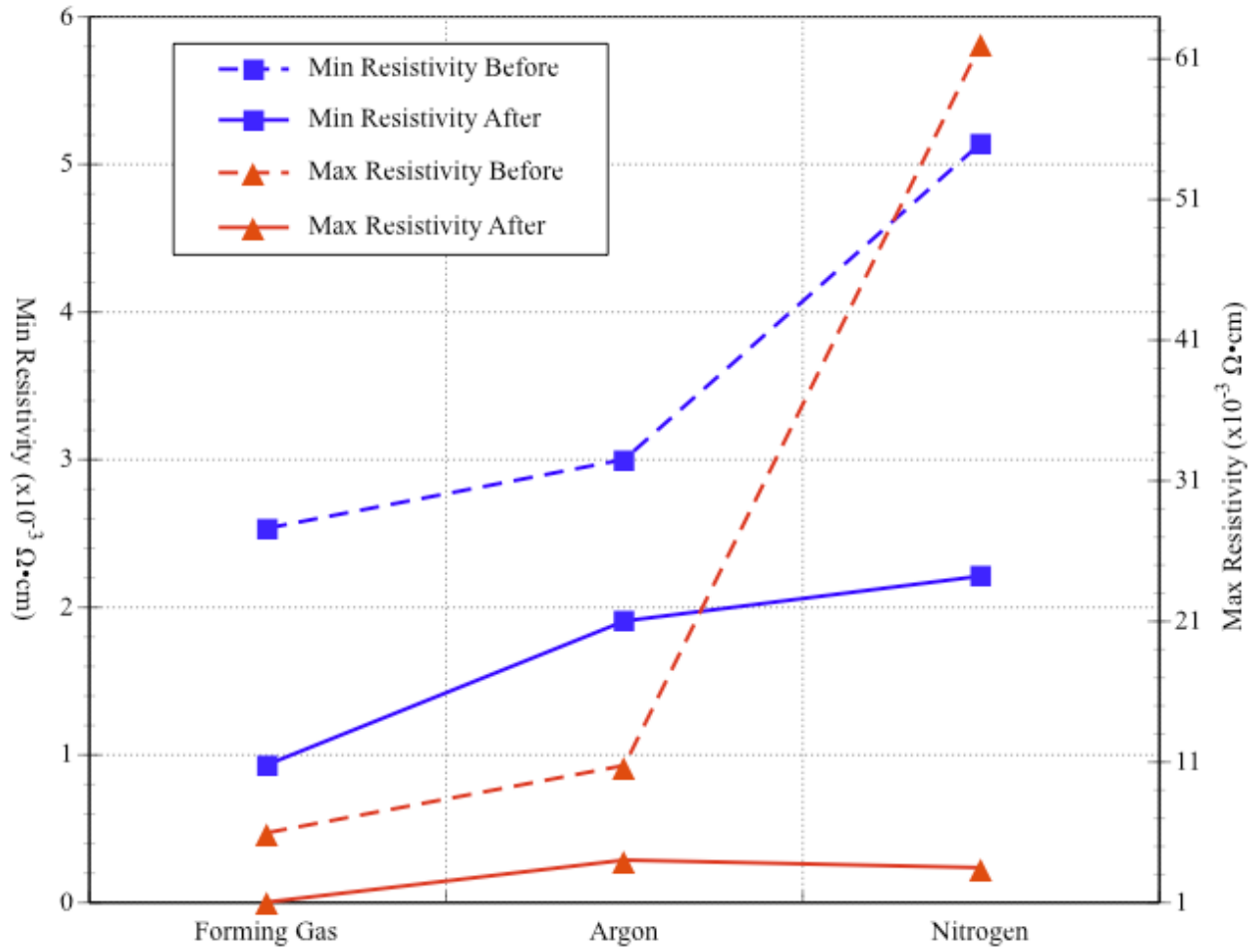


Figure 6-2. Minimum and maximum resistivity of AZO films before and after annealing in forming gas, argon, and nitrogen ambients.

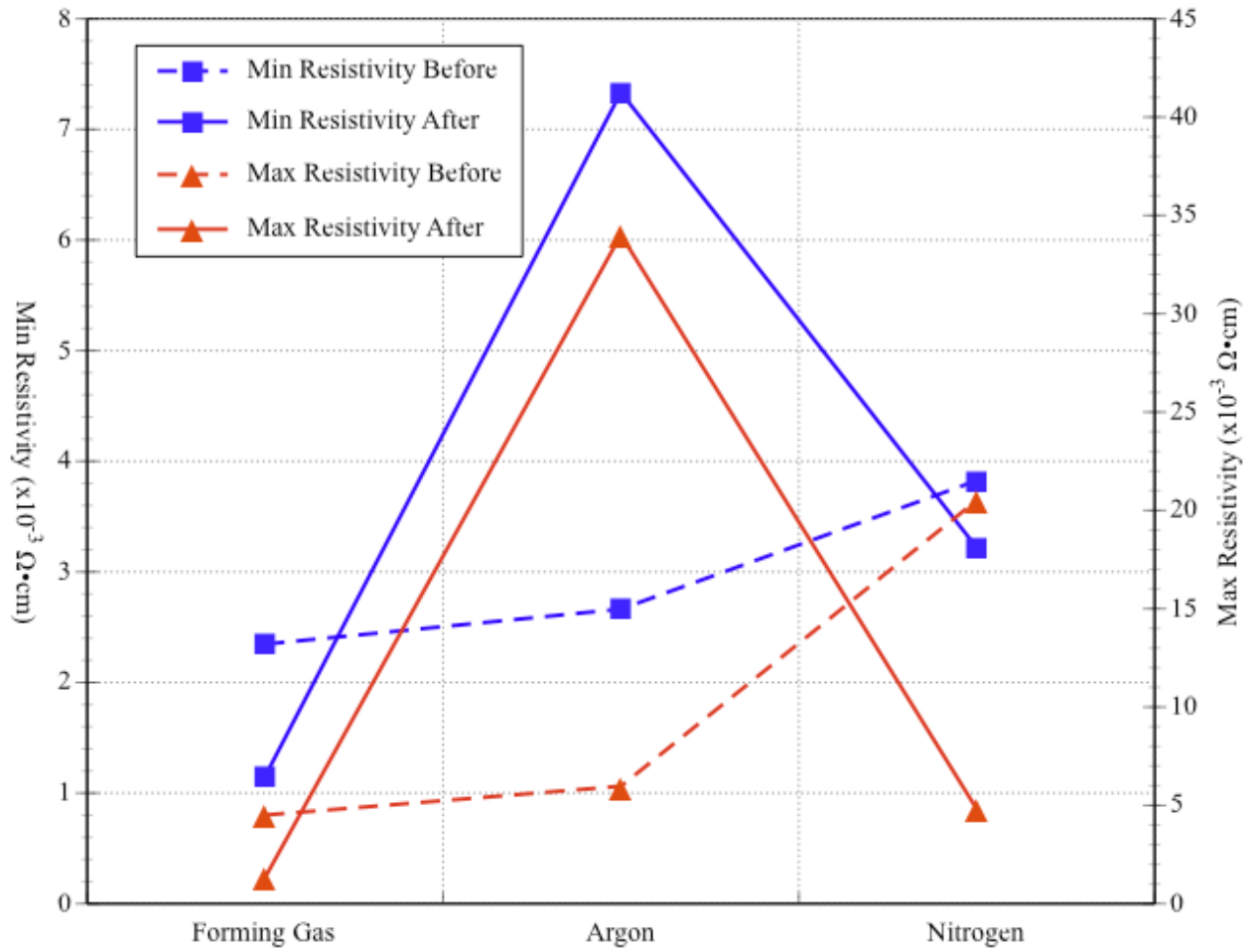


Figure 6-3. Minimum and maximum resistivity of HAZO films before and after annealing in forming gas, argon, and nitrogen ambients.

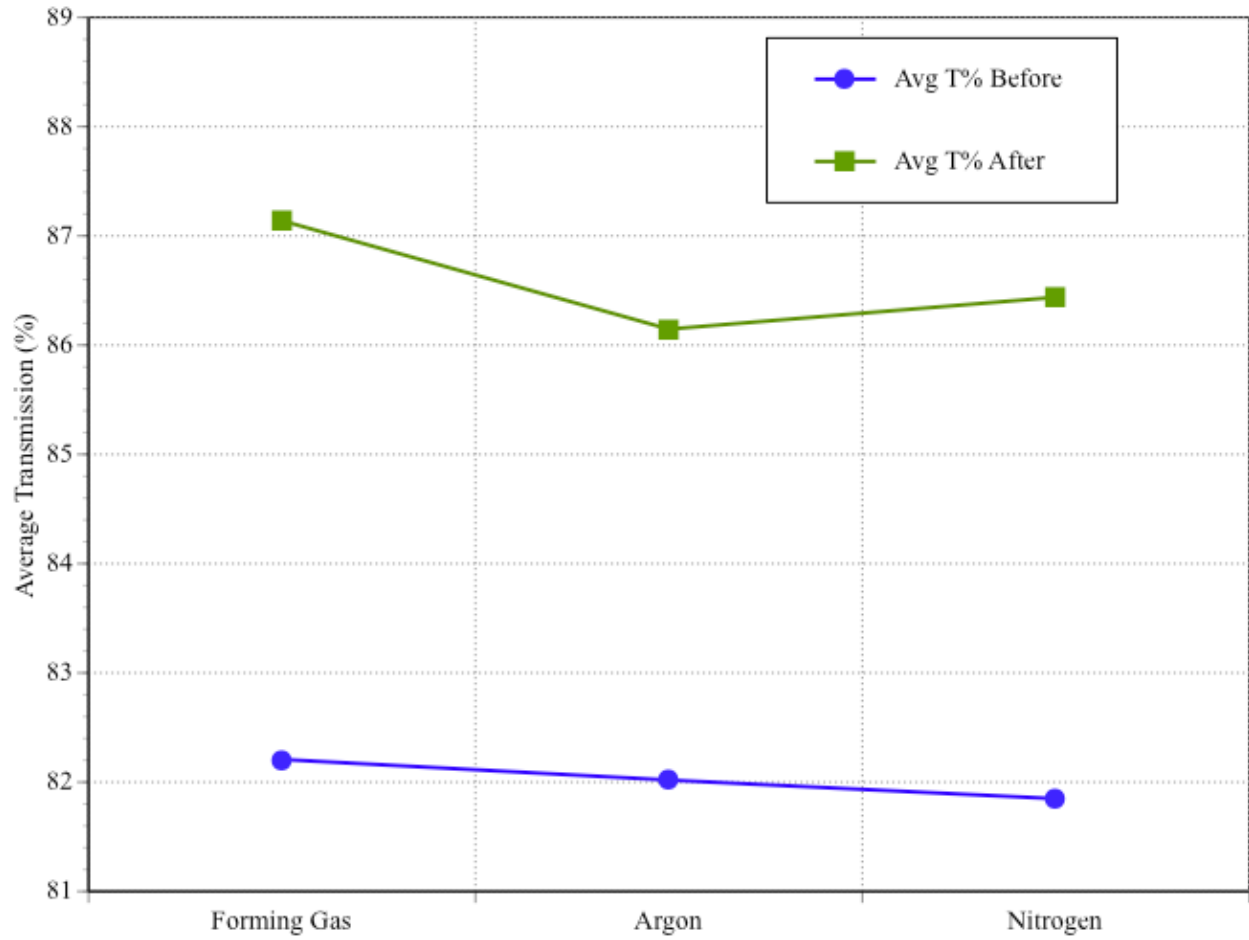


Figure 6-4. Average transmission of AZO films before and after annealing in forming gas, argon, and nitrogen ambients.

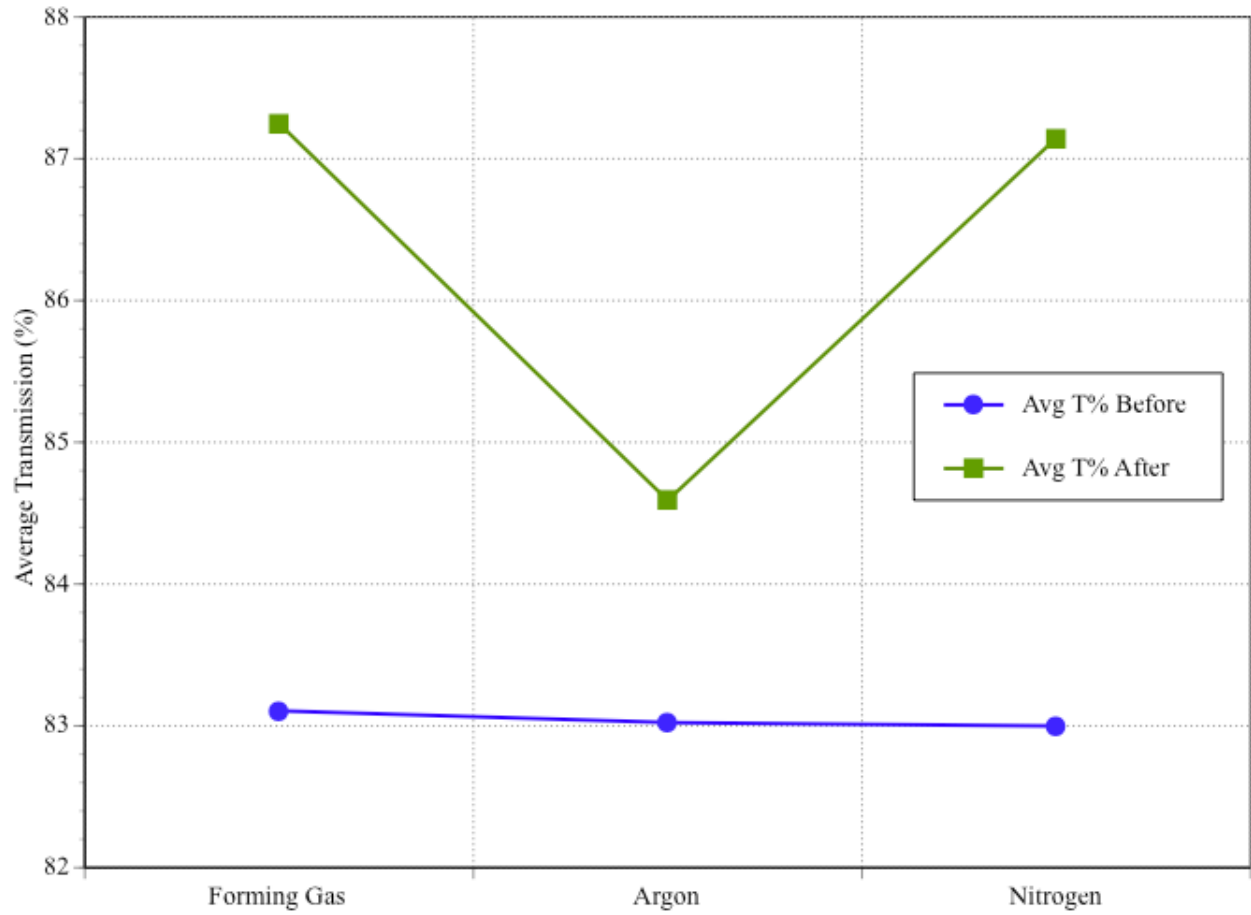


Figure 6-5. Average transmission of HAZO films before and after annealing in forming gas, argon, and nitrogen ambients.

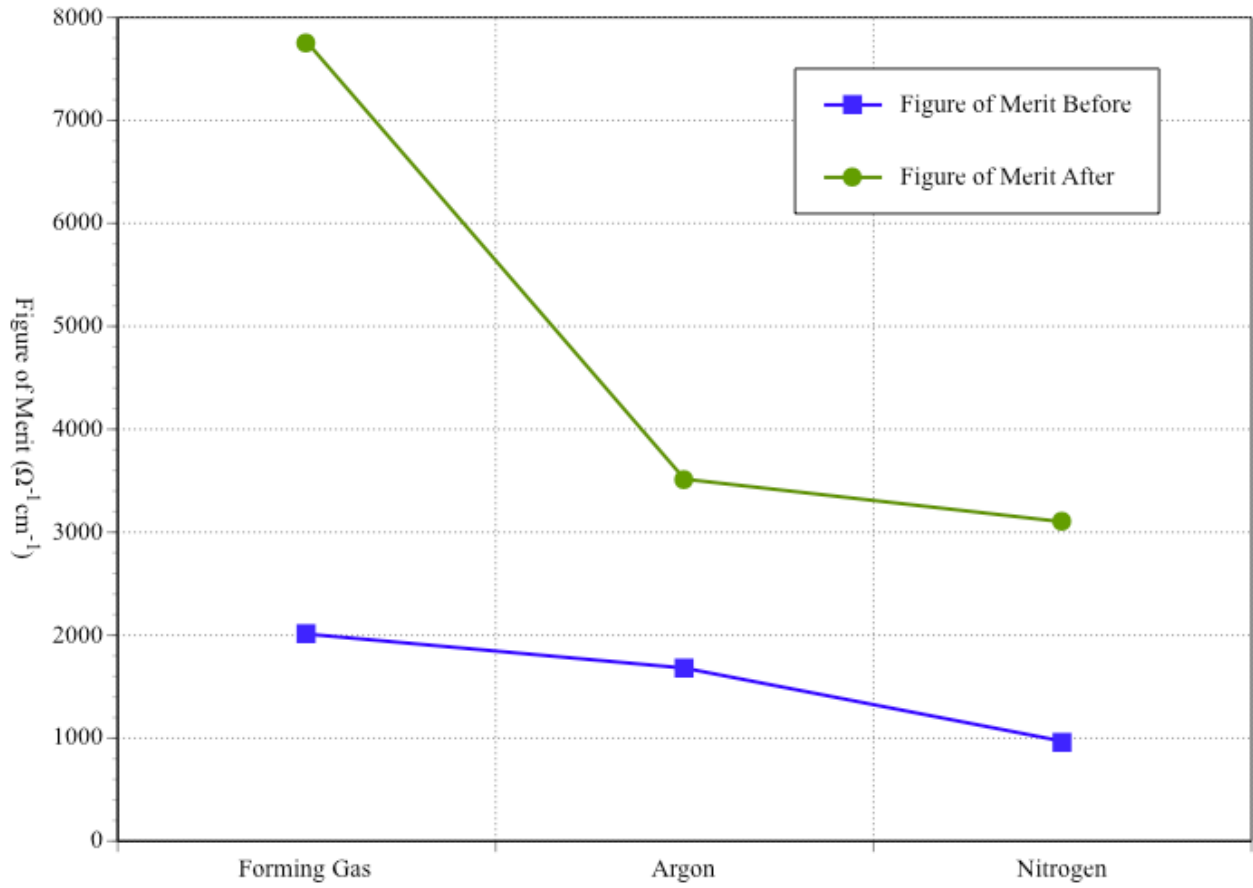


Figure 6-6. Figure of merit of AZO films before and after annealing in forming gas, argon, and nitrogen ambients.

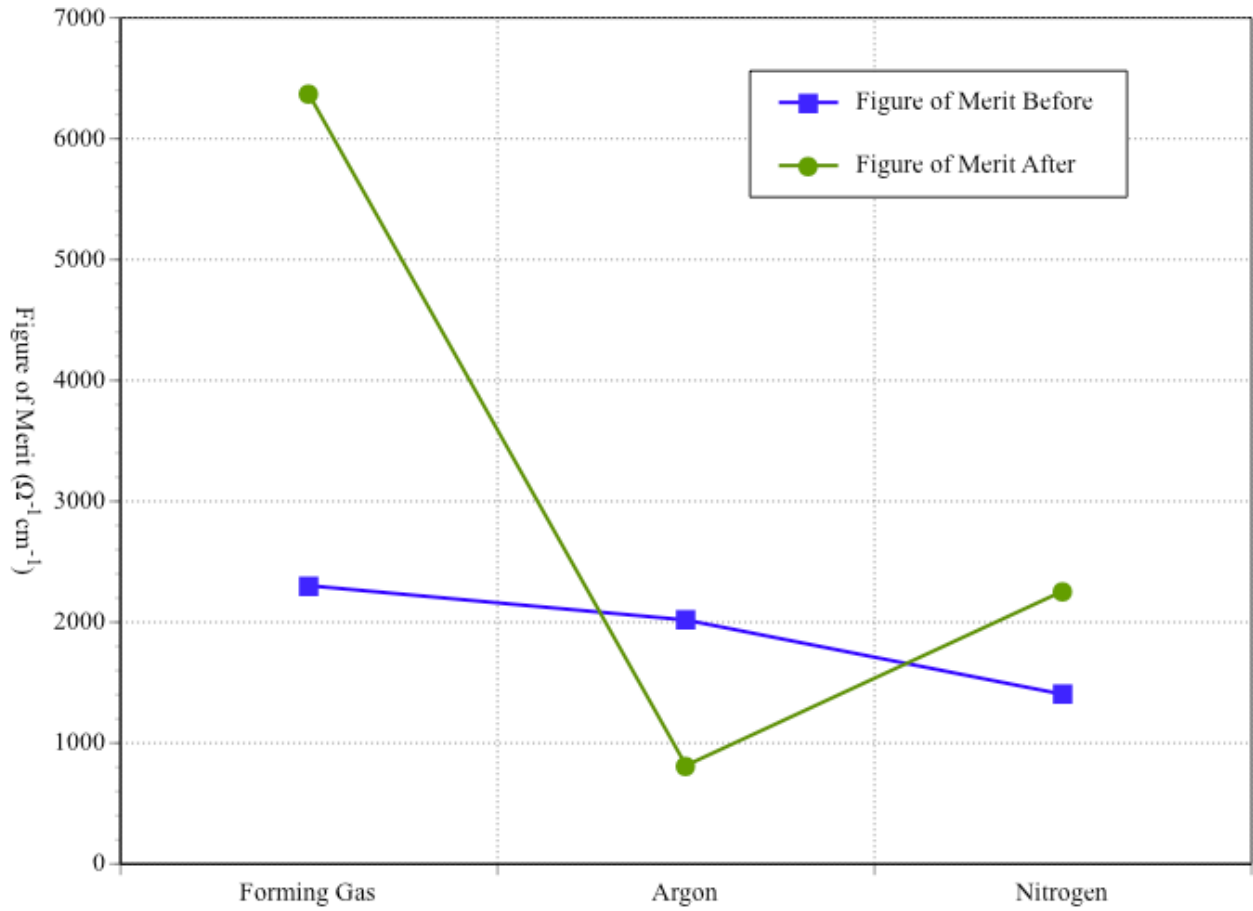


Figure 6-7. Figure of merit of HAZO films before and after annealing in forming gas, argon, and nitrogen ambients.

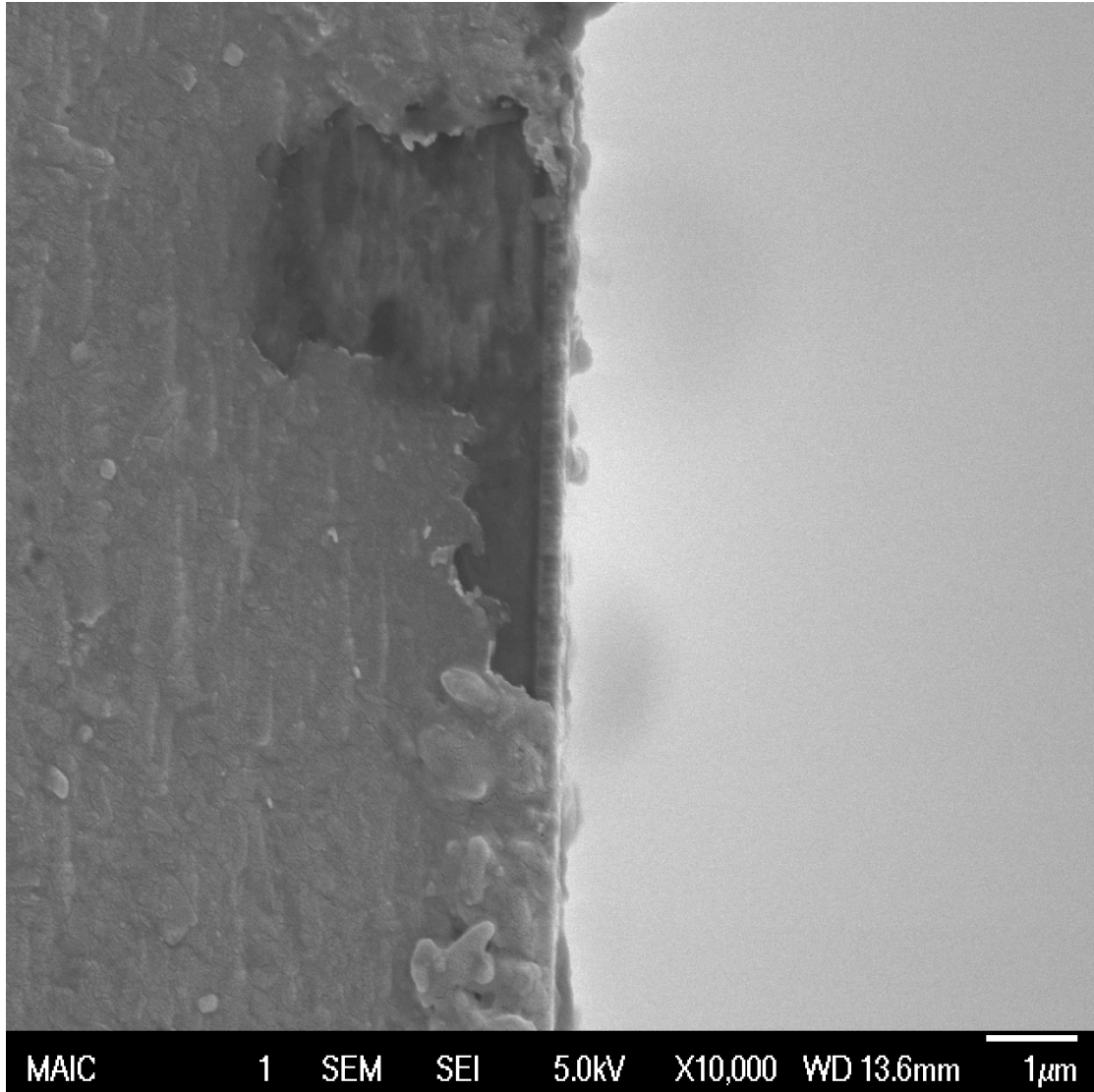


Figure 6-8. Cross-sectional image of HAZO annealed in argon ambient taken with a field-emission scanning electron microscope.

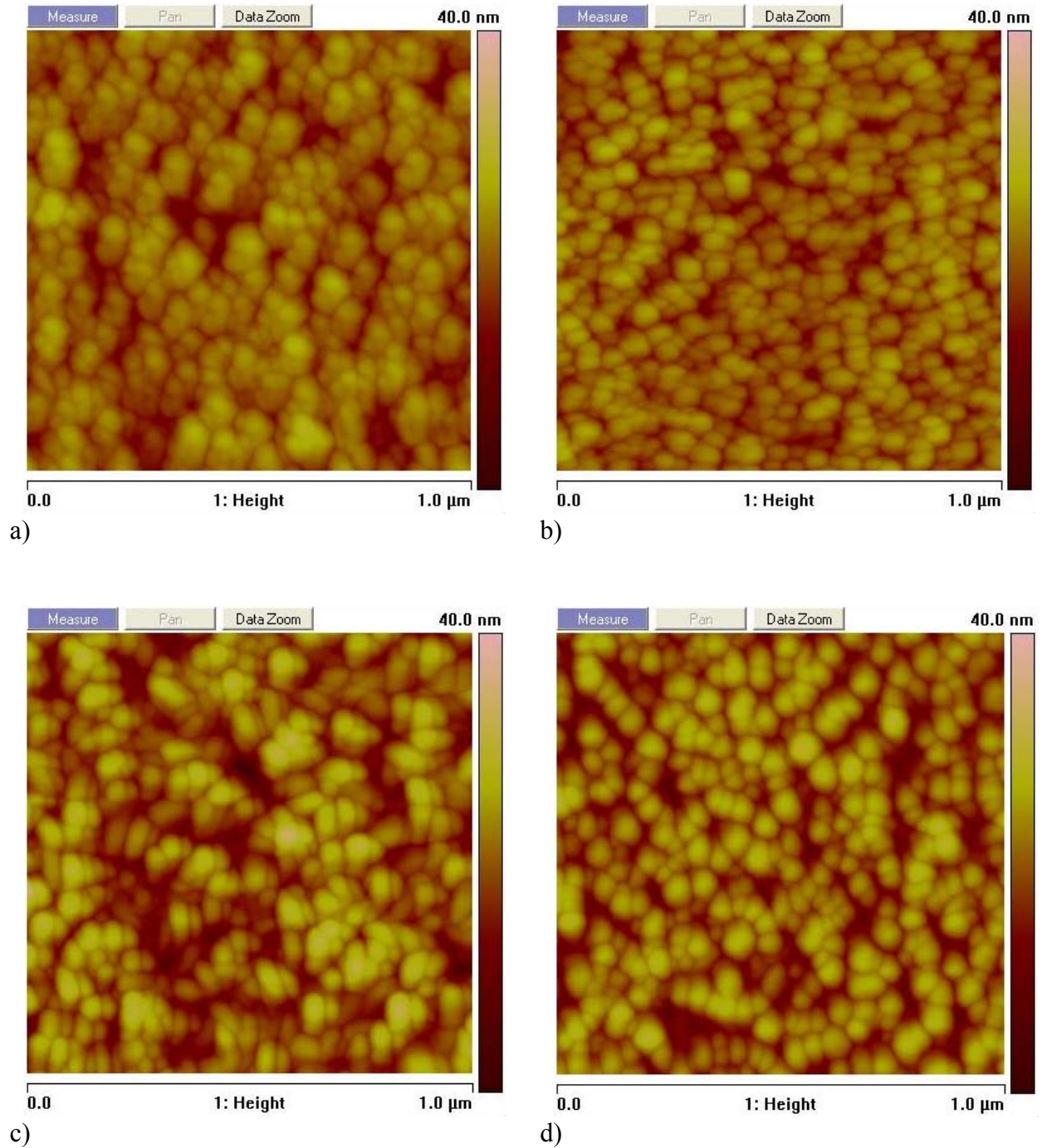


Figure 6-9. Atomic force microscopy of AZO films a) as-deposited, and annealed in b) forming gas, c) argon, and d) nitrogen ambients.

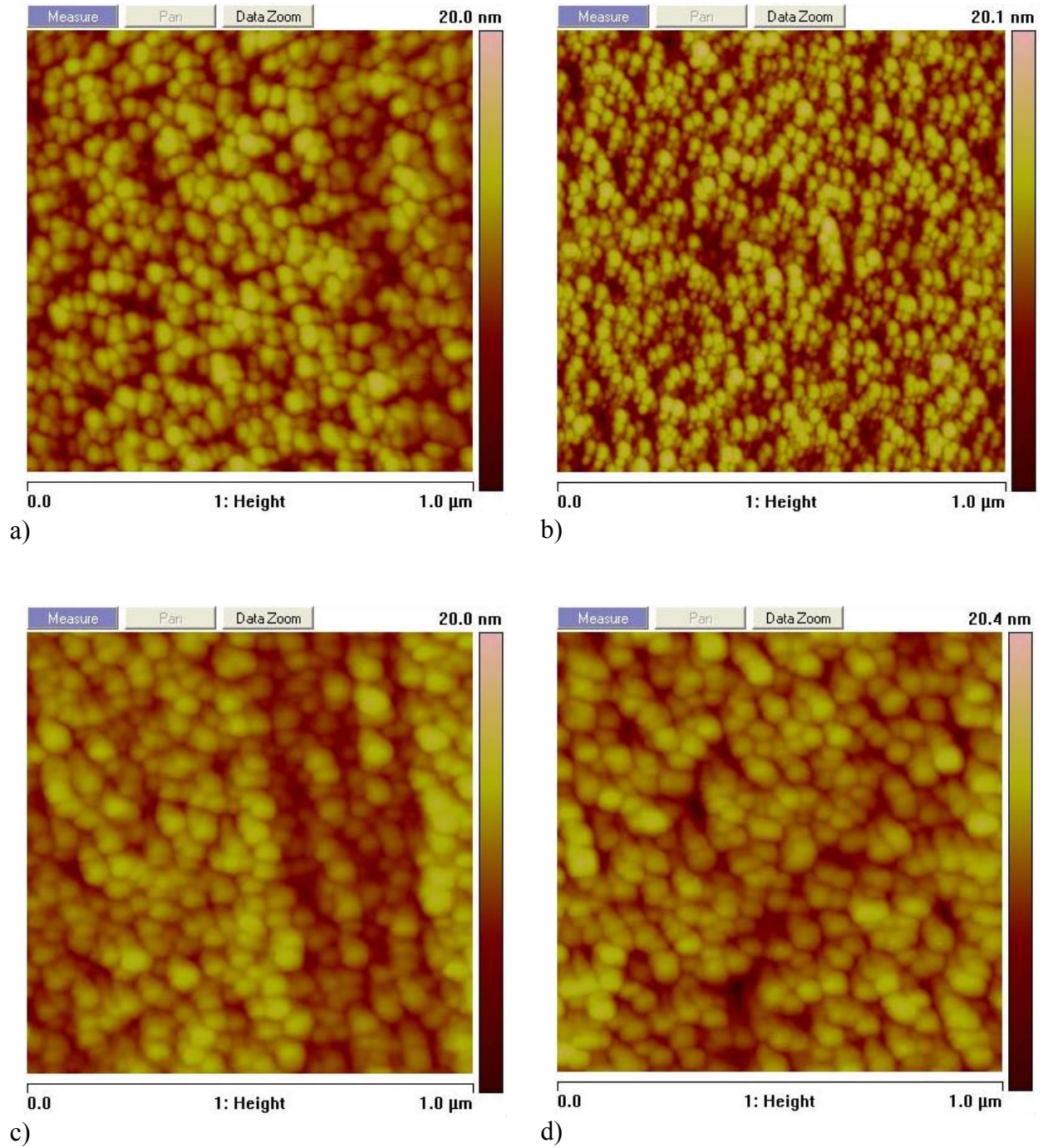


Figure 6-10. Atomic force microscopy of HAZO films a) as-deposited, and annealed in b) forming gas, c) argon, and d) nitrogen ambients.

## LIST OF REFERENCES

- [1] B.C. Farhar, T.C. Coburn, Colorado Homeowner Preferences on Energy and Environmental Policy (National Renewable Energy Laboratory, 1999).
- [2] U.S. DOE, Energy Information Agency, International Energy Annual 2000 (US. Department of Energy, 2000).
- [3] U.S. DOE, Energy Information Agency, Monthly Energy Review (US. Department of Energy, 2002).
- [4] J. Mortensen, Factors Associated with Photovoltaic System Costs (Topical Issues Brief) (National Renewable Energy Laboratory, 2001).
- [5] M. Thomas, H. Post, R. DeBlasio, Progress in Photovoltaics: Research and Applications 7 (1999) 1-19.
- [6] R.F. Pierret, Semiconductor Device Fundamentals (Addison-Wesley Publishing Company, New York, 1996).
- [7] W.K. Kim, Study of Reaction Pathways and Kinetics in  $\text{Cu}(\text{In}_x\text{Ga}_{1-x})\text{Se}_2$  Thin Film Growth, Ph.D. Thesis, University of Florida, 2006.
- [8] B. von Roedern, K. Zweibel, H.S. Ullal, Conference Record of the Thirty-first IEEE Photovoltaic Specialists Conference, 2005, pp. 183-188.
- [9] S.J. Jones, T. Liu, X. Deng, M. Izu, E.C.D. Inc, M.I. Troy, Conference Record of the Twenty-Eighth IEEE Photovoltaic Specialists Conference, Anchorage, AK, 2000, pp. 845-848.
- [10] A. Shah, J. Dutta, N. Wyrsh, K. Prasad, H. Curtins, F. Finger, A. Howling, C. Hollenstein, Materials Research Society Symposium Proceedings, 1992, pp. 15-26.
- [11] B.P. Nelson, E. Iwaniczko, A.H. Mahan, Q. Wang, Y. Xu, R.S. Crandall, H.M. Branz, Thin Solid Films 395 (2001) 292-297.
- [12] Y. Mori, K. Yoshii, K. Yasutake, H. Kakiuchi, S. Kiyama, H. Tarui, Y. Domoto, Journal of the Japan Society for Precision Engineering 65 (1999) 1600-1604.
- [13] B. Tell, J.L. Shay, H.M. Kasper, Physical Review B 4 (1971) 2463-2471.
- [14] D. Braunger, T. Durr, D. Hariskos, C. Koble, T. Walter, N. Wieser, H.W. Schock, Conference Record of the Twenty Fifth IEEE Photovoltaic Specialists Conference, Washington, DC, 1996, pp. 1001-1004.
- [15] K. Siemer, J. Klaer, I. Luck, J. Bruns, R. Klenk, Solar Energy Materials & Solar Cells 67 (2001) 159-166.

- [16] S. Siebentritt, *Thin Solid Films* 403-404 (2002) 1-8.
- [17] B.J. Stanbery, *Conference Record of the 31st IEEE Photovoltaic Specialists Conference*, Lake Buena Vista, FL, 2005, pp. 355-358.
- [18] H.J. Moller, *Semiconductors for Solar Cells* (Artech House, Inc., Norwood, MA, 1993).
- [19] H.W. Schock, R. Noufi, *Progress in Photovoltaics Research and Applications* 8 (2000) 151-160.
- [20] M. Yamaguchi, *Journal of Applied Physics* 78 (1995) 1476.
- [21] M.A. Contreras, E. Egaas, K. Ramanathan, J. Hiltner, A. Swartzlander, J. Hasoon, R. Noufi, *Progress in Photovoltaics: Research and Applications* 7 (1999) 311-316.
- [22] H.S. Ullal, K. Zweibel, B.G. von Roedern, *Conference Record of the Twenty-Eighth IEEE Photovoltaic Specialists Conference*, Anchorage, AK, 2000, pp. 100.
- [23] W. Horig, H. Neumann, B. Schumann, G. Kuhn, *Physica Status Solidi* 85 (1978) K57.
- [24] K. Yoshino, N. Mitani, T. Ikari, P. Fons, S. Niki, A. Yamada, *Solar Energy Materials and Solar Cells* 67 (2001) 173-178.
- [25] C.H. Henry, *Journal of Applied Physics* 51 (1980) 4494-4500.
- [26] M. Saad, A. Kassis, *Solar Energy Materials and Solar Cells* 77 (2003) 415-422.
- [27] D.L. Young, J. Keane, A. Duda, J.A. Abushama, C.L. Perkins, M. Romero, R. Noufi, *Progress in Photovoltaics: Research and Applications* 11 (2003) 535-541.
- [28] V. Nadenau, U. Rau, A. Jasenek, H.W. Schock, *Journal of Applied Physics* 87 (2000) 584-593.
- [29] A. Jasenek, U. Rau, V. Nadenau, H.W. Schock, *Journal of Applied Physics* 87 (2000) 594-602.
- [30] M.A. Contreras, K. Ramanathan, J. Abushama, F. Hasoon, D.L. Young, B. Egaas, R. Noufi, *Progress in Photovoltaics: Research and Applications* 13 (2005) 209-216.
- [31] S. Kundu, L. Olsen, *Conference Record of the Twenty-Ninth IEEE Photovoltaic Specialists Conference*, New Orleans, LA, 2002, pp. 648-651.
- [32] J.S. Ward, K. Ramanathan, F.S. Hasoon, T.J. Coutts, J. Keane, M.A. Contreras, T. Moriarty, R. Noufi, *Progress in Photovoltaics: Research and Applications* 10 (2002) 41-46.
- [33] K. Ramanathan, F.S. Hasoon, S. Smith, D.L. Young, M.A. Contreras, P.K. Johnson, A.O. Pudov, J.R. Sites, *Journal of Physics and Chemistry of Solids* 64 (2003) 1495-1498.

- [34] A. Bauknecht, U. Blieske, T. Kampschulte, J. Albert, H. Sehnert, M.C. Lux-Steiner, A. Klein, W. Jaegemann, *Applied Physics Letters* 74 (1999) 1099-1101.
- [35] D. Hariskos, S. Spiering, M. Powalla, *Thin Solid Films* 480-481 (2005) 99-104.
- [36] J. AbuShama, R. Noufi, S. Johnston, S. Ward, X. Wu, *Photovoltaic Specialists Conference* (2005) 299-302.
- [37] K.T. Ramakrishna, P. Jayarama, *Journal of Physics D: Applied Physics* 25 (1992) 1345-1348.
- [38] J. Song, S. Li, S. Yoon, W. Kim, J. Kim, J. Chen, *Photovoltaic Specialists Conference, 2005. Conference Record on the Thirty-first IEEE* (2005) 449-452.
- [39] S. Siebentritt, A. Bauknecht, A. Gehaed, U. Fiedeler, T. Kampschulte, S. Schuler, W. Harneit, S. Brehme, J. Albert, M.C. Lux-Steiner, *Solar Energy Materials and Solar Cells* 67 (2002) 344-348.
- [40] A. Bauknecht, U. Blieske, T. Kampschulte, A. Enaoui, V. Nadenau, H.W. Schock, A.N. Tiwari, M. Krejci, S. Duchemin, M.C. Artaud, L.M. Smith, S. Rushworth, J. Sollner, M.C. Lux-Steiner, *Proceedings of 2nd World Conference on Photovoltaic Energy Conversion, 1998*, pp. 2436-2439.
- [41] B.G. Lewis, D.C. Paine, *MRS Bulletin* 25 (2002) 22-27.
- [42] T. Minami, *Semiconductor Science and Technology* 20 (2005) 34-35.
- [43] G. Hodes, *Chemical Solution Deposition of Semiconductor Films* (Marcel Dekker, Inc., New York, 2003).
- [44] J.L. Vossen, W. Kern, *Thin film processes II* (Academic Press, Inc., Boston, 1991).
- [45] M.A. Contreras, M.J. Romero, R. Noufi, *Thin Solid Films* 511 (2006) 51.
- [46] R. Kaczynski, *Copper Gallium Diselenide Thin Film Absorber Growth for Solar Cell Device Fabrication*, Ph.D. Thesis, University of Florida, 2007.
- [47] W. Chen, *US Patent* 5,112,410 (1992).
- [48] R. Brundle, S. Wilson, *Encyclopedia of Materials Characterization: Surfaces, Interfaces, Thin Films*, 1992).
- [49] R. Jenkins, R.L. Snyder, *Introduction to X-Ray Powder Diffractometry* (Wiley-Interscience, New York, 1996).
- [50] H.P. Klug, L.E. Alexander, *X-Ray Diffraction Procedures* (Wiley, New York, 1974).
- [51] W.A. Pliskin, S.J. Zanin, *Handbook of Thin Film Technology* (McGraw-Hill, New York, 1970).

- [52] M. Ohring, *The Materials Science of Thin Films* (Academic Press, Inc., San Diego, CA, 1992).
- [53] J. Robertson, *Philosophical Magazine Part B* 63 (1991) 47-77.
- [54] T.V. Herak, *Journal of Non Crystalline Solids* 69 (1984) 39-48.
- [55] J.J. Lander, *Physical Review* 91 (1953) 1382-1387.
- [56] F. Wenner, *A Method of Measuring Earth Resistivity* (Govt. Print. Off., 1916).
- [57] D.K. Schroeder, *Semiconductor material and device characterization* (Wiley, 1990).
- [58] B. Jones, *The Physics Teacher* 31 (1993) 48-49.
- [59] L.B. Valdes, *Proceedings of the IRE* 42 (1954) 420-427.
- [60] R.E. Hummel, *Electronic Properties of Materials* (Springer, New York, 2001).
- [61] F.M. Smits, *BSTJ* 37 (1958) 711-718.
- [62] M.A. Contreras, T. Nakada, M. Hongo, A. Pudov, J. Sites, *Proceedings of 3rd World Conference on Photovoltaic Energy Conversion*, Washington, DC, 2003, pp. 570-573.
- [63] D. Biro, R. Preu, O. Schultz, S. Peters, D. Huljic, *Solar Energy Materials and Solar Cells* 74 (2002) 35-41.
- [64] T. Yamaguchi, Y. Yamamoto, T. Tanaka, A. Yoshida, *Thin Solid Films* 343-344 (1999) 516-519.
- [65] T. Wada, Y. Hashimoto, S. Nishiwaki, T. Satoh, S.H. Idots, *Solar Energy Mater. Solar Cells* (2001).
- [66] K. Ramanathan, M. Contreras, C. Perkins, S. Asher, *Progress in Photovoltaics: Research and Applications* 11 (2003) 225-230.
- [67] C.H. Huang, *Alternative Buffer Layers, Device Modeling and Characterization of Copper-Indium-Diselenide-Based Thin-Film Solar Cells*, Ph.D. Thesis, University of Florida, 2002.
- [68] X. Wu, R. Dhere, D. Albin, T. Gessert, C. Dehart, J.C. Keane, A. Duda, T.J. Coutts, A. Asher, D.H. Levi, H.R. Moutinho, Y. Yan, T. Moriarty, S. Johnston, K. Emery, P. Sheldon, *Proceedings of NCPV Program Review Meeting* (2001) 995.
- [69] P. Smith, *Journal of Vacuum Science & Technology A: Vacuum, Surfaces, and Films* 10 (1992) 897-902.
- [70] J. Ge, Y. Li, *Advanced Functional Materials* 14 (2004) 157-162.

- [71] T. Chu, S. Chu, J. Britt, C. Ferekides, C. Wu, *Journal of Applied Physics* 70 (1991) 2688-2693.
- [72] S.Y. Yin, A.L. Fahrenbruch, R.H. Bube, *Journal of Applied Physics* 49 (1978) 1294.
- [73] X. Li, W. Li, X. Dong, *Japanese Journal of Applied Physics* 45 (2006) 9108-9110.
- [74] D. Okoli, A. Ekpunobi, C. Okeke, *Academic Open Internet Journal* 18 (2006) 1-12.
- [75] P. Roy, J. Ota, S. Srivastava, *Thin Solid Films* 515 (2006) 1912-1917.
- [76] Y. Chang, C. Munsee, G. Herman, J. Wager, P. Mugdur, D.H. Lee, C.H. Chang, *Surface and Interface Analysis* 37 (2005) 398-405.
- [77] J. Cheng, D. Fan, H. Wang, B. Liu, Y. Zhang, H. Yan, *Semiconductor Science and Technology* 18 (2003) 676-679.
- [78] D. Hariskos, M. Powalla, N. Chevaldonnet, D. Lincot, A. Schindler, B. Dimmler, *Thin Solid Films* 387 (2001) 179-181.
- [79] A. Nayeem, G. Vajralingam, K. Yagaiah, M. Nagabhooshanam, *Modern Physics Letters B* 14 (2000) 733-742.
- [80] J. Doña, J. Herrero, *Journal of The Electrochemical Society* 144 (1997) 4081-4091.
- [81] D. Lincot, R. Borges, *Journal of The Electrochemical Society* 139 (1992) 1880-1889.
- [82] S. Mahmoud, A. Ibrahim, A. Riad, *Thin Solid Films* 372 (2000) 144-148.
- [83] L.C. Burton, T.L. Hench, *Applied Physics Letters* 29 (1976) 612.
- [84] M. Valkonen, S. Lindroos, T. Kanninen, M. Leskelä, *Applied Surface Science* 120 (1997) 58-64.
- [85] M. Valkonen, S. Lindroos, M. Leskelä, *Applied Surface Science* (1998).
- [86] M. Valkonen, T. Kanninen, S. Lindroos, M. Leskelä, *Applied Surface Science* 115 (1997) 386-392.
- [87] S. Ray, M. Karanjai, D. DasGupta, *Thin Solid Films* 322 (1998) 117-122.
- [88] I. Oladeji, L. Chow, J. Liu, W. Chu, A.B. Idots, *Thin Solid Films* (2000).
- [89] J. Zhou, X. Wu, G. Teeter, B. To, Y. Yan, R. Dhere, *Physica Status Solidi (b) Applied Research* 241 (2004) 775-778.
- [90] P. O'Brien, J. McAleese, *Journal of Materials Chemistry* 8 (1998) 2309-2314.

- [91] I.O. Oladeji, L. Chow, C.S. Ferekides, V. Viswanathan, Z. Zhao, *Solar Energy Materials and Solar Cells* 61 (2000) 203-211.
- [92] Y.P. Wang, W.I. Lee, T.Y. Tseng, *Applied Physics Letters* 69 (1996) 1807.
- [93] D.C. Reynolds, D.C. Look, B. Jogai, *Solid State Communications* 99 (1996) 873.
- [94] D.M. Bagnall, Y.F. Chen, Z. Zhu, T. Yao, S. Koyama, M.Y. Shen, T. Goto, *Applied Physics Letters* 70 (1997) 2230.
- [95] B. Dong, H. Hu, G. Fang, X. Zhao, D. Zheng, Y. Sun, *Journal of Applied Physics* 103 (2008) 073711-1-8.
- [96] W. Lin, R. Ma, W. Shao, B. Kang, Z. Wu, *Rare Metals* 27 (2008) 32-35.
- [97] S. Lin, J. Huang, P. Sajgalik, *Surface & Coatings Technology* 190 (2005) 39-47.
- [98] L.Y. Chen, W.H. Chen, J.J. Wang, F.C.N. Hong, Y.K. Su, *Applied Physics Letters* 85 (2004) 5628.
- [99] W. Gao, Z. Li, *Ceramics International* 30 (2004) 1155-1159.
- [100] E. Fu, D. Zhuang, G. Zhang, Z. ming, W. Yang, J. Liu, *Microelectronics Journal* 35 (2004) 383-387.
- [101] C.H. Lee, K.S. Lim, J. Song, *Solar Energy Materials & Solar Cells* 43 (1996) 37.
- [102] C.H. Lee, K.S. Lim, J. Song, *Japanese Journal of Applied Physics* 36 (1997) 4418.
- [103] S.J. Baik, J.H. Jang, C.H. Lee, W.Y. Cho, K.S. Lim, *Applied Physics Letters* 70 (1997) 3516.
- [104] R.G. Jianhua, *Solar Cells* 30 (1991) 437.
- [105] M. Yoshino, W.W. Wenas, A. Yamada, M. Konagai, K. Takahashi, *Japanese Journal of Applied Physics* 32 (1993) 726.
- [106] M. Tzolov, N. Tzenov, D. Dimova-Malinovska, *Thin Solid Films* 379 (2000) 28-36.
- [107] Q. Li, D. Zhu, W. Liu, Y. Liu, X. Ma, *Applied Surface Science* 254 (2008) 2922-2926.
- [108] S. Lee, T. Lee, K. Lee, B. Cheong, Y. Kim, W. Kim, *Journal of Physics D: Applied Physics* 41 (2008) 1-7.
- [109] C.G. Van De Walle, *Phys Rev Lett* 85 (2000) 1012-1015.
- [110] C.G. Van de Walle, J. Neugebauer, *Nature* 423 (2003) 626-628.
- [111] P. Nunes, D. Costa, E. Fortunato, R. Martins, *Vacuum* 64 (2002) 293-297.

- [112] M. Martinez, J. Herrero, M. Gutiérrez, *Solar Energy Materials and Solar Cells* 45 (1997) 75-86.
- [113] J. Lee, K. Kang, S. Kim, K. Yoon, I. Park, J. Song, *Solar Energy Materials and Solar Cells* 64 (2000) 185-195.
- [114] V. Musat, B. Teixeira, E. Fortunato, R. Monteiro, *Thin Solid Films* 502 (2006) 219-222.
- [115] J. Chang, W. Lin, M. Hon, *Applied Surface Science* 183 (2001) 18-25.
- [116] B. Oh, M. Jeong, D. Kim, W. Lee, J. Myoung, *Journal of Crystal Growth* 281 (2005) 475-480.
- [117] G. Fang, D. Li, B. Yao, *Vacuum* 68 (2003) 363-372.
- [118] V. Srikant, D.R. Clarke, *Journal of Applied Physics* 81 (1997) 6357.
- [119] K. Kim, K. Park, D. Ma, *Journal of Applied Physics* 81 (1997) 7764-7772.
- [120] J. Chang, M. Hon, *Thin Solid Films* 386 (2001) 79-86.
- [121] M. Ritala, T. Asikainen, M. Leskela, J. Skarp, *Thin Films for Photovoltaic and Related Device Applications: Symposium Held April 8-11 426* (1996) 513.
- [122] J.A.A. Selvan, H. Keppner, A. Shah, *Thin Films for Photovoltaic and Related Device Applications: Symposium Held April 8-11, 1996, San Francisco, California, USA* (1996).
- [123] A. Gupta, A. Compaan, *Applied Physics Letters* 85 (2004) 684-686.
- [124] M. Bertolotti, M.V. Laschena, M. Rossi, A. Ferrari, L.S. Qian, F. Quaranta, A. Valentini, *Journal of Materials Research* 5 (1990) 1929-1932.
- [125] V. Gupta, A. Mansingh, *Journal of Applied Physics* 80 (1996) 1063-1073.
- [126] K.S. Weissenrieder, J. Müller, *Thin Solid Films* 300 (1997) 30-41.
- [127] A.P. Roth, D.F. Williams, *Journal of The Electrochemical Society* 128 (1981) 2684.
- [128] J.L. Deschanvres, B. Bochu, J.C. Joubert, *Journal de Physique* 4 3 (1993) 3-485.
- [129] J. Lee, B. Yeo, B. Park, *Thin Solid Films* 457 (2004) 333-337.
- [130] J.H. Webb, D.F. Williams, M. Buchanan, *Applied Physics Letters* 39 (1981) 640.
- [131] L. Vasanelli, A. Valentini, A. Losacco, *Solar Energy Materials* 16 (1987) 91.
- [132] Y. Suzuki, T. Yotsuya, K. Takiguchi, M. Yoshitakey, S. Ogawa, *Appl. Surf. Sci* 33 (1988) 1114.

- [133] S. Fujihara, C. Sasaki, T. Kimura, *Applied Surface Science* 180 (2001) 341-350.
- [134] K. Park, D. Ma, K. Kim, *Thin Solid Films* 305 (1997) 201-209.
- [135] B.H. Choi, H.B. Im, others, *Thin Solid Films* 193 (1990) 712-720.
- [136] T. Minami, H. Sato, H. Nanto, S. Takata, *Japanese journal of applied physics. Pt. 2, Letters* 25 (1986) L776-L779.
- [137] G.A. Hirata, J. McKittrick, T. Cheeks, J.M. Siqueiros, J.A. Diaz, O. Contreras, O.A. Lopez, *Thin Solid Films* 288 (1996) 29-31.
- [138] S.A. Studenikin, N. Golego, M. Cocivera, *Journal of Applied Physics* 87 (2000) 2413.
- [139] Y. Igasaki, H. Saito, others, *Thin Solid Films* 199 (1991) 223-230.
- [140] D. Zhang, D. Brodie, *Thin Solid Films* 238 (1994) 95-100.
- [141] F.H. Lu, H.Y. Chen, *Thin Solid Films* 355 (1999) 374-379.
- [142] S. Chu, W. Water, J. Liaw, *Journal of the European Ceramic Society* 23 (2003) 1593-1598.
- [143] S. Lin, J. Huang, P. Sajgalik, *Surface & Coatings Technology* 185 (2004) 254-263.
- [144] K. Kim, H. Tampo, J. Song, T. Seong, S. Park, *Japanese Journal of Applied Physics* 44 (2005) 4776-4779.
- [145] P.M. Verghese, D.R. Clarke, *Journal of Materials Research* 14 (1999) 1039-1045.

## BIOGRAPHICAL SKETCH

Andre Baran V, the son of Andre Baran IV and Candace Elizabeth Harte Baran, was born in 1980 in Deland, Florida. As an only child, he grew up primarily in Port Orange, Florida, graduating from the International Baccalaureate program at Spruce Creek High School in 1999. He chose to continue his education in Atlanta, Georgia. He was honored with the prestigious President's Scholarship for outstanding leadership and academic achievements from the Georgia Institute of Technology where he earned a Bachelor of Science in chemical engineering in 2002.

In 2003 he returned to Florida and entered the Ph.D. program in the Department of Chemical Engineering at the University of Florida in Gainesville. He pursued his research under Dr. Oscar D. Crisalle in the area of thin film photovoltaics. Upon completion of his Ph.D. studies Andre will be relocating to Oregon where he will work for the Intel Corporation as a part of their Portland Technology Development center.